



The
University
Of
Sheffield.

Department of Physics and Astronomy

**Magnetic and Magneto-Optical
Properties of Doped Oxides**

Mohammed S. Alqahtani

Thesis submitted to the University of Sheffield for the degree of

Doctor of Philosophy

October 2012

Acknowledgments

It has been a real privilege to study and research as a participant in the magnetic oxide semiconductors group at the University of Sheffield. I wish to express my great gratitude and sincere appreciation to my principle supervisor, Professor Gillian Gehring. I am really in debt to her for her inspiring guidance, overwhelming support and fruitful discussion throughout the development of this thesis.

Thanks are also due to my Co-advisor, Mark Fox and to Dr. Harry Blythe for their assistance and valuable suggestions throughout the various stages of the experimental parts of the work.

I extend a special thanks to my colleagues Qi Feng, David Score, Ali Hakimi, Minju Ying, Hasan Albargi and Wala Dizayee for their encouragement, and for the fantastic time I have had.

Special thanks to my parents who have been always a great support to me since my childhood. Also, I would like to thank all my brothers and sisters, my friends Dr. Mohammed Alshorman and Dr. Saad Alqahtani for all their support. Finally, I wish to thank my son Yasser and my daughter Lana for their love and patient.

Last of all, but no means the least; I am thankful to the chairmen/women and members of the department of physics and Astronomy in the University of Sheffield for their help and encouragement.

Mohammed Alqahtani

Sheffield, October 2012.

Abstract

This thesis describes the growth, structural characterisation, magnetic and magneto-optics properties of lanthanum strontium manganite (LSMO), GdMnO₃ and transition metal (TM)-doped In₂O₃ thin films grown under different conditions. The SrTiO₃ has been chosen as a substrate because its structure is suitable to grow epitaxial LSMO and GdMnO₃ films. However, the absorption of SrTiO₃ above its band gap at about 3.26 eV is actually a limitation in this study. The LSMO films with 30% Sr, grown on both SrTiO₃ and sapphire substrates, exhibit a high Curie temperature (T_c) of 340 K. The magnetic circular dichroism (MCD) intensity follows the magnetisation for LSMO on sapphire; however, the measurements on SrTiO₃ were dominated by the birefringence and magneto-optical properties of the substrate. In the GdMnO₃ thin films, there are two well-known features in the optical spectrum; the charge transfer transition between Mn d states at 2 eV and the band edge transition from the oxygen p band to d states at about 3 eV; these are observed in the MCD. This has been measured at remanence as well as in a magnetic field. The optical absorption at 3 eV is much stronger than at 2 eV, however, the MCD is considerably stronger at 2 eV. The MCD at 2 eV correlates well with the Mn spin ordering and it is very notable that the same structure appears in this spectrum, as is seen in LaMnO₃. The results of the investigations of Co and Fe-doped In₂O₃ thin films show that TM ions in the films are TM²⁺ and substituted for In³⁺. The room temperature ferromagnetism observed in TM-doped In₂O₃ is due to the polarised electrons in localised donor states associated with oxygen vacancies. The formation of Fe₃O₄ nanoparticles in some Fe-doped films is due the fact that TM-doped In₂O₃ thin films are extremely sensitive to the growth method and processing condition. However, the origin of the magnetisation in these films is due to both the Fe-doped host matrix and also to the nanoparticles of Fe₃O₄.

Publications

Gillian A. Gehring, Harry J. Blythe, Qi Feng, David S. Score, Abbas Mokhtari, Marzook Alshammari, **Mohammed S. Al Qahtani** and A. Mark Fox, *Using Magnetic and optical methods to determine the size and characteristics of nanoparticles embedded in oxide semiconductors*, IEEE Transactions on Magnetics, vol. 46, issue 6, pp. 1784-1786.(2010).

A. M. H. R. Hakimi, M. G. Blamire, S. M. Heald, M. S. Alshammari, **M. S. Alqahtani**, D. S. Score, H. J. Blythe, A. M. Fox and G. A. Gehring, *Donor band ferromagnetism in cobalt-doped indium oxide*, Physical Review B 84 (8), 085201 (2011).

F.-X. Jiang, X.-H. Xu, J. Zhang, X.-C. Fan, H.-S. Wu, M. Alshammari, Q. Feng, H. J. Blythe, D. S. Score, K. Addison, **M. Al-Qahtani** and G. A. Gehring, *Room temperature ferromagnetism in metallic and insulating $(In_{1-x}Fe_x)_2O_3$ thin films*, Journal of Applied Physics 109 (5), 053907-053907 (2011).

Mohammed S. Al Qahtani, Marzook Alshammari, H.J Blythe, A.M. Fox, G.A.Gehring,N. Andreev, V. Chichkov, and Ya, Mukovskii, *Magnetic and Optical properties of strained films of multiferroic $GdMnO_3$* , *Journal of Physics* (accepted 2012).

Marzook S. Alshammari, **Mohammed S Alqahtani**, AM Fox, HJ Blythe, A. M. H. R. Hakimi,SM HealdS. Alfahad, M. Alotibi, A. Alyamani, GA Gehring, *Magnetic, Transport, Optical and Magneto-optical investigations of In_2O_3 containing Fe_3O_4 nanoparticles*, (prepared for publication).

David S. Score, James R. Neal, Anthony J. Behan, Abbas Mokhtari, Feng Qi, Marzook Alshammari, **Mohammed S. Al Qahtani**, Harry J. Blythe, A. Mark Fox, Roy W. Chantrell, Steve M Heald, Stefan T. Ochsenbein and Daniel R. Gamelin, Gillian A. Gehring, *Enhanced magnetism in $ZnCoO$ by exchange coupling to Co nanoparticles*, (prepared for publication).

Conferences

M. Alshammari, **Mohammed S. Al Qahtani**, Qi Feng, H.J. Blythe, D.S. Score, K. Addison, A.M. Fox, G.A. Gehring, Feng-Xian Jiang, Xiao-Hong Xu, Jun Zhang, Xiao-Chen Fan, Hai-Shun Wu, *Influence of oxygen pressure on the magnetic and transport properties of Fe-doped In₂O₃ thin films*, Condensed Matter and Materials Physics CMMP09, at the University of Warwick, 2009, Dec. 15-17, UK.

Mohammed S. Al Qahtani, Marzook Alshammari, H.J. Blythe, A.M. Fox, G.A. Gehring, N. Andreev, V. Chichkov, and Ya. Mukovskii, *Magnetic and Optical properties of strained films of multiferroic GdMnO₃*, Condensed Matter and Material Physics Conference (CMMP) 2010, University of Warwick, 2010, Dec. 14-16, UK.

Contents

Acknowledgments.....	i
Abstract.....	ii
Publications.....	iii

Chapter 1- Introduction and Thesis Structure

1.1 Introduction.....	1
1.2 Thesis Structure	3
1.3 References.....	5

Chapter 2- Theoretical Background

2.1 Introduction.....	8
2.2 Magnetic Moment of Electron in a Free Ion.....	8
2.3 Magnetisation in Solids.....	12
2.4 Diamagnetism	13
2.5 Paramagnetism.....	14
2.6 Ferromagnetism	16
2.7 Anti-Ferromagnetism.....	20
2.8 Exchange Interaction in Magnetic Systems	21
2.8.1 Direct Exchange Interaction	21
2.8.2 Indirect Interactions	21
I Super-Exchange.....	22
II Double Exchange Interaction.....	23
III RKKY Interaction.....	24
2.9 A Brief History of Oxide Thin Films.....	25
2.10 References.....	30

Chapter 3- Experimental Methods

3.1 Introduction:.....	33
3.2 Target and Film Preparation:	33
3.3 Pulsed Laser Deposition	34
3.3.1 Excimer Laser	34
3.3.2 Basics Excimer Laser.....	35
3.3.3 Mechanisms of Pulsed Laser Deposition.....	37
3.4 Growth of Thin Films and PLD System	39
3.5 Measuring Film Thickness- Dektak Surface Profiler	42
3.6 Measuring Magnetisation – SQUID Magnetometer	45
3.6.1 SQUID Fundamentals.....	45
3.6.2 Sample Handling and SQUID Operation.....	47
3.7 Magneto-Optics Basics	51
3.8 Magneto-Optics Set-up and Principles of the Technique	53
3.9 Optical Transmission and Reflection Techniques	57
3.10 Thin Films Samples Investigated.....	60
3.11 References.....	63

Chapter 4- Lanthanum Strontium Manganite (LSMO)

4.1 Introduction:.....	67
4.2 Literature Review on LSMO	68
4.3 Experiment Results and Discussion.....	79
4.3.1 The Dependence of Magnetic Properties on Oxygen Pressure and Type of Substrate.....	81
4.3.2 Dependence of Magnetic Properties on Film Thickness	86
4.3.3 Dependence of Magnetic Properties on Annealing	89
4.3.4 Magneto-Optical Properties of LSMO Thin Films.....	92

4.4 Summary and Conclusions	99
4.5 References.....	101

Chapter 5- Multiferroic Manganite GdMnO₃

5.1 Introduction.....	106
5.2 Literature Review on the Multiferroic, Gadolinium Manganite (GdMnO ₃).....	107
5.3 Experimental Results and Discussion	113
5.3.1 Magnetic Measurements	114
5.3.2 Optical Measurements	119
5.4 Summary and Conclusions	128
5.5 References.....	129

Chapter 6- Strontium Titanate STO Substrates

6.1 Introduction.....	132
6.2 Literature on Optical and Magneto-Optical properties of STO Substrates.....	132
6.3 Experiment Results and Discussion.....	137
6.4 Summary and Conclusions	149
6.5 References.....	150

Chapter 7- Transition Metal (TM) Doped In₂O₃

7.1 Introduction.....	152
7.2 Literature Review on TM Doped In ₂ O ₃	152
7.3 Experiment Result and Discussion	157
7.3.1 Co Doped In ₂ O ₃	157
7.3.2 Fe Doped In ₂ O ₃	164
7.4 Summary and Conclusions	179
7.5 References.....	181

Chapter 8- Conclusions and Future Work

8.1 Conclusions.....	186
8.1.1 LSMO Thin Films.....	186
8.1.2 GdMnO ₃ Thin Films	188
8.1.3 Co and Fe-Doped In ₂ O ₃ Thin Films.....	189
8.2 Future Work.....	190
8.3 Reference	192

Appendix A

Chapter 6 – Appendix	194
References.....	197

Chapter 1

Introduction and Thesis Structure

1.1 Introduction

A spintronics or spin device electronics, where the spin of electrons in addition to their electrical charge is used to encode information, is an emerging technology that replaces conventional semiconductor-based electronic devices [1-2]. The concept of a spintronic device relies on a source of spin-polarised currents, and so researchers have shown intense interest in materials that have the largest possible spin polarisations of the conduction electrons at the Fermi level. Of most interest for research, are materials which display metallic characteristics for the majority-spin electrons, while the Fermi energy falls in a gap in the density of states for the minority-spin electrons. This behaviour is known as half-metallic ferromagnetism and was predicted to occur in oxides [3-4]. There is particular interest in the half-metallic material systems which include doped manganites, double perovskites and magnetite. All of them show Curie temperatures above room temperature, meaning they are well-suited for the purposes of spintronics [2, 5]. Amongst a wide range of Perovskite-type of manganites, $(\text{La}_{0.7}\text{Sr}_{0.3})\text{MnO}_3$ (LSMO) is expected to display a nearly complete spin polarisation at the Fermi level. The potential has been observed for LSMO thin films to perform well in spintronic devices [6-7].

The field of oxide electronics has expanded exponentially since the 1990's, due to the discovery of high- T_c superconductors and with the progress in thin film technology. Oxides are representative of strongly correlated electronic systems;

therefore they have versatile physical properties. Different degrees of freedom are present and different ordering phenomena occur within the same materials and result in phenomena including superconductivity and ferromagnetism [2].

Semiconducting indium oxide (In_2O_3) is in the focus for current research and thought to be an ideal material for dilute magnetic semiconductors (DMS) when doped with transitional metal (TM) ions. Room temperature ferromagnetism has been reported for all 3d TM (V, Cr, Fe, Cu, Ni and Co) doped In_2O_3 [8-20]. Indium oxide is a cubic structure with 80 atoms per unit cell. It has a wide band-gap energy (3.75 eV), large carrier density when doped with Sn and is transparent in the visible region. All these properties make In_2O_3 well-suited for the purposes of device applications [21-23].

Multiferroic oxides are another possible candidate for spintronics device applications [24-25]. These oxides have the property of two or more ferroic order parameters co-existing in one single phase. The majority of the multiferroic transition metal oxides display antiferromagnetic properties, so research is required to find those oxides that display ferromagnetic properties [26-27]. However, some success has been observed in applications of multiferroics. They have been used as thin film barriers in spin filter tunnel junctions and in semiconductor devices as electrodes [2, 25].

The subject of this thesis is the study of the magnetic and magneto-optic properties of LSMO, multiferroic GdMnO_3 and TM-doped In_2O_3 thin films.

1.2 Thesis Structure

This thesis consists of eight chapters, chapter one is the introduction of the thesis and chapter two provides basic concepts and background information on magnetisation and magneto-optics. A discussion of the exchange interaction and a history on oxide thin films are introduced in this chapter.

Chapter three describes the experimental techniques used in this thesis. It also gives some background information beyond the techniques and describes how the work was carried out.

Chapter four describes the experimental investigation of the magnetic and magneto-optics properties of LSMO thin films. The effect of growth conditions, substrate, film thickness and annealing on magnetic and magneto-optics properties is introduced. In addition, a literature review on LSMO is given in this chapter.

Chapter five describes the experimental investigation of the magnetic and magneto-optics properties of multiferroic GdMnO_3 thin films. The role of strain in these films is discussed in this chapter. It also gives a literature review on multiferroic manganite GdMnO_3 .

Chapter six describes the experimental investigation of the optical and magneto-optical properties of the STO substrate. The film grown on an STO substrate exhibited an anomalous magnet-optics behaviour due to the birefringence of the STO substrate. The influence of birefringence on the magneto-optics data taken using the Sato method is given in this chapter.

Chapter seven describes the experimental investigation of the magnetic and magneto-optics properties of Co and Fe doped In_2O_3 thin films. The influence of TM concentration, growth conditions, annealing and adding Sn on

the magnetic and magneto-optics properties is introduced in this chapter. The contribution of TM ions to the magnetisation is explored in order to determine the origin of the ferromagnetism and a new method is established to estimate the contribution of Co and Fe ions in In_2O_3 system. This chapter also provides an introduction and a literature review of TM-doped In_2O_3 .

Chapter eight is a summary of the experimental results. Proposals for future work and projects are also discussed.

1.3 References

1. G. A. Prinz, *Science* **282** (5394), 1660-1663 (1998).
2. M. Opel, *Journal of Physics D-Applied Physics* **45** (3) (2012).
3. A. Yanase and K. Siratori, *Journal of the Physical Society of Japan* **53** (1), 312-317 (1984).
4. R. A. Degrout, F. M. Mueller, P. G. Vanengen and K. H. J. Buschow, *Physical Review Letters* **50** (25), 2024-2027 (1983).
5. J. M. D. Coey and C. L. Chien, *Mrs Bulletin* **28** (10), 720-724 (2003).
6. H. L. Liu, K. S. Lu, M. X. Kuo, L. Uba, S. Uba, L. M. Wang and H. T. Jeng, *Journal of Applied Physics* **99** (4), 043908-043907 (2006).
7. T. K. Nath, J. R. Neal and G. A. Gehring, *Journal of Applied Physics* **105** (7), 07D709-703 (2009).
8. D. Berardan, E. Guilmeau and D. Pelloquin, *Journal of Magnetism and Magnetic Materials* **320** (6), 983-989 (2008).
9. L. M. Huang, C. M. Araujo and R. Ahuja, *Epl* **87** (2) (2009).
10. H. W. Ho, B. C. Zhao, B. Xia, S. L. Huang, J. G. Tao, A. C. H. Huan and L. Wang, *Journal of Physics-Condensed Matter* **20** (47) (2008).
11. Sub, iacute, G. as, J. Stankiewicz, F. Villuendas, M. Lozano, P. a, Garc and J. a, *Physical Review B* **79** (9), 094118 (2009).
12. J. Philip, A. Punnoose, B. I. Kim, K. M. Reddy, S. Layne, J. O. Holmes, B. Satpati, P. R. LeClair, T. S. Santos and J. S. Moodera, *Nat Mater* **5** (4), 298-304 (2006).
13. G. Z. Xing, J. B. Yi, D. D. Wang, L. Liao, T. Yu, Z. X. Shen, C. H. A. Huan, T. C. Sum, J. Ding and T. Wu, *Physical Review B* **79** (17), 174406 (2009).

14. R. P. Panguluri, P. Kharel, C. Sudakar, R. Naik, R. Suryanarayanan, V. M. Naik, A. G. Petukhov, B. Nadgorny and G. Lawes, *Physical Review B* **79** (16), 165208 (2009).
15. Y. K. Yoo, Q. Xue, H.-C. Lee, S. Cheng, X. D. Xiang, G. F. Dionne, S. Xu, J. He, Y. S. Chu, S. D. Preite, S. E. Lofland and I. Takeuchi, *Applied Physics Letters* **86** (4), 042506-042503 (2005).
16. O. D. Jayakumar, I. K. Gopalakrishnan, S. K. Kulshreshtha, A. Gupta, K. V. Rao, D. V. Louzguine-Luzgin, A. Inoue, P. A. Glans, J. H. Guo, K. Samanta, M. K. Singh and R. S. Katiyar, *Applied Physics Letters* **91** (5), 052504-052503 (2007).
17. D. Chu, Y.-P. Zeng, D. Jiang and Z. Ren, *Applied Physics Letters* **91** (26), 262503-262503 (2007).
18. P. F. Xing, Y. X. Chen, S.-S. Yan, G. L. Liu, L. M. Mei, K. Wang, X. D. Han and Z. Zhang, *Applied Physics Letters* **92** (2), 022513-022513 (2008).
19. X.-H. Xu, F.-X. Jiang, J. Zhang, X.-C. Fan, H.-S. Wu and G. A. Gehring, *Applied Physics Letters* **94** (21), 212510-212513 (2009).
20. F.-X. Jiang, X.-H. Xu, J. Zhang, H.-S. Wu and G. A. Gehring, *Applied Surface Science* **255** (6), 3655-3658 (2009).
21. H. Kim, M. Osofsky, M. M. Miller, S. B. Qadri, R. C. Y. Auyeung and A. Pique, *Applied Physics Letters* **100** (3), 032404-032403 (2012).
22. J.-H. Lee, S.-Y. Lee and B.-O. Park, *Materials Science and Engineering: B* **127** (2–3), 267-271 (2006).
23. C. Nunes de Carvalho, G. Lavareda, A. Amaral, O. Conde and A. R. Ramos, *Journal of Non-Crystalline Solids* **352** (23–25), 2315-2318 (2006).
24. M. Fiebig, *Journal of Physics D-Applied Physics* **38** (8), R123-R152 (2005).

25. N. A. Spaldin, S.-W. Cheong and R. Ramesh, *Physics Today* **63** (10), 38-43 (2010).
26. T. Kimura, S. Kawamoto, I. Yamada, M. Azuma, M. Takano and Y. Tokura, *Physical Review B* **67** (18) (2003).
27. N. A. Spaldin and M. Fiebig, *Science* **309** (5733), 391-392 (2005).

Chapter 2

Theoretical Background

2.1 Introduction

This chapter will provide a brief discussion of the concepts of magnetism and the various possible exchange interactions. It will also provide a history of the investigation of oxide materials that relate to the topics covered in this thesis. The introduction to the concepts of magnetisation was obtained by referring to the following text books: “Magnetic Materials Fundamentals and Device Applications” by N.A.Saldin [1], “Introduction to Solid States Physics” by C. Kittel [2], “Physics of Magnetism and Magnetic Materials” by K.H.J.Buschow and F.R.D.Boer [3], “Magnetism and magnetic materials” by J.M.D.Coey [4].

2.2 Magnetic Moment of Electron in a Free Ion

Magnetic moment is the fundamental object in magnetism. From elementary physics, the current I circulating in a loop of area A produces a magnetic moment given by:

$$\mu_m = IA \tag{2.1}$$

The direction of μ_m is normal to the plane of the loop and such that the current flows counter-clockwise relative to an observer, standing along μ_m as shown in fig.2.1.

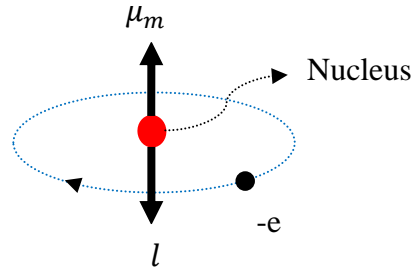


Figure (2.1): the electron moves in circular orbit where the magnetic moment μ_m and the quantised angular momentum l are oppositely directed.

A magnetic dipole moment is so called because it behaves similarly to an electric dipole which consists of one negative charge and one positive charge separated by a small distance. In a similar way, the movement of the electron around the nucleus produces a magnetic moment given by:

$$\mu_L = I_e A = I_e (\pi r^2), \quad 2.2$$

where, I_e is the current due to the circulation of the electric charge (e) in a circular orbit with period T around the nucleus. The orbital angular momentum of the electron is given by:

$$L = r^2 \omega, \quad 2.3$$

where r is the radius of the circular orbit, m is the mass of the electron and ω is the angular velocity. Hence, the magnetic moment of the electron in terms of its angular momentum is given by:

$$\vec{\mu}_L = \frac{e}{T} (\pi r^2) = -\frac{e}{2m} \vec{L} \quad 2.4$$

From quantum theory the angular momentum of an orbital electron is determined by the orbital quantum number l as:

$$L = \frac{lh}{2\pi} = l\hbar \quad 2.5$$

Substituting the value of L from eqn. 2.5 into eqn. 2.4 gives:

$$\vec{\mu}_l = -\frac{eh}{4\pi m} = -\frac{e}{2m} l\hbar = -\mu_B \vec{l} \quad 2.6$$

Eqn. (2.6) shows that an electron in an atom can take only certain specified values of magnetic moment (quantised) depending on the l values. The component of the orbital angular momentum along the applied magnetic field direction is given by $m_l \hbar$, where m_l is the orbital magnetic quantum number. The quantity $\mu_B = \frac{e\hbar}{2m}$ is called the Bohr magneton which equals 9.27×10^{-24} J/T.

To fully specify the state of an electron in the atom, a fundamental concept needs to be introduced; this is the spin of the electron. By an analogy with the orbital magnetic moment, it might be expected that the spin magnetic moment is given by:

$$\vec{\mu}_s = -\mu_B \vec{s} \quad 2.7$$

But, in fact, this is incorrect and the situation for the spin angular momentum is different because twice as much moment is created by spin angular momentum than for orbital angular momentum. Therefore the spin magnetic moment is given by:

$$\vec{\mu}_s = -g_e \mu_B \vec{s} , \quad 2.8$$

where, the factor g is called the g-factor of the electron or the Landé splitting factor. This was originally introduced by Landé to explain the anomalous Zeeman effect and latter theories have justified the assumption theoretically. By taking $g=2$ the spin magnetic moment along the field direction is one Bohr magneton for a single electron.

Similarly to the electron, the nucleus has its own spin associated with its angular momentum. The mass of the nucleus is of the order of 2000 times the mass of electron and hence the magnetic moment associated with the nuclear spin can be ignored since it is very small.

The total spin angular momentum, \vec{S} , and the total orbital angular momentum, \vec{L} , of the electrons are combined to determine the total angular momentum, \vec{J} , as follows:

$$\vec{S} = \sum_i \vec{s}_i, \quad \vec{L} = \sum_i \vec{l}_i \quad \text{and} \quad \vec{J} = \vec{L} + \vec{S} \quad 2.9$$

This type of coupling is referred to L-S coupling (Russell-Saunders coupling). In light atoms the coupling between the individual spins to give \vec{S} and the individual orbital angular momenta to give \vec{L} is stronger than spin-orbit coupling giving \vec{J} . However, there is also j-j coupling for the heavy atoms where the spin-orbit coupling dominates. In this case, the spin and orbital angular momenta of individual electrons couple to give the total angular momenta per electron which interact via electron distributions to form the resultant total angular momentum.

The total magnetic moment, $\vec{\mu}_T = \vec{\mu}_S + \vec{\mu}_L$ is not collinear with \vec{J} but makes an angle, θ , with, \vec{J} , and precesses around it. Therefore, the magnetic moment and then the magnetic properties are determined by:

$$\vec{\mu} = \vec{\mu}_T \cos\theta = -g_J \mu_B \vec{J}, \quad 2.10$$

where, g_J is called the Landé g-factor and is given by:

$$g_J = 1 + \frac{J(J+1) + S(S+1) - L(L+1)}{2J(J+1)} \quad 2.11$$

The atomic magnetic moment(μ) determines the magnetisation of the system. The magnetisation of a material is expressed in terms of density of net magnetic moment μ .

2.3 Magnetisation in Solids

In solids, the magnetism of the material is defined as the sum of the magnetic moments per unit volume as:

$$\vec{M} = \sum_{\text{unit volume}} \vec{\mu}_i \quad 2.12$$

When an external magnetic field (H) is applied to a material, the relationship between H and the magnetic induction (B) is given by:

$$B = \mu_0(H + M) , \quad 2.13$$

where, $\mu_0 = 4\pi \times 10^{-7} \text{ Hm}^{-1}$ is the magnetic permeability in free space and M is the magnetisation of the material. The properties of the material are defined by the way in which M or B varies with the applied magnetic field H . The ability of a material to become magnetised is called magnetic susceptibility (χ) which is defined in low field as the ratio between M and H :

$$\chi = \frac{M}{H} \quad 2.14$$

The permeable of the material to the magnetic field is called permeability (μ) and given by:

$$\mu = \frac{B}{H} \quad 2.15$$

The relative permeability of the material (μ_r) is defined as the ratio of μ and μ_0 :

$$\mu_r = \frac{\mu}{\mu_0} \quad 2.16$$

The values of the magnetic susceptibility (χ) and the relative permeability (μ_r) can be used to classify magnetic materials. The materials with negative susceptibility are defined as diamagnetic whereas if the susceptibility and the permeability are small and positive the materials are known as paramagnetic. As for paramagnetic materials, ferromagnetic materials have a positive susceptibility and permeability, but much larger values.

2.4 Diamagnetism

The susceptibility of diamagnetic materials is negative as has been mentioned in sect. (2.3). The application of a magnetic field to the diamagnetic material leads to the induced magnetic moment being directed in the opposite direction of the applied magnetic field as shown in fig.2.2; and this type of magnetism is found in all matter. The materials in which diamagnetic is observed consist of atoms that have no net magnetic moment, because they have filled electron shells. The noble gases, NaCl and Al₂O₃ are examples of materials that show this type of magnetism. The classical Langevin theory and quantum theory give the same result for the diamagnetic susceptibility which is given by:

$$\chi = -\frac{N\mu_0 Z e^2 \langle r^2 \rangle_{av}}{6m_e}, \quad 2.17$$

where, Z is the number of electrons, e is the electron charge; N is the number of atoms per unit volume, m_e is the electron mass and $\langle r^2 \rangle_{av}$ is the average value of all occupied orbital radii. It is clear from eqns. 2.17 that the diamagnetic susceptibility is negative and temperature independent.

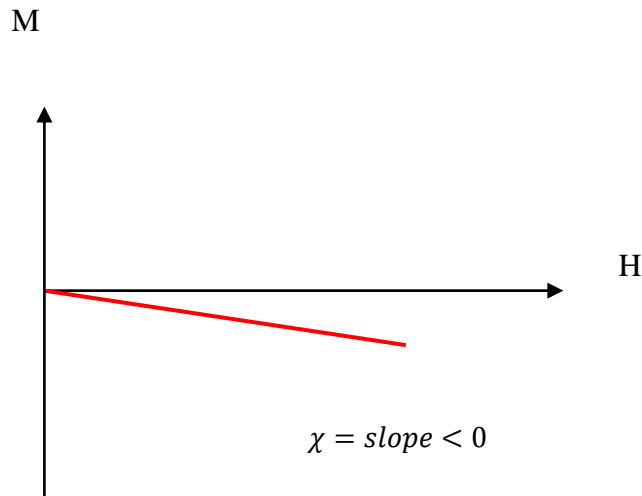


Figure (2.2): The diamagnetic magnetisation and susceptibility are negative and independent of temperature.

2.5 Paramagnetism

Paramagnetic materials have a net magnetic moment due to the unpaired electron in the partially-filled orbitals. The magnetic moments on neighbouring atoms in paramagnetic materials are non-interacts and the temperature causes random orientation of these moments. The application of a magnetic field aligns the magnetic moments partially toward the field direction. At low field, the magnetisation of paramagnetic materials increases as the magnetic field is increased and the paramagnetic susceptibility is temperature dependent as shown in fig. 2.3. The paramagnetic susceptibility is given by Curie's law as:

$$\chi = \frac{N\mu_0\mu_{eff}^2}{3k_B T} = \frac{C}{T}, \quad 2.18$$

where, $\mu_{eff} = g\sqrt{J(J+1)}\mu_B$, C is the Curie constant and k_B is Boltzmann's constant.

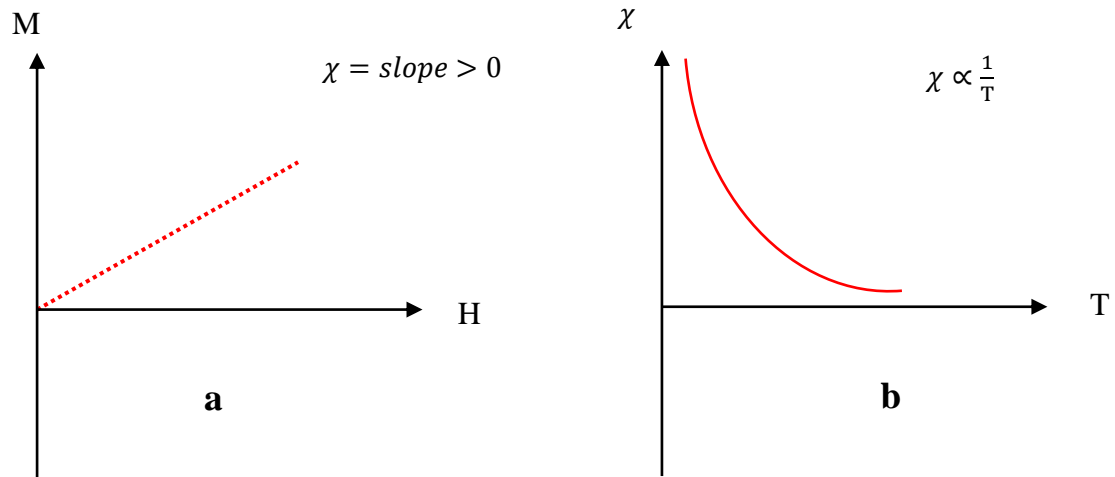


Figure (2.3): a) The paramagnetic magnetisation and susceptibility are positive b) The paramagnetic susceptibility is temperature dependent.

In fact Curie's law is modified if moments interact ferromagnetically to give the Curie-Weiss law which is given by:

$$\chi = \frac{c}{T-\theta} \quad 2.19$$

The paramagnetic materials follow the Curie-Weiss law until a critical temperature (θ) below which the material becomes ferromagnetic. The magnetic moment of the paramagnetic ions can be calculated using equation (2.10). The calculated and experimental values of the magnetic moment are in agreement for most paramagnetic ions. However for transition-metals this agreement does not work, unless the orbital angular momentum of the electrons is completely ignored as shown

in Table (2.1) for some transition-metal ions used in this thesis. This phenomenon is called quenching of the orbital angular momentum where the electric fields generated by the surrounding ions in the solid force the orbitals to be coupled strongly to the crystal lattice. As a result, the orbitals are prevented turning toward the field and then the magnetic moment is determined by electron spin only.

**Removed by the
author for copyright reasons**

Table (2.1): Calculated and measured effective magnetic moment for some transition-metal ions [1-2].

2.6 Ferromagnetism

Ferromagnetic materials are magnetic materials that exhibit spontaneous magnetisation and a magnetic ordering temperature. The presence of ferromagnetic behaviour in common materials (iron, cobalt, nickel) is due to the atoms containing unfilled orbits. Most of the ferromagnetic metals have 4s and 3d partially filled bands. The d bands are relatively flat and the mobility of the d band electrons is low (localized) whereas s bands are parabolic structure and the mobility of s band

electrons are high (delocalized). The exchange interaction between electrons induces the electrons bands splitting. This leads to an imbalance between the density of spin-up (majority) and spin-down (minority) of 3d electrons as shown in fig. 2.4, which give rise to the magnetisation. However, application of an external magnetic field can enhance or weaken the band splitting and thus changes the magnetisation. A weaker exchange interaction in a 4s band causes a balance in the distribution of 4s spin-up and spin-down electrons. Therefore, the 3d band is responsible for the magnetism in the ferromagnetic metals [5-8].

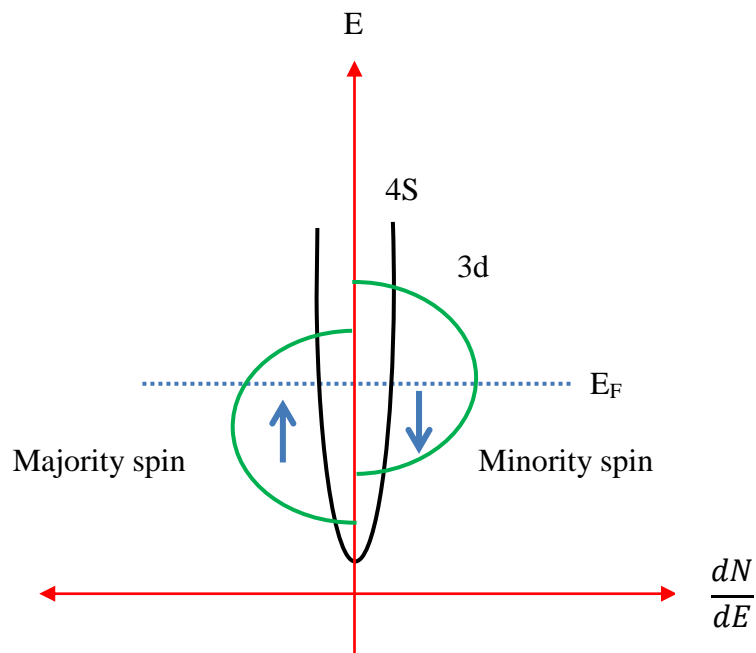


Figure (2.4): Diagram showing the band structure of the ferromagnetic metals. The 3d band is split into spin-up (majority) and spin-down (minority) causes a net magnetic moment per atom. The Fermi level E_F is represented by the dashed line.

Ferromagnetic materials obey the Curie-Weiss law above the critical temperature called Curie temperature T_c where above this temperature the ferromagnetic materials become paramagnetic. The susceptibility of the ferromagnetic material at $T > T_c$ is given by:

$$\chi = \frac{c}{T-T_c} \quad 2.20$$

The susceptibility has a positive value at $T > T_c$ but at T equal to T_c the susceptibility becomes infinite, which corresponds to the spontaneous order phase. This means that the ferromagnetic materials have spontaneous magnetisation even in the absence of the external magnetic field. However, a ferromagnetic material has zero initial magnetisation which indicates that ferromagnetic material consists of small regions called domains and the magnetic dipoles are aligned parallel in each domain. In the absence of an external magnetic field the magnetisation in different domains has a different orientation and then the total magnetisation average is zero. The process of magnetisation causes magnetic dipoles of all domains to orient in the same direction. The magnetisation of a ferromagnet is a complex function of the applied magnetic field and depends on the material's past history, as shown in fig. 2.5. The graph of magnetisation (M) versus magnetic field (H) shown in fig. 2.5 is known as a hysteresis loop. In an applied magnetic field, the magnetisation of the system increases as the field is increased until it reaches a maximum at the saturation magnetisation (M_s). When the magnetic field is reduced to zero after saturation, the magnetisation decreases to a certain value (M_r) called the remnant magnetisation. The reversed magnetic field required to reduce the magnetisation to zero is called the coercivity (H_C). The magnetisation and the susceptibility of ferromagnetic materials are temperature dependent as shown in fig.2.6. The saturation magnetisation reaches its maximum at absolute zero and vanishes above the Curie temperature (T_c).

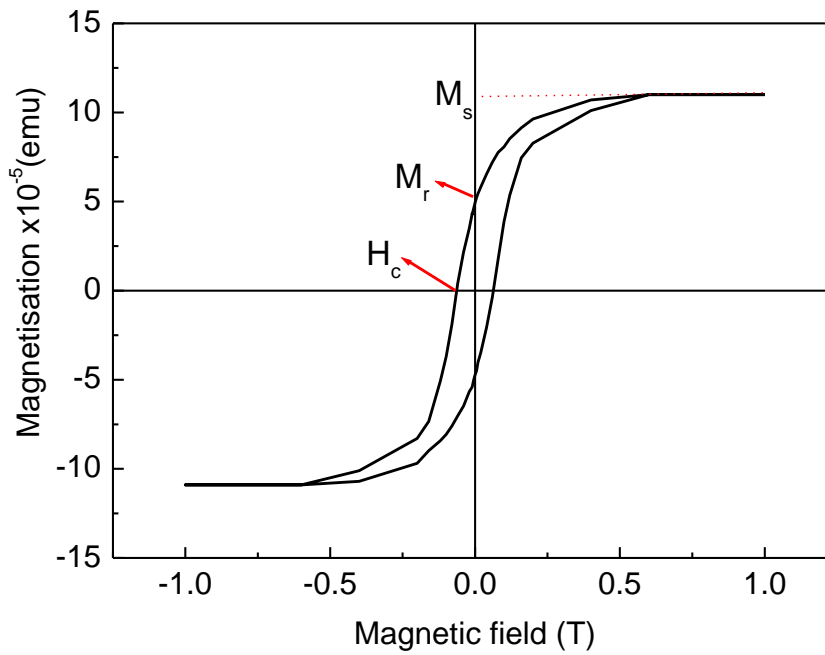


Figure (2.5): Variation of the magnetisation with magnetic field (hysteresis loop) for a ferromagnetic material. M_s denotes the saturation magnetisation, H_c the coercive field and M_r the remnant magnetisation.

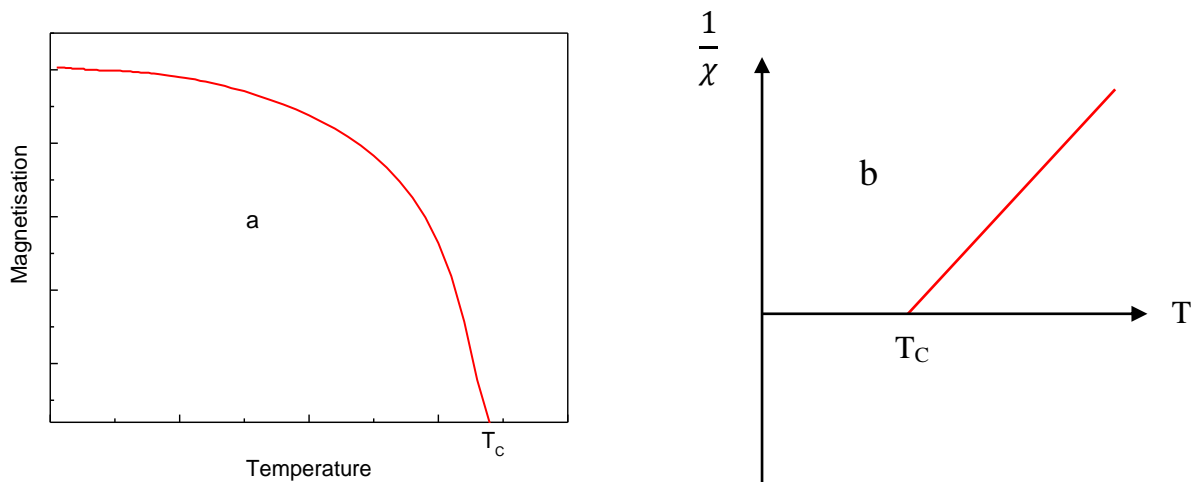


Figure (2.6): a) The magnetisation as a function of temperature for a ferromagnetic material. b) The inverse susceptibility as a function of temperature for a ferromagnetic material.

2.7 Anti-Ferromagnetism

In antiferromagnetic materials, half of the magnetic dipoles are aligned in one direction and the other half in the opposite direction. Below some critical temperature, called the Néel temperature (T_N), antiferromagnets are divided onto two identical magnetic ions sublattices. The magnetic moment on the first sublattice are polarised in one direction and the magnetic moment on the second polarised by the same amount in the opposite direction. The spins of atoms between nearest neighbours will be antiparallel at $T=0$. Accordingly, the net magnetic moment is zero and the spontaneous magnetisation is non-existent. The susceptibility of antiferromagnets is temperature dependent as shown in fig.2.7. Above the Néel temperature (T_N) the susceptibility is given by:

$$\chi = \frac{C}{T+\theta} \quad 2.21$$

Above T_N the moments are paramagnetic and below this temperature the moments are alternatively arranged parallel and antiparallel. Below the Néel temperature (T_N) the susceptibility decreases slightly with decreasing temperature.

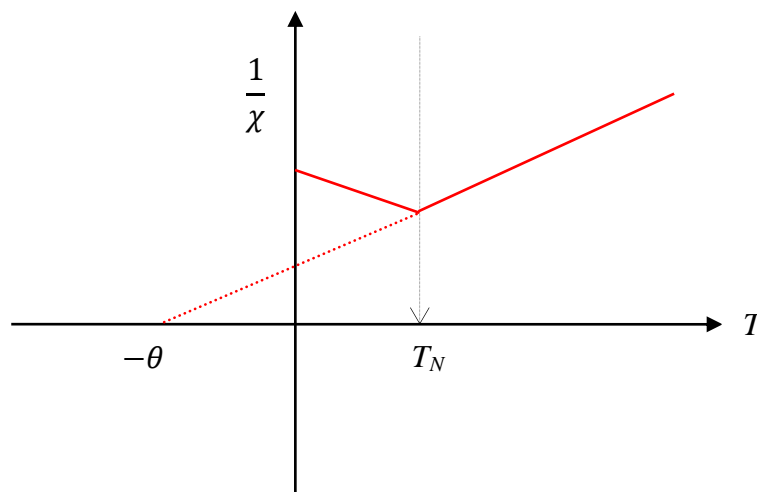


Figure (2.7): inverse susceptibility as a function of temperature in an antiferromagnet.

2.8 Exchange Interaction in Magnetic Systems

The magnetic and electrical behaviour depends on the interaction between the different atoms. There are many different exchange interactions that have been used to explain ferromagnetism in the magnetic system. These interactions can be divided into categories of direct and indirect interactions.

2.8.1 Direct Exchange Interaction

Direct exchange interaction occurs between spin on ions which are close enough to have sufficient overlap of their wave functions. If two single free atoms exist beside one another, with their respective lobes of charge density that correspond to different states. These lobes typically form an overlap region of charge density that will contribute to both atoms. The Pauli exclusion principle requires that no single electron state is occupied twice. Therefore, the electrons are then required to possess opposite spins. This gives rise to an antiparallel alignment and therefore the direct exchange interaction is antiferromagnetic. The direct exchange sign depends principally on the interatomic spacing and band occupancy with ferromagnetic exchange favoured at a larger spacing [4].

2.8.2 Indirect Interactions

It is not possible for coupling to take place through direct exchange if the ions, on which the magnetic moments are located, are situated with excessive space between them. The exchange must therefore take place in an indirect manner such as super-exchange, double exchange and RKKY exchange.

I Super-Exchange

Super-exchange is a coupling that occurs between two nearest-neighbour cations through a shared non-magnetic ion (e.g. oxygen). The transition metal oxides are a good illustration of the super-exchange interaction. In transition metal oxides the 3d-orbitals are hybridized with the 2p-O orbitals. Virtual hopping of O-2p electrons to the overlapping transition metal (TM) orbitals leads to excited states which can result in a reduction of the total energy of the system. The strength and the sign of the super-exchange interaction depend on the occupancy and orbital degeneracy of the 3d states. This can lead to antiferromagnetic or ferromagnetic behaviour as summarized below for $\text{La}^{3+} \text{Mn}^{3+} \text{O}_3^{2-}$ as an example [9].

- 1- The super-exchange interaction that occurs between the half-filled d-shell of Mn^{3+} ions and the fully occupied O-2p electrons is antiferromagnetic as shown in fig. (2.8 a). Since the hopping of the two O-2p electrons will reduce the system energy if the spins of Mn^{3+} ions on the either side of the anion (oxygen) are of opposite spin.
- 2- The super-exchange interaction is ferromagnetic if the two nearest-neighbour Mn^{3+} ions are connected at 90 degree to the oxygen ion. Since the hopping of the two O-2p electrons will reduce the system energy if the spin of Mn^{3+} core spins are parallel as shown in fig.2.8 b

**Removed by the
author for copyright reasons**

Figure (2.8): super-exchange interaction between the e_g orbital of two Mn^{3+} ions via the O-2p for $LaMnO_3$. Dependent on the occupation with electrons, the resulting interaction is a) antiferromagnetic b) ferromagnetic. Adapted from ref. [9].

II Double Exchange Interaction

The double exchange interaction (DE) was proposed by Zener [10]. It is a type of interaction that occurs indirectly between the spins of magnetic ions and needs mixed valence. The DE is responsible for ferromagnetism in the mixed-valence perovskite manganites where the extra electron of the Mn^{3+} ion travel back and forth between Mn^{3+} and Mn^{4+} ions and its spin is coupled with those of both ion cores. The

difference DE and super-exchange interaction is that the super-exchange interaction occurs between two atoms with the same valence (number of electrons). More details regarding DE are given in section 4.2 of chapter 4.

III RKKY Interaction

The Ruderman-Kittel-Kasuya-Yosida (RKKY) interaction [11] describes the magnetic interaction between localized d or f electron spins (magnetic ion) and the delocalized conduction band electrons (sp-band). Due to the direct exchange interaction the spin of one magnetic ion interacts with the close conduction electron. This conduction electron is then magnetised and acts as an effective field which influences the polarisation of the nearby magnetic ions. The polarisation decays in an oscillatory manner as the distance from the magnetic ion is increased. Consequently, a second magnetic ion can then couple parallel to the first magnetic ion, but only if there is a small separation of the magnetic moments. This model is efficient when a high concentration of delocalized carriers is present in the host material. The RKKY mechanism illustrates an interaction with much longer range than direct interaction, but the mechanism can vary widely in terms of strength, with minor changes in the magnetic moment separation.

2.9 A Brief History of Oxide Thin Films

The history of oxide thin films was intensely influenced by the development of the suitable deposition techniques [9]. Several techniques were used to grow epitaxial oxide thin films; these include techniques such as sputtering, molecular beam epitaxy (MBE) *etc.* However, no other growth method had such a high impact as the development of the novel pulsed laser deposition (PLD) technique in the late 1980s [9, 12-13]. Since the discovery of tunnelling magnetoresistance (TMR) on tunnel junctions based on manganese perovskite oxides [14-15], the interest has increased rapidly for the application of oxides in the field of spintronics. Among oxides materials that have been produced very large TMR are the half-metallic oxides [16-17]. Half-metallic behaviour in double-exchange oxides was predicted for Fe_3O_4 in 1984 [18], CrO_2 in 1986 [19], and Manganites in 1996 [20]. Mixed-valence manganites, such as $\text{La}_{0.67}\text{Sr}_{0.33}\text{MnO}_3$ (LSMO), are DE ferromagnets with a maximum Curie temperature T_C of 360 K [21]. Part of this thesis focuses on LSMO and a literature review of LSMO is presented in section 4.2 of chapter 4.

The discovery of ferromagnetism in Diluted magnetic semiconductors (DMSs) greatly increased research activity in this field. DMSs are a solid-solution of a non-magnetic semiconductor and magnetic element, as shown in fig. 2.9. In diluted magnetic semiconductors (DMSs) transition metals with unfilled d shells (Sc, Ti, V, Cr, Mn, Fe, Co, Ni and Cu) and rare earth elements with unfilled f shells (e.g. Eu, Gd and Er) have been used as magnetic elements. The content of magnetic element in a DMSs ranges from a few percent to several tens of percent [22-23]. The interaction between magnetic ions is critical where the absence of this interaction leads to paramagnetism of the DMSs. The ferromagnetism of a DMS can arise under certain condition such as changes in the density of free carriers, which can lead to exchange

interaction between magnetic ions. In a DMSs the delocalised valence band holes and conduction band electrons interact with the magnetic moment associated with the magnetic atoms [22].

**Removed by the
author for copyright reasons**

Figure (2.9): Two types of semiconductors a) a magnetic semiconductor b) a diluted magnetic semiconductors (DMS). Adapted from ref.[24].

A significant contribution to the research on DMSs was made by Slyn'ko *et al* in 1980s [25]. These workers, were the first to discover Fe magnetic ordered cluster in InSe and CdTe. The low Curie temperature and the difficulty in doping II-VI- based DMSs n-type and p-type made these materials less attractive for applications [22]. A breakthrough in the field of DMSs was in 1989 by Munekata *et al* [26] who

succeeded in doping a considerable amount of Mn into InAs using MBE. However, the Curie temperature T_C for this material was very low at about 7.5 K [26-27].

DMSs have been studied in depth both experimentally and theoretically. Dietl *et al* [28] calculated the Curie temperature for various wide band gap semiconductors as shown in fig. 2.10. It was predicted that the Curie temperature could exceed room temperature in p-type semiconductor-based- DMSs. This theoretical study encouraged several groups to work in this field. In addition to this, reports of room temperature ferromagnetism in Co-doped TiO₂ films [29] have encouraged experimental studies and intensive experimental work has begun on oxide- based DMSs.

**Removed by the
author for copyright reasons**

Figure (2.10): Calculated values of the Curie temperature T_C for various p-type semiconductors containing 5% of Mn atoms and 3.5×10^{20} holes/ cm³ [28].

Coey *et al*, considered a model assuming indirect exchange via shallow donors [30]. According to this model, high T_C required hybridization and charge transfer from the impurity band to the unoccupied 3d states at the Fermi level as shown in fig.2.11. Consequently, on passing along the 3d series of metals there are two regions

in which a high T_C is expected; one of these occurs when the $3d^\uparrow$ states cross the Fermi level in the impurity band at the beginning of the series (fig. 2.11 a), and the other occurs when the $3d^\downarrow$ states cross the Fermi level in the impurity band at the end of the series (fig.2.11 c).

**Removed by the
author for copyright reasons**

Figure (2.11): Schematic band structure of an oxide containing 3d impurity and spin-split donor impurity band. The position of the 3d level that leads to a high T_C is shown in (a, c). b) Shows the position of the 3d level that leads to a lower T_C . Adapted from ref. [30].

In order to examine the Coey model, thin films of ZnO all doped with 5% of each of the 3d TM element (Sc, Ti, V, Cr, Mn, Fe, Co, Ni, Cu and, Zn) were grown using PLD [30]. The results were in agreement with the model where the highest room temperature magnetisations (in μ_B/cation) occurred for Co, Fe, Ni, V, Ti and Sc, respectively. The magnetisation (in μ_B/cation) is near zero for Cr, Mn and Cu. However a significant room temperature magnetisation was reported [31-32] for a low concentration of Mn (2-3%) doped ZnO films.

Recently, In_2O_3 -based DMSs have attracted great attention as candidates for room temperature ferromagnetism and are expected to have the potential to widen the range of application due to the wide band-gap (3.75 eV) and are transparent in the visible region [33]. Part of this thesis focuses on TM doped In_2O_3 and a literature review of In_2O_3 is presented in section 7.2 of chapter 7.

More recently, a renewed interest in multiferroic materials in the form of thin films has provided novel opportunities for oxides in spintronics. Multiferroics brings novel physics phenomena and offers possibilities for new device functions due to the coexistence of several ferroic orders such as ferroelectricity and ferromagnetism [34]. Part of this thesis focuses on multiferroics and a literature review on multiferroics is presented in section 5.2 of chapter 5.

2.10 References

1. N. A. Spaldin, *Magnetic materials : fundamentals and device applications*. (Cambridge University Press, Cambridge, Uk ; New York, 2003).
2. C. Kittel, *Introduction to solid state physics*, 6th ed. (Wiley, New York, 1986).
3. K. H. J. Buschow and F. R. d. Boer, *Physics of magnetism and magnetic materials*. (Kluwer Academic/Plenum Publishers, New York, 2003).
4. J. M. D. Coey, *Magnetism and magnetic materials*. (Cambridge University Press, Cambridge, 2010).
5. D. G. Pettifor, *Journal of Magnetism and Magnetic Materials* **15-8** (JAN-), 847-852 (1980).
6. F. J. Himpsel, J. E. Ortega, G. J. Mankey and R. F. Willis, *Advances in Physics* **47** (4), 511-597 (1998).
7. O. Gunnarsson, *Journal of Physics F-Metal Physics* **6** (4), 587-606 (1976).
8. J. F. Janak, *Phys. Rev. B* **16** (1), 255-262 (1977).
9. M. Opel, *J. Phys. D-Appl. Phys.* **45** (3) (2012).
10. C. Zener, *Physical Review* **82** (3), 403-405 (1951).
11. K. Yosida, *Theory of magnetism*. (Springer, Berlin ; New York, 1996).
12. H. M. Christen and G. Eres, *Journal of Physics: Condensed Matter* **20** (26), 264005 (2008).
13. L. W. Martin, Y. H. Chu and R. Ramesh, *Materials Science and Engineering: R: Reports* **68** (4–6), 89-133 (2010).
14. M. Bibes and A. Barthelemy, *IEEE Trans. Electron Devices* **54** (5), 1003-1023 (2007).
15. Y. Lu, X. W. Li, G. Q. Gong, G. Xiao, A. Gupta, P. Lecoeur, J. Z. Sun, Y. Y. Wang and V. P. Dravid, *Phys. Rev. B* **54** (12), R8357-R8360 (1996).

16. J. M. D. Coey and M. Venkatesan, *J. Appl. Phys.* **91** (10), 8345-8350 (2002).
17. J. M. D. Coey and S. Sanvito, *J. Phys. D-Appl. Phys.* **37** (7), 988-993 (2004).
18. A. Yanase and K. Siratori, *J. Phys. Soc. Jpn.* **53** (1), 312-317 (1984).
19. K. Schwarz, *Journal of Physics F-Metal Physics* **16** (9), L211-L215 (1986).
20. W. E. Pickett and D. J. Singh, *Phys. Rev. B* **53** (3), 1146-1160 (1996).
21. M. Imada, A. Fujimori and Y. Tokura, *Rev. Mod. Phys.* **70** (4), 1039-1263 (1998).
22. C. Liu, F. Yun and H. Morkoc, *J. Mater. Sci.-Mater. Electron.* **16** (9), 555-597 (2005).
23. G. V. Lashkarev, M. V. Radchenko, V. A. Karpina and V. I. Sichkovskiy, *Low Temp. Phys.* **33** (2-3), 165-173 (2007).
24. H. Ohno, *Science* **281** (5379), 951-956 (1998).
25. V. V. Slynko and R. D. Ivanchuk, *Ukr Fiz Zh+* **26** (2), 221-223 (1981).
26. H. Munekata, H. Ohno, S. von Molnar, A. Segmüller, L. L. Chang and L. Esaki, *Physical Review Letters* **63** (17), 1849-1852 (1989).
27. K. Kagami, M. Takahashi, C. Yasuda and K. Kubo, *Sci. Technol. Adv. Mater.* **7** (1), 31-41 (2006).
28. T. Dietl, H. Ohno, F. Matsukura, J. Cibert and D. Ferrand, *Science* **287** (5455), 1019-1022 (2000).
29. Y. Matsumoto, M. Murakami, T. Shono, T. Hasegawa, T. Fukumura, M. Kawasaki, P. Ahmet, T. Chikyow, S. Koshihara and H. Koinuma, *Science* **291** (5505), 854-856 (2001).
30. J. M. D. Coey, M. Venkatesan and C. B. Fitzgerald, *Nat. Mater.* **4** (2), 173-179 (2005).

31. M. Ivill, S. J. Pearton, D. P. Norton, J. Kelly and A. F. Hebard, *J. Appl. Phys.* **97** (5), 053904-053905 (2005).
32. P. Sharma, A. Gupta, K. V. Rao, F. J. Owens, R. Sharma, R. Ahuja, J. M. O. Guillen, B. Johansson and G. A. Gehring, *Nat Mater* **2** (10), 673-677 (2003).
33. M. Venkatesan, R. D. Gunning, P. Stamenov and J. M. D. Coey, *J. Appl. Phys.* **103** (7) (2008).
34. M. Bibes and A. Barthelemy, *Nat. Mater.* **7** (6), 425-426 (2008).

Chapter 3

Experimental Methods

3.1 Introduction

This chapter describes the experimental techniques, the sample preparation and the characterisation measurements that have been the basis of this work. This will involve the procedure for production and measurement of thin film's thicknesses and magnetic moments. This chapter will also provide a brief discussion on the basics of the magneto-optics. It also describes the procedure for the measurement of the optical and magneto-optical properties of the samples. The introduction to the magneto-optics basics was obtained by referring to the following text books: "Optical properties of Solids" by A.M.Fox [1] and "Magnetic Materials Fundamentals and Device Applications" by N.A.Spaldin [2].

3.2 Target and Film Preparation

Our ultimate aim was the growth of thin films. These films were ablated from bulk targets using an excimer (XeCl); a technique known as pulsed laser deposition (PLD). The targets were prepared before ablation; we now describe the method of production. Stoichiometric amounts of the appropriate powders were weighed-out using an accurate balance. The requisite amounts of powders was mixed together and ground for 20 minutes in a mortar and pestle. This powder-mix was then annealed for about eight hours in air in a furnace. The resulting powders were then re-ground and re-fired at a higher temperature for the same length of time in order to optimise the

reaction of components to form the oxide compound. After the final anneal, sufficient powder was placed in a commercial die of internal diameter 25 mm and pressed to 25000 kPa in vacuo to yield a pellet of about 5 mm thickness. This pellet was then sintered again at increasing temperatures for various lengths of time. The final result was a high density, a smooth-surfaced target, which was then subsequently used in the laser ablation chamber.

3.3 Pulsed Laser Deposition

There are several alternative techniques that can be employed to produce high-quality thin films and multilayers. Examples of these techniques are molecular-beam epitaxy (MBE), sputtering [3-4] or metal organic chemical vapour deposition (MOCVD), aqueous deposition and (PLD) [3, 5-6] . The PLD technique is now widely used for the growth of metal oxide films. It is a suitable laboratory technique for growing high- quality epitaxial layers directly from a ceramic target. PLD was first developed by Cheung *et al* and has been mostly employed for sequential deposition of compound semiconductors [7].

3.3.1 Excimer Laser

In discussing different kinds of lasers, identification is made by the material undergoing the laser process. There are four categories of lasing materials: solid, gas, liquid, and semiconductor [8]. According to these categories there are many different types of laser available for many different uses and the excimer laser is a pertinent example [9]. The effect of laser beam on a target is affected by three variables: power, spot size, and time. The change of energy with power and time are proportional while that of spot size is an inverse square.

A pulsed laser, of which an excimer laser is an example, delivers its energy in the form of a single pulse or train of pulses [8]. Laser light emitted from a standard device is generally characterized in terms of power, in units of watts. The energy in Joules is defined as a power in watts multiplied by the time (sec). Pulsating laser energy is calculated for each pulse as in CW. The average power (P_{avg}) produced by a train of pulses is determined by multiplying the pulse power (p) by the pulse repetition rate (f) and the pulse width (Δt) [10-11] as following:

$$P_{avg} \text{ (Watt)} = p \text{ (W)} \times f \text{ (Hz)} \times \Delta t \text{ (sec)} \quad 3.1$$

3.3.2 Basics Excimer Laser

The word excimer is a contraction of the two words, excited dimer. The excimer laser was invented in 1970 by Nikolai Basov. In an excimer laser the lowest energy state of the molecules is not bound but repulsive. The excited state is a bound state which is induced by an electrical discharge or high-energy electron beam. The excimer laser action can then be produced on the transition between the upper state (bound state) and the lower state (free state) [8-9].

An excimer laser typically uses an inert gas such as argon (Ar), krypton (Kr) or xenon (Xe) to combine, in the excited state, with a halogen atom such as fluorine (F) or chlorine (Cl) to form a rare-gas-halide excimer [9]. The typical laser used for growth is the excimer with KrF at the wavelength of 248nm, XeCl at 308 nm or ArF at 193 nm, all values lying in the ultra violet UV. Most materials used in film growth exhibit strong absorption in the region of the laser wavelength range from 200 nm to 400 nm [3, 12-14]. Fig.3.1 shows the potential energy diagram as a function of atomic

separation for the production of an excimer AB^* . This formation is created by the collision of an excited atom A^* with B or by the collision of a positive or negative ion A^+ and B^- [15]. Here, the potential is always repulsive in the lowest energy state, whilst the excited states exhibit a minimum energy at one separation. Consequently, the population inversion is easily achieved due to the low population in the ground state. Furthermore, even when lasing commences, the ground state population remains low because the ground state is inherently unstable [8].

**Removed by the
author for copyright reasons**

Figure (3.1): Potential energy curves showing the formation of the excimer AB^* [8].

The fundamental, avalanche electric discharge circuit layout is illustrated by fig.3.2. This comprises a pair of electrodes, a storage capacitor and inductive coils. The plasma tube contains the gaseous medium at high pressure. In order to produce the laser, a high potential is applied to charge the storage capacitor to approximately 40 kV. Subsequently the thyatron switch is fired, meaning the energy is transferred to

the peaking capacitors over about 100 ns. The energy is then transferred to the discharge area as the peaking capacitors become fully charged, and the time duration of this transfer is 20-50 ns [12, 16].

**Removed by the
author for copyright reasons**

Figure (3.2): Schematic diagram of an excimer discharge circuit design, where C_1, C_2 are the storage capacitor and peaking capacitor respectively. Adapted from ref.[16].

3.3.3 Mechanisms of Pulsed Laser Deposition

The principle of pulsed laser deposition is a very complex physical phenomenon, involving the transfer of energies. The target surface absorbs the laser beam energy and converts the energy to electronic excitations and then to thermal, chemical, and mechanical energies. When the laser beam is incident on the surface of the target the elements in the target are rapidly heated up to their evaporation temperature. The materials are dissociated from the target surface and ablated out with stoichiometry corresponding to that in the target. A plasma plume is then created

when the laser ablates on to the target surface. After that, the material expands in the plasma toward the substrate due to the Coulomb repulsion and recoil from the target surface. The plasma condenses on the heated substrate [3]. The plasma plume distribution and the plasma shape depend on the background pressure. It has been observed that the shape of the plasma plume changes as a result of changes of the oxygen pressure; this is due to chemical interactions between the oxygen and the ablated species [17-18]. The film properties are strongly influenced by the deposition condition such as oxygen pressure, deposition temperature (substrate temperature) and laser fluence. When the condensation rate is sufficiently high, a thermal equilibrium can be reached and the film grows on the substrate surface at the expense of the direct flow of ablation particles and the thermal equilibrium obtained [19-22]. Fig.3.3 illustrates the formation stages of the thin film by PLD.

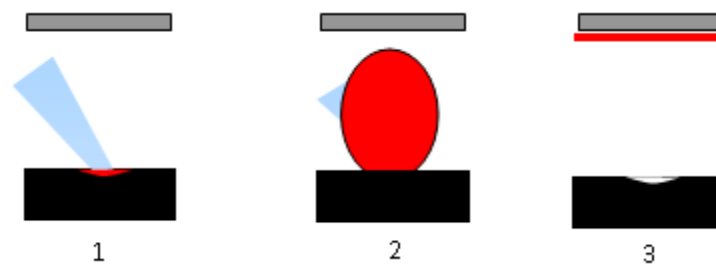


Figure (3.3): Shows the stages of formation the thin film by PLD. (1)- Laser-target interaction, (2) laser plasma interaction and plasma expansion and (3) film deposition.

3.4 Growth of Thin Films and PLD System

The PLD system shown in fig. 3.4 consists of three main components: the laser, the optical system and the deposition chamber. A LEXTRA 200 excimer laser was used to deliver the laser beam at a wavelength of 308 nm. The laser currently being used produces a pulse of energy of up to 400 mJ with a pulse length of about 28 ns and a repetition rate of 10 Hz. The optical arrangement consists of a quartz lens which focuses the laser beam onto the target surface. This lens is mounted on a rail between the laser and the deposition chamber. The beam is focused so as to be incident on the target at 45° and a spot size of about 3 mm² is formed.

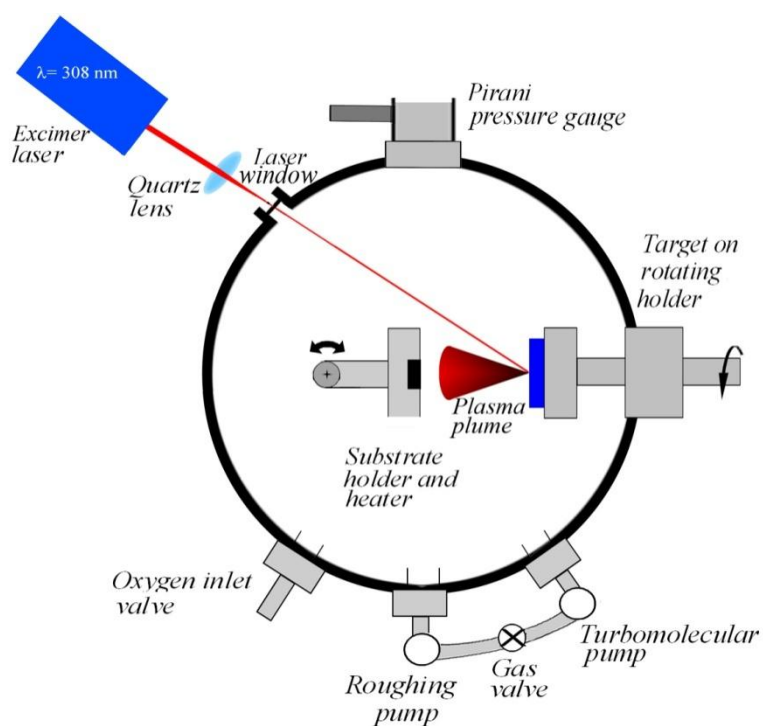


Figure (3.4): Schematic diagram of the PLD laser deposition chamber.

The deposition chamber is a stainless-steel, high-vacuum compartment containing the target and substrate holder. Removing the stainless-steel lid gives access to the inside of the main chamber. The inside of the main chamber is comprised of three main sections: the target holder, the substrate holder, and the pressure gauge unit. The target holder can be rotated, and is driven by an electric motor on a rotary feed-through. This rotation prevents the same spot from being continually ablated and therefore reduces the formation of splashing on the substrate. The chamber also has a quartz window through which the laser passes onto the target.

The substrate holder consists of two electric heater-elements sandwiched between two thin stainless-steel plates. The substrate is completely cleaned with ethanol and clamped to the upper plate of the substrate holder. The holder position for the substrate remains constant, (about 35 mm from the target) even though its position can be altered. The substrate temperature depends on the material being ablated. Some materials were grown at room temperature, whereas for other materials we need to heat the film to high temperature in *vacuo* [23-24].

Once in position, the deposition chamber is sealed and pumped-down to the required pressure. The deposition chamber is evacuated using a turbo-molecular pump (TMP) in conjunction with a rotary pump in order to reach a minimum base pressure of 10^{-5} Torr. The pressure inside the chamber can be varied from base to a pressure of a few hundred mTorr, when a gas is leaked into the chamber in a controlled manner. The pressure inside the chamber in the latter case is controlled by three valves: a gas valve, a roughing pump valve and gate-valve and is continuously monitored by a pressure gauge. Oxygen gas can be filled back into the chamber via the gas valve and the gas pressure is controlled by a careful balance between the gate-valve and oxygen-inlet. When the desired pressure is greater than 10 mTorr, the

pressure is controlled by a careful balance between roughing pump valve and oxygen inlet gas valve whilst the TMP gate valve remained shut.

In order to promote film growth, the laser beam is aligned and pulsed onto the target for several minutes. The deposition time is determined by the desired film thickness, which is also affected by the quality of the plume.

During film deposition, the deposition conditions, such as oxygen pressure, deposition temperature and laser fluence, were held constant at all times. Finally, when the deposition is finished, the film can be either rapidly quenched or left to cool down to room temperature for some hours.

A film's composition usually assumed to be that of the respective target, although there are essentially two possible sources of error in determining whether an ablated film's composition differs from its nominal value. The first error arise in the target preparation, the second error arise in the film deposition. The error in the composition of the target is quite small, since the required amount of the various powders have been weighted-out using a very accurate electronic balance then the powders are ground together to form a uniform concentration powder. The error arising during ablation of the target is difficult to assess. Earlier work [25-26] has suggested that the concentration of transition metal ions in an ablated film is somewhat higher than in the target. It has been suggested that this could be due to preferential sputtering of the host cation. However, it is also possible that a greater error is the reproducibility of the films caused by the small changes in deposition conditions between the ablation of successive films [27]. In order to make a quantitative assessment of the error between actual and nominal film concentration, it is necessary to have an analyses of the ablated film. In the present work, an error of about 60% was found for Co doped In_2O_3 and 14% for Fe-doped In_2O_3 .

3.5 Measuring Film Thickness- Dektak Surface Profiler

A Dektak surface profiler is essentially a mechanical lever connected to an optical lever and controlled by a PC. Its purpose is to record precise measurements of small, vertical features.

A stylus on the Dektak is transported along the film surface, and as it moves along the sample, its vertical movement is recorded. In order to measure the film thickness using the Dektak stylus, film-free areas in the corners of the film can be generated during the deposition procedure, when the substrate is clamped to the holder as shown in fig. 3.5.

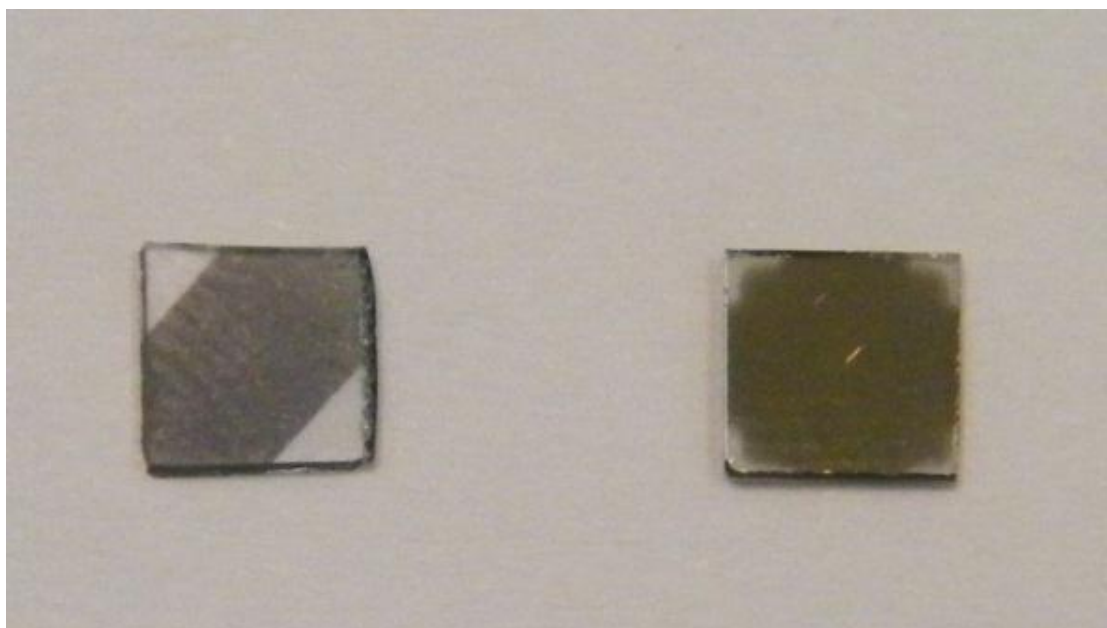


Figure (3.5): The free areas in the substrate corners generated during the deposition procedure.

It is possible to alter the range of force used when pressing the stylus onto the sample. The height of the stylus can be changed in relation to the work stage by a micrometer screw. When the vertical displacement of the stylus is adjusted, the stylus is then directed from the film-free area toward the middle of the film. The change in the vertical position of the stylus results in a varying electrical inductance. The inductance data that it produces is recorded and translated to a height, before being plotted as a function of horizontal distance. In order to measure the thickness value a few measurements are made, and an average is calculated. Fig.3.6 shows an example of the data recorded by the Dektak.

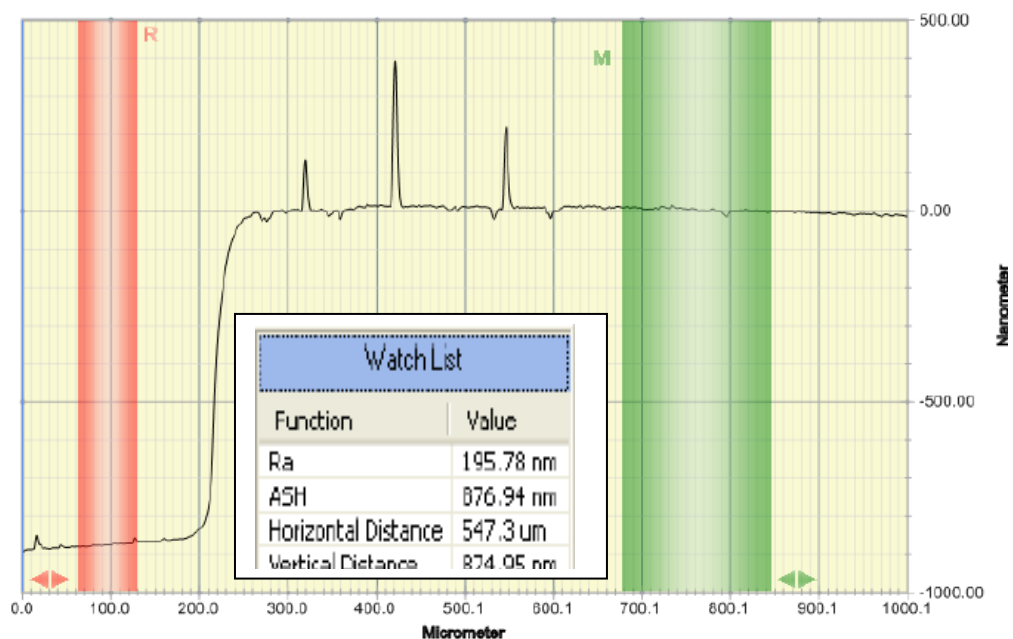


Figure (3.6): Film thickness data as measured by the Dektak surface profiler for an LSMO thin film. The thickness of the film is the difference between the green and the red line which are located on the film surface and on the substrate surface respectively. The inset shows the thickness of 876.94 nm.

It is estimated that the error from the Dektak is about 10% [14]. Also the horizontal resolution of the Dektak depends on the scan length and scan speed.

The thickness of the film may vary from region to region depending on the substrate and the shape of the deposition plume; this is the main problem in the Dektak measurement. It has been found that the lanthanum aluminate (LaAlO_3) substrate is twinned during growth so that the film thickness at the centre is greater than the thickness at the edge. On the other hand, films that were grown on sapphire substrates could be measured without any difficulty [14, 28-29].

Film thickness depends on the deposition time. Fig. 3.7 shows film thickness as a function of deposition time for $\text{La}_{0.7}\text{Sr}_{0.03}\text{MnO}_3$ films that we have grown on a SrTiO_3 (STO) substrate.

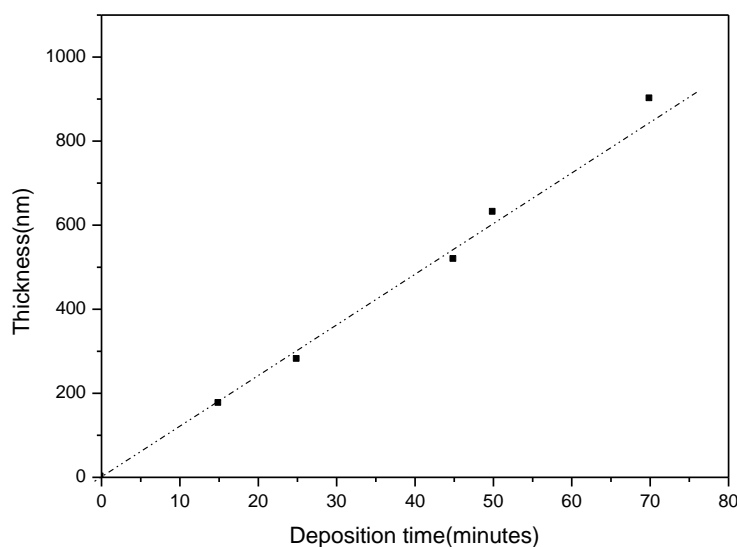


Figure (3.7): Thickness of $\text{La}_{0.7}\text{Sr}_{0.03}\text{MnO}_3$ films grown on STO substrates as a function of deposition time. All other parameters, laser fluence, oxygen pressure, substrate temperature were held constant.

3.6 Measuring Magnetisation-SQUID Magnetometer

SQUID is an acronym of superconducting quantum interference device. It is one of the most sensitive detectors which use the properties of Josephson junctions to detect very small magnetic fields. This device has a field resolution at the 10^{-17} T. There are two kinds of SQUID, DC (direct current) and RF (radio frequency). The DC SQUID was invented in 1964 and it has two Josephson junctions parallel in superconducting loop. The RF SQUID was invented in 1965 and works with only one Josephson junctions [30-31]. All of the measurements on our samples were obtained using an RF SQUID magnetometer model MPMS-5 manufactured by Quantum Design. The SQUID has a number of applications, due to its extreme sensitivity and ability to detect small magnetic fields, and examples of these include material property measurements and bio-magnetism. There are several excellent reviews available on the SQUID and its applications [30, 32-33].

3.6.1 SQUID Fundamentals

Fundamentally, a SQUID operates on the basis of measuring a voltage induced by the magnetic field from a sample in a field-sensing coil [33]. The RF SQUID system consists of superconducting material ring of self-inductance L , interrupted by a single weak link of critical current. If a magnetic field is applied through the ring in its normal state, i.e. not superconducting, magnetic field would penetrate the material in the ring as usual. The ring becomes superconducting when the temperature of the ring is reduced and the field will be expelled from the body of the material. When the magnetic field has been removed, the flux threading the ring centre will remain trapped due to the induced surface current. The trapped flux is quantized in multiples of $h/2e$ called fluxons where one fluxon is equal $2.068 \times 10^{-15} \text{ Tm}^2$ [30, 34]. Super

conducting ring has a relatively large critical current, above which the superconducting state is destroyed. If the superconducting ring is interrupted by an extremely thin layer of insulating material (weak link), there is a possibility of electron pairs tunnelling through insulating materials. In this state the ring would be superconducting but the critical current would be reduced by the weak link, typically to about 50 μA [35].

The system consists of set of superconducting pick-up coils located in a uniform magnetic field. The superconducting circuit is inductively coupled with the SQUID via superconducting transformer, which is inductively coupled itself with the LC resonant tank circuit. The tank circuit is resonant at about 15 MHz. The sample moved in discrete steps through the pick-up coils. This causes a change in flux in the coils which is proportional to the sample's magnetic moment. Any change in the input coil current will induce a change in the current flowing in the SQUID ring. The output signal is then detected in the output SQUID sensor. A least-squares fitting program converts the variation in flux to a theoretical expression that gives a magnetisation value [30-31, 34, 36-37]

3.6.2 Sample Handling and SQUID Operation

The sample is mounted directly into a large uniform plastic straw or by placing the sample in a gelatine capsule as shown in fig.3.8. After that the straw containing the sample is attached to the brass end of a stainless-steel sample rod (sample holder) which is then introduced into the SQUID via an access port situated in the top of the SQUID system.

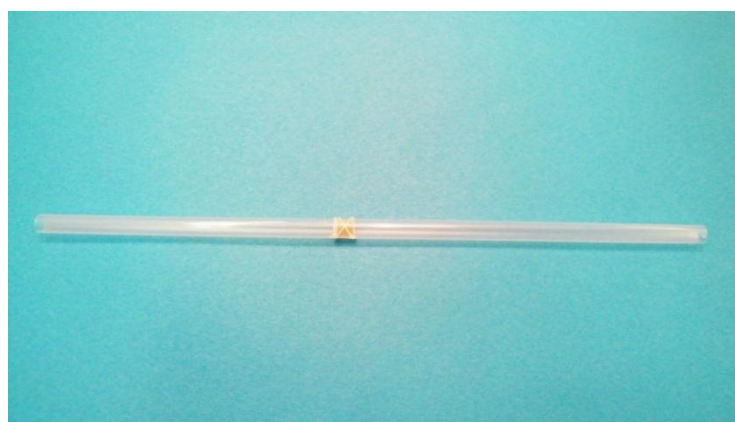


Figure (3.8): The sample is mounted in the plastic straw before attaching it to the end of the SQUID sample-holder.

An air-lock is used to introduce the sample into the SQUID; this prevents contamination of the He gas in main body of the SQUID. The sample is then positioned so as to be at the centre of a set of pick-up coils, which enable the magnetic moment of the sample to be determined. These pick-up coils are wound in the form of a second-order gradiometer, so as to reject, to large extent, extraneous signals and unwanted noise.

There are several measurement programs that have been used in the course of the present work, these include:

- Zero field-cooled (ZFC)
- Field-cooled (FC)
- Hysteresis loop

Firstly, the ZFC sequence is used when the sample is cooled in zero magnetic field. A small field is then applied (about 0.1 T) and the sample measured in temperature range from 5 K to 300 K (warming-up). Secondly, FC sequence is used when the sample is cooled down in a field and the magnetisation is measured in the required temperature range. Fig.3.9 shows ZFC/FC measurement that has been made on a $[\text{ZnO}(0.7 \text{ nm}):\text{CoFe}(0.6 \text{ nm})]_{60}$ multilayer film, which is grown on glass substrate. This film was grown in Prof. Xu's laboratory in Shanxi Normal University Linfen, China.

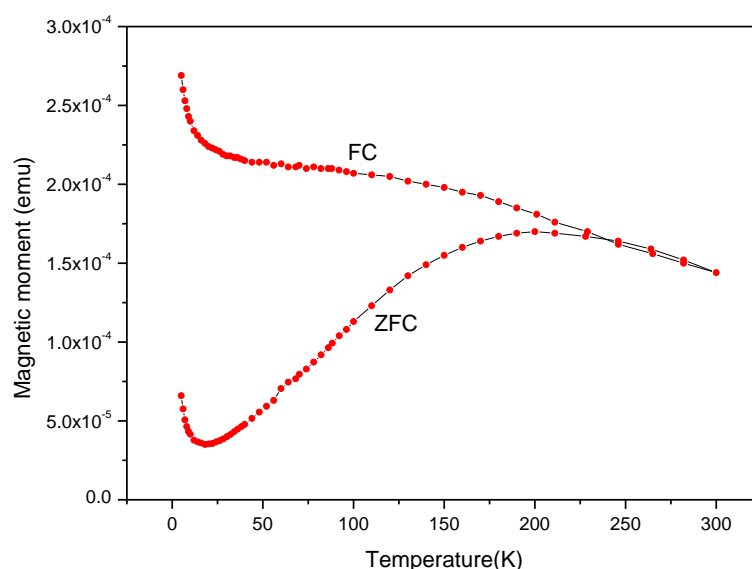


Figure (3.9): Shows the ZFC and FC measurement of a $[\text{ZnO}(0.7 \text{ nm}):\text{CoFe}(0.6 \text{ nm})]_{60}$ multilayer film which is grown on a glass substrate.

The magnetisation of the sample is measured as a function of external field. The subsequent plot will consist of both a contribution from the sample and also one from the substrate. Fig.3.10 shows the raw SQUID data that has been measured for $\text{Fe}_{0.05}(\text{In}_2\text{O}_3)_{0.95}$ grown on a sapphire substrate. This raw data exhibits three main contributions: diamagnetic contribution from the substrate, ferromagnetic contribution from the film and also a possible paramagnetic contribution from some part of the film due to unreacted components.

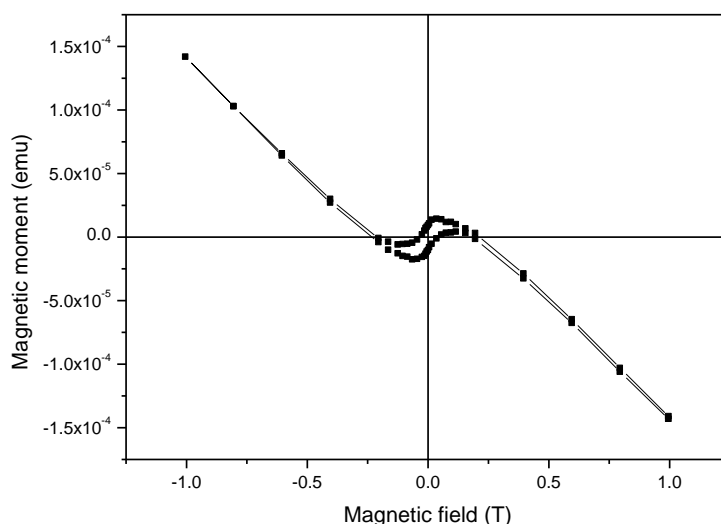


Figure (3.10): The raw SQUID data for a $\text{Fe}_{0.05}(\text{In}_2\text{O}_3)_{0.95}$ film grown on sapphire and measured at room temperature.

The ferromagnetic component is saturated at higher fields about 0.3 T. This means that the ferromagnetic component makes a constant contribution to the raw SQUID data at these fields. This fact enables us to separate the ferromagnetic contribution from the others. This can be achieved by calculating the slope of the straight line to each of the high-field regions then subtracting it from each point to

leave the ferromagnetic contribution as indicated in fig.3.11. The inset in this figure displays the diamagnetic component.

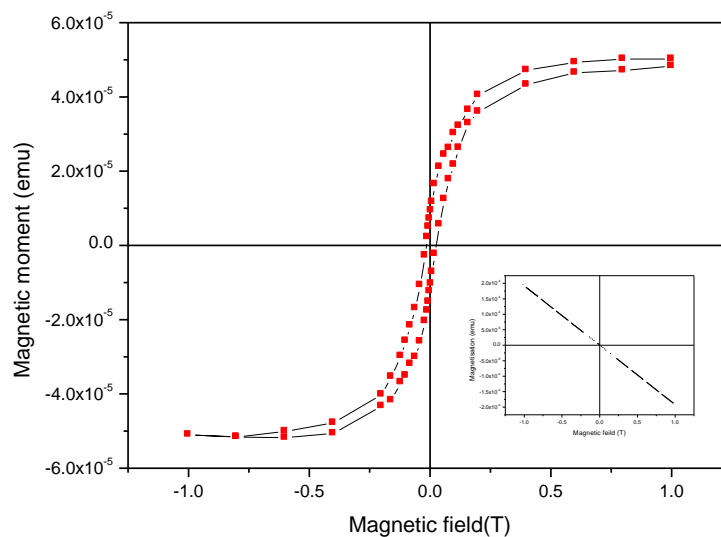


Figure (3.11): The room temperature SQUID data for a $Fe_{0.05}(In_2O_3)_{0.95}$ sample after subtraction of diamagnetic contribution from the substrate. Inset is the linear, subtracted component.

There is in fact also a possibility of a paramagnetic contribution from the film, which would also give a high-field linear dependency. It is not easy to separate the paramagnetic and diamagnetic contributions. However, it can be calculated by determining the signal per unit mass for the blank substrate then scaling this signal for the mass of the film substrate to have the diamagnetic contribution. The paramagnetic contribution is then calculated by subtracting the diamagnetic part from each point to leave the paramagnetic contribution.

3.7 Magneto-Optics Basics

Magneto-optics is a phenomenon which occurs when the light interacts with magnetically polarized materials. It is used to investigate the way light is modified when passed through a magnetic crystal. If light passing through an absorbing material of thickness, l , the material will have a complex refractive index, \tilde{n} , that has real and imaginary parts. We can write:

$$\tilde{n} = n_0 + i\kappa, \quad 3.2$$

where κ is called the extinction coefficient and is related to the absorption coefficient α . If the light has a wavelength λ then α is given by:

$$\alpha = \frac{2\kappa\omega}{c} = \frac{4\pi\kappa}{\lambda} \quad 3.3$$

In this case the light wave vector k can be written in terms of angular frequency ω and refractive index \tilde{n} as:

$$k = \frac{\omega\tilde{n}}{c} \quad 3.4$$

Linearly polarised light can be considered to comprise of two oppositely circular polarised components: right circularly polarised light (RCP) and left circularly polarised light (LCP) as shown in fig. (3.12). Therefore equation 3.2 may be written as:

$$\tilde{n}_{\pm} = n_{0\pm} + i\kappa_{\pm}, \quad 3.5$$

where (+) refers to RCP and (-) refers to LCP light. The RCP and LCP components have the same magnitude but the vectors rotate in the opposite directions to each other. If the linearly polarised light passes through a magnetic medium the magnitude of the RCP and LCP differ from one another as shown in fig.3.12. In this case the refractive index of the RCP and LCP light are not equal, $\tilde{n}_+ \neq \tilde{n}_-$. This results in a

phase difference between the internal and final planes of polarisation which is called circular birefringence or Faraday rotation. This is given by:

$$\theta_F = \frac{\omega l}{2c} (\Delta n) = \frac{\omega l}{2c} (n_+ - n_-), \quad 3.6$$

where c is the velocity of light in free space, ω is the angular frequency and l is the thickness of the magnetic medium. In the case of an absorbing magnetic medium the components of the extinction coefficient κ_+ and κ_- differ from one another. This leads to difference in the absorption of RCP and LCP at a frequency ω , which causes plane polarized light to become elliptically polarized; this is known as magnetic circular dichroism (MCD), which is given by:

$$MCD = \frac{\omega l}{2c} (\Delta \kappa) = \frac{\omega l}{2c} (\kappa_+ - \kappa_-) \quad 3.7$$

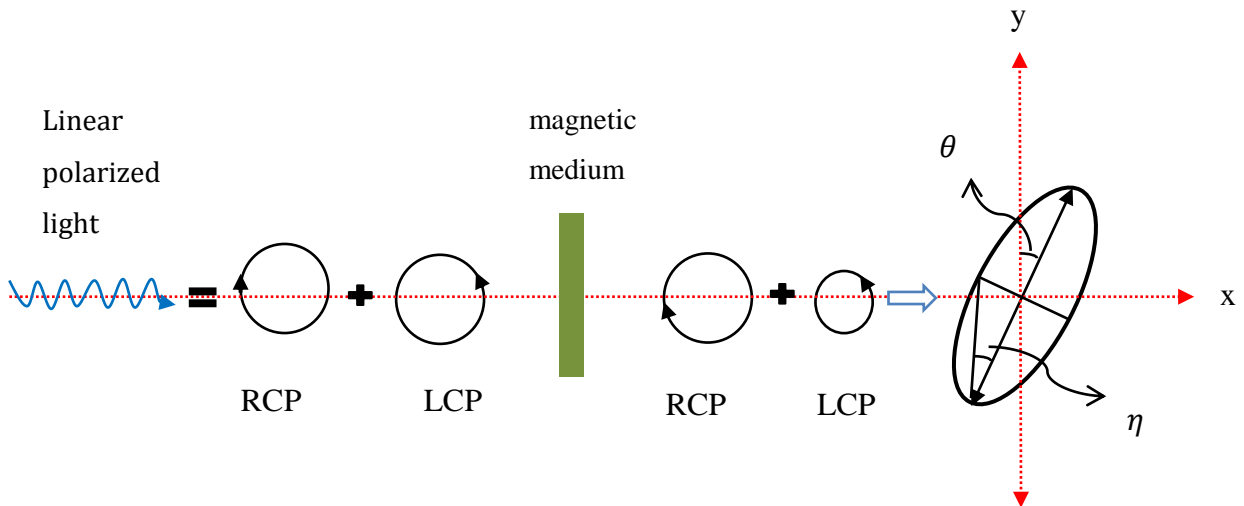


Figure (3.12): Linearly polarised light made up of equal components of RCP and LCP is incident on a magnetic medium; the transmitted or reflected light becomes elliptically polarised and rotated.

Opaque samples are usually studied by reflection where the plane of polarisation of the light is rotated as it reflected from a magnetised sample; this phenomenon is known as the Kerr effect. In measurement where the light is transmitted through the magnetised sample, the plane of polarisation of the light beam is rotated; this phenomenon is called the Faraday effect.

3.8 Magneto-Optics Set-up and Principles of the Technique

The set-up for measuring the magneto-optical effects is based upon the Katsuaki Sato method [38]. This technique allows the simultaneous measurement of the magnetic circular dichroism (MCD) and rotation (θ) of the sample. In addition, this technique can give a high sensitivity of 0.002° at 500 nm and resolution of 12 nm.

Fig. 3.13 shows a schematic diagram of the magneto-optics set-up which can be altered between Kerr and Faraday geometry. The Kerr geometry is the most appropriate geometry to be used when the sample is highly absorbing and effectively opaque, whereas the Faraday geometry is used when the sample is transparent.

In this set-up either a tungsten or xenon lamp with powers of 150 Watt and 250 Watt were used to cover a wide range of spectra of 0.6-3.8 eV and 1.5- 4.5 eV respectively. The light from the appropriate source is then aligned to pass through a Spectro-275 spectrometer in order to give monochromatic light. The required wavelength can be obtained by selecting between three different diffraction gratings blazed at different wavelengths. In order to remove the unwanted wavelengths, the light was filtered using a band-pass filter. The light was then passed through a Glan-Taylor UV prism polariser to yield the required plane polarised light to pass through the sample.

Removed by the author for copyright reasons

Figure 3.13: Schematic diagram of magneto-optics setup in either Faraday or Kerr geometry. Adapted from ref. [36].

The sample was mounted either on a room temperature sample holder or on cold-finger cryostat with optical-window/aperture. The sample is then placed vertically between the poles of an electromagnet which provides a magnetic field of 1.8 T and 0.5 T for room temperature and low temperature measurement respectively. This difference in the value of the field is due to the fact that the magnet pole-piece separation had to be increased for low temperature measurement in order to

accommodate the cryostat tail-piece. At low temperature measurement, the cryostat is evacuated for about 30 minutes before introducing liquid helium to cool the sample down. An Oxford ITC⁰³ temperature controller was used to set specific temperatures and measurements could be made over the range from 5 to 400 K. The polarised light is then focused and aligned to a similar size of aperture, then reflected or transmitted through the sample onto the photoelastic modulator (PEM). A series of mirrors and lenses is manoeuvred and used to achieve the optimal alignment so as to keep the maximum amount of the light passing through the sample and reduce the scattering within the pole-pieces, which affect the sensitivity of the experiment.

The PEM produces a signal which is proportional to the ellipticity and rotation of the light. The PEM is a piezo-birefringent modulator which consists of a birefringent crystal mounted on a piezo-vibrator with modulating frequency, f . The birefringent crystal vibration causes advancement and retardation in the phase of the traversing light parallel to the vibration direction [39]. The direction of the birefringent crystal vibration is set at 45° to the polariser and the modulation of the retardation is set to a quarter of the light wavelength. This means that the light emerging from the PEM alternates between RCP and LCP with frequency, f . The sample will then introduce oscillations, with a frequency f or $2f$, in the light intensity, if it exhibits any MCD, or rotation, whereas the light intensity will remain constant if the sample shows no magneto-optics effect.

The light is then passed through an analyser and focused onto the photomultiplier (PMT). This detector converts the light intensity to an electrical signal then feeds it to a conditioning unit to amplify the signal and split it into an AC and a DC component. The DC component is recorded using a Keithley voltmeter which can be controlled via the gain of the PMT. This component has to be constant in order to

maintain a constant sensitivity. The AC component is recorded using two signal-recovery lock-in amplifiers. The voltmeter and lock-in amplifiers, one and two, are used to measure the intensities I_0 , I_{1f} and I_{2f} respectively.

These three intensities, I_0 , I_{1f} and I_{2f} , have been calculated by Sato [38] and are given in the following equations:

$$I_1(0) = I_0 T [1 + J_0(\delta_0) \sin(\Delta\theta + 2\varphi)] \quad 3.8$$

$$I_2(f) = I_0 \Delta T J_1(\delta_0) \quad 3.9$$

$$I_3(2f) = 2I_0 T J_2(\delta_0) \sin(\Delta\theta + 2\varphi) \quad 3.10$$

$$T = \frac{1}{2} (t_+^2 + t_-^2) \quad 3.11$$

$$\Delta T = (t_+^2 - t_-^2), \quad 3.12$$

where I_0 represents the intensity constant and J_0 , J_1 and J_2 are the Bessel functions which are proportional to the intensity of light used to determine the maximum sensitivity of the magneto-optics measurement. The terms t_+ and t_- are the Fresnel coefficients for RCP and LCP transmitted light respectively. The symbol δ_0 is the amplitude of the retardation, f the modulation frequency, φ the analyser angle and $\Delta\theta$ the difference between RCP and LCP.

The Faraday rotation θ_F and Faraday ellipticity η_F (MCD) can be deduced by measuring the intensities I_0 , I_{1f} and I_{2f} as in the Sato's formulae:

$$\theta_F = -\frac{1}{2} \Delta\theta \quad 3.13$$

$$\eta_F = \frac{1}{4} \left(\frac{\Delta T}{T} \right) \quad 3.14$$

Therefore, the values of $\Delta\theta$ and $\Delta T/T$ can be calculated from the experimental values of $I_2(f)/I_1(0)$ and $I_3(2f)/I_1(0)$, setting $\varphi = 0$, as shown in the following:

$$\frac{I_2(f)}{I_1(0)} = A \frac{J_1(\delta_0)\Delta T/T}{1+J_0(\delta_0)\sin(\Delta\theta)} \approx A J_1(\delta_0) \frac{\Delta T}{T} \approx \eta_F \quad 3.15$$

$$\frac{I_3(2f)}{I_1(0)} = B \frac{2J_2(\delta_0)\sin(\Delta\theta)}{1+J_0(\delta_0)\sin(\Delta\theta)} \approx B J_2(\delta_0)2\Delta\theta \approx \theta_F \quad 3.16$$

In order to reduce the noise levels in the magneto-optics data the measurements are repeated automatically via the controlling PC which runs Labview software. On the other hand, the data can be calibrated in order to convert them into real units (degrees). This calibration is achieved by rotating the polariser angle so as to give a minimum output of $I_3(2f)$, then we rotate the analyser over a few degrees through steps of 1°. The calibration factor is then determined by recording the resulting change in $I_3(2f)/I_0(0)$ value at each analyser angle.

3.9 Optical Transmission and Reflection Techniques

The spectra of transmission and reflection were measured directly in order to determine the absorption spectroscopy. Fig. 3.14 shows the schematic diagram for the absorption spectroscopy system. In this system the data were recorded at room temperature using a tungsten halogen lamp with a power of 250 watts to enable us to cover a wide spectral range from 1.7 eV to 4.5 eV. The set-up can be switched alter between transmission and reflection geometry via changing the position of the PMT.

The light produced from the lamp is passed through a Specro-275 spectrometer in order to produce monochromatic light. This light is then filtered and split in two beams: reference and sample beams. These two beams are passed through an optical chopper with a frequency of 370 MHZ and 310 MHZ respectively. After leaving the optical chopper, the reference beam is recorded by the PMT, whereas the

sample beam goes to the sample and is then recorded by a second PMT. This detector will then convert the light intensity to an electrical signal, and then send it to a conditioning-unit to amplify the signal and split it into the AC and DC components. The AC signals were amplified and recorded using two signal recovery, lock-in amplifiers which were used to measure the intensities I_0 , I_1 , I_2 and I_r .

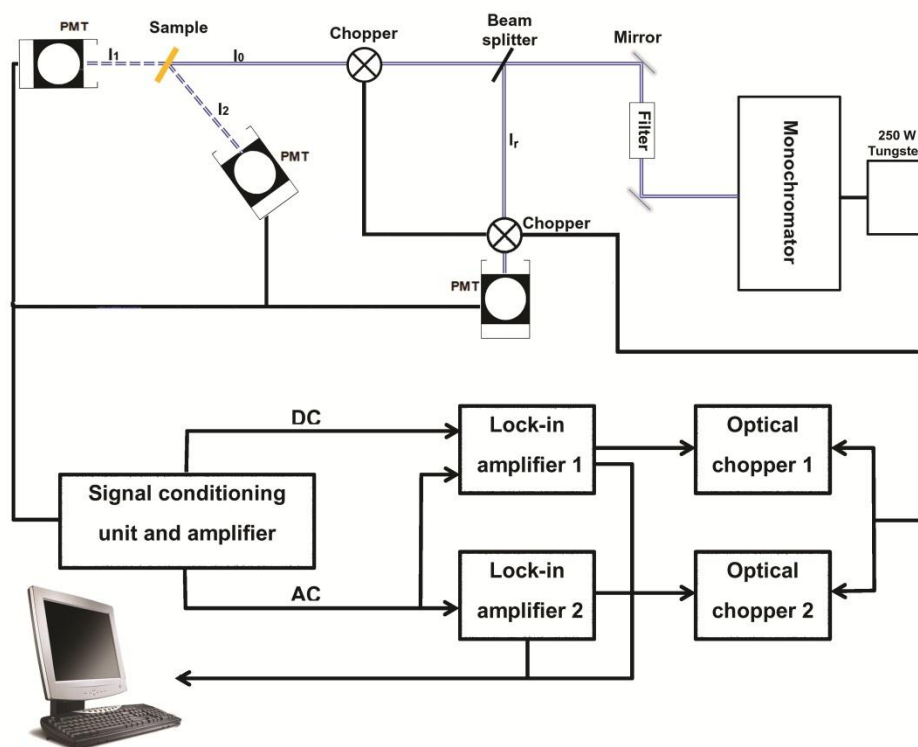


Figure (3.14): Schematic diagram of the absorption spectroscopy system.

When the light is passed through the sample of thickness l , the transmission spectra T is obtained as in the equation below [1]:

$$T = \frac{I_1}{I_0} = (1 - R)^2 e^{-al} , \quad 3.17$$

where α is the absorption coefficient which can be calculated from the following equation:

$$\alpha = \frac{1}{l} \ln \left[\frac{(1-R)^2}{T} \right] \quad 3.18$$

The band gap of the material also can be obtained from the spectra [40] as follows:

$$(\alpha h\nu)^2 \propto (h\nu - E_g), \quad 3.19$$

where, E_g is the band gap energy and $h\nu$ is the photon energy. The band gap can then be obtained by plotting α^2 as a function of $h\nu$ as shown below in fig. 3.15:

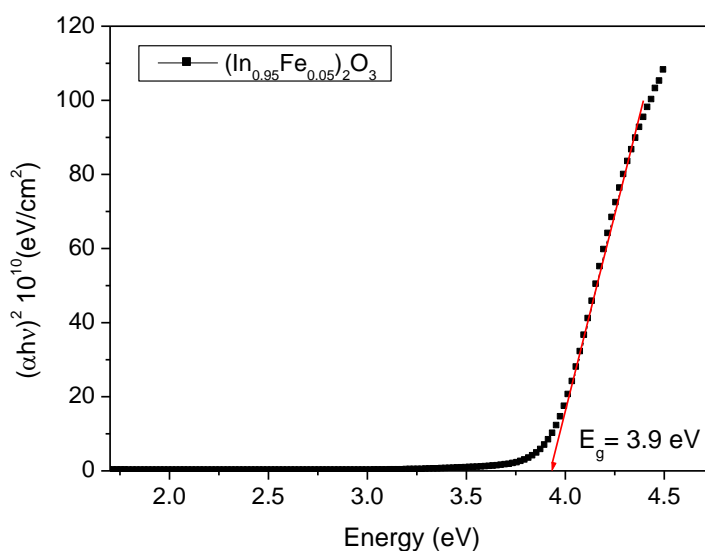


Figure 3.15: The Square of the absorption coefficient as a function of energy for $(\text{In}_{0.95}\text{Fe}_{0.05})_2\text{O}_3$ thin film, $E_g = 3.9$ eV.

3.10 Thin Films Samples Investigated

In this thesis thin films were prepared in different research groups using different growth methods. The details of the thin films that were prepared and investigated during this thesis are illustrated in the table (3.1) below:

Table (3.1): Summary of the content and growth conditions of the samples that were investigated in this thesis.

Sample name	Content	Thickness (nm)	O ₂ Pressure (mTorr)	Deposition Temperature (°C)	Annealing for 30 min (°C)	substrate	Deposition method
272Mq	$\text{La}_{0.7}\text{Sr}_{0.3}\text{MnO}_3$	81	4×10^{-3}	650	No	STO	By PLD in Sheffield University
274Mq		74	100	650	No	STO	
304Mq		130	200	650	No	STO	
306Mq		87	300	650	No	STO	
271Mq		100	4×10^{-3}	650	No	Sapphire	
273Mq		115	100	650	No	Sapphire	
301Mq		110	200	650	No	Sapphire	
303Mq		80	300	650	No	Sapphire	
260Mq	$\text{La}_{0.5}\text{Sr}_{0.5}\text{MnO}_3$	132	4×10^{-3}	650	No	STO	
262Mq		80	100	650	No	STO	
264Mq		69	200	650	No	STO	
270Mq		63	300	650	No	STO	

Sample name	Content	Thickness (nm)	O ₂ Pressure (mTorr)	Deposition Temperature (°C)	Annealing for 30 min (°C)	substrate	Deposition method
259Mq	La _{0.5} Sr _{0.5} MnO ₃	105	4×10 ⁻³	650	No	Sapphire	By PLD in Sheffield University
261Mq		75	100	650	No	Sapphire	
263Mq		50	200	650	No	Sapphire	
269Mq		105	300	650	No	Sapphire	
321Mq	La _{0.85} Sr _{0.15} MnO ₃	82	4×10 ⁻³	650	No	STO	
323Mq		59	100	650	No	STO	
324Mq		91	200	650	No	STO	
325Mq		100	300	650	No	STO	
320Mq		100	5×10 ⁻³	650	No	Sapphire	
322Mq		90	100	650	No	Sapphire	
326Mq		89	200	650	No	Sapphire	
327Mq		92	300	650	No	Sapphire	
520Mq	La _{0.7} Sr _{0.3} MnO ₃	50	300	650	No	STO	
521Mq	La _{0.7} Sr _{0.3} MnO ₃	200	300	650	No	STO	
Yam001	GdMnO ₃	100	1-2	650	No	STO	By Sputtering in Moscow
Yam002	GdMnO ₃	100	1-2	650	No	LAO	

Sample name	Content	Thickness (nm)	O ₂ Pressure (mTorr)	Deposition Temperature (°C)	Annealing for 30 min (°C)	substrate	Deposition method
006	(In _{0.99} Co _{0.01}) ₂ O ₃	200	0.562	330	No	Sapphire	By Sputtering in Cambridge University
007	(In _{0.98} Co _{0.02}) ₂ O ₃	200					
008	(In _{0.97} Co _{0.03}) ₂ O ₃	200					
009	(In _{0.96} Co _{0.04}) ₂ O ₃	200					
010	(In _{0.95} Co _{0.05}) ₂ O ₃	200					
133T53SP	(In _{0.99} Fe _{0.01}) ₂ O ₃	336	2×10 ⁻³	600	No	Sapphire	By PLD in KACST Saudi Arabia
132T52SP	(In _{0.98} Fe _{0.02}) ₂ O ₃	294					
131T51SP	(In _{0.97} Fe _{0.03}) ₂ O ₃	258					
130T50SP	(In _{0.96} Fe _{0.04}) ₂ O ₃	200					
129T49SP	(In _{0.95} Fe _{0.05}) ₂ O ₃	156					
328T49SP	(In _{0.95} Fe _{0.05}) ₂ O ₃	178	2×10 ⁻³	600	No	Sapphire	By PLD in KACST Saudi Arabia
329T49SP		170			500		
330T49SP		174			400		
331T49SP		179			300		
362T62SP	(In _{0.90} Fe _{0.05} Sn _{0.05}) ₂ O ₃	162	2×10 ⁻³	600	No	Sapphire	By PLD in KACST Saudi Arabia
435T93SP	(In _{0.85} Fe _{0.05} Sn _{0.10}) ₂ O ₃	196			No		
A	(In _{0.95} Fe _{0.05}) ₂ O ₃	319	5×10 ⁻²	600	No	Sapphire	By PLD in Xu's group China
B	(In _{0.95} Fe _{0.05}) ₂ O ₃	224	100		No		

3.11 References

1. M. Fox, *Optical properties of solids*. (Oxford University Press, Oxford ; New York, 2001).
2. N. A. Spaldin, *Magnetic materials : fundamentals and device applications*. (Cambridge University Press, Cambridge, Uk ; New York, 2003).
3. W. Prellier, L. Ph and B. Mercey, *Journal of Physics: Condensed Matter* **13** (48), R915 (2001).
4. L. M. Wang, H. H. Sung, B. T. Su, H. C. Yang and H. E. Horng, *Journal of Applied Physics* **88** (7), 4236-4240 (2000).
5. G. J. Snyder, R. Hiskes, S. DiCarolis, M. R. Beasley and T. H. Geballe, *Physical Review B* **53** (21), 14434-14444 (1996).
6. R. von Helmolt, J. Wecker, B. Holzapfel, L. Schultz and K. Samwer, *Physical Review Letters* **71** (14), 2331-2333 (1993).
7. O. Akira and T. Atsushi, *Semiconductor Science and Technology* **20** (4), S1 (2005).
8. J. Wilson and J. F. B. Hawkes, *Lasers, principles and applications*. (Prentice Hall, New York, 1987).
9. O. Svelto and D. C. Hanna, *Principles of lasers*, 3rd ed. (Plenum, New York, 1989).
10. L. I. Grossweiner, L. R. Jones, J. B. Grossweiner and B. H. G. Rogers, *The science of phototherapy : an introduction*. (Springer, Dordrecht ; Norwell, MA, 2005).
11. C. B. Hitz, J. J. Ewing and J. Hecht, *Introduction to laser technology*, 3rd ed. (IEEE Press, New York, 2001).

12. D. B. Chrisey and G. K. Hubler, *Pulsed laser deposition of thin films*. (J. Wiley, New York, 1994).
13. W. Prellier, A. M. Haghiri-Gosnet, B. Mercey, P. Lecoecur, M. Hervieu, C. Simon and B. Raveau, *Applied Physics Letters* **77** (7), 1023-1025 (2000).
14. M. Ziese, S. P. Sena and H. J. Blythe, *Journal of Magnetism and Magnetic Materials* **202** (2–3), 292-300 (1999).
15. D. A. Eastham, *Atomic physics of lasers*. (Taylor & Francis, London ; Philadelphia, 1986).
16. D. Basting and G. Marowsky, *Excimer laser technology*. (Springer/Praxis, Berlin ; New York, 2005).
17. X. Y. Chen, S. B. Xiong, Z. S. Sha and Z. G. Liu, *Applied Surface Science* **115** (3), 279-284 (1997).
18. D. J. Lichtenwalner, O. Auciello, R. Dat and A. I. Kingon, *Journal of Applied Physics* **74** (12), 7497-7505 (1993).
19. G. Koster, B. L. Kropman, G. J. H. M. Rijnders, D. H. A. Blank and H. Rogalla, *Applied Physics Letters* **73** (20), 2920-2922 (1998).
20. M. Lippmaa, N. Nakagawa, M. Kawasaki, S. Ohashi and H. Koinuma, *Applied Physics Letters* **76** (17), 2439-2441 (2000).
21. T. Ohnishi, K. Shibuya, T. Yamamoto and M. Lippmaa, *Journal of Applied Physics* **103** (10), 103703-103706 (2008).
22. A. Ohtomo and H. Y. Hwang, *Journal of Applied Physics* **102** (8), 083704-083706 (2007).
23. J. F. Lawler, J. M. D. Coey, J. G. Lunney and V. Skumryev, *Journal of Physics: Condensed Matter* **8** (49), 10737 (1996).

24. H. Nguyen Hoa, S. Joe and H. Awatef, *Journal of Physics: Condensed Matter* **17** (1), 199 (2005).
25. L. S. Dorneles, D. O'Mahony, C. B. Fitzgerald, F. McGee, M. Venkatesan, I. Stanca, J. G. Lunney and J. M. D. Coey, *Applied Surface Science* **248** (1-4), 406-410 (2005).
26. E. van de Riet, J. C. S. Kools and J. Dieleman, *Journal of Applied Physics* **73** (12), 8290-8296 (1993).
27. A. J. Behan, A. Mokhtari, H. J. Blythe, M. Ziese, A. M. Fox and G. A. Gehring, *Journal of Physics: Condensed Matter* **21** (34), 346001 (2009).
28. Z. L. Wang and A. J. Shapiro, *Surface Science* **328** (1-2), 141-158 (1995).
29. M. Ziese, H. C. Semmelhack, K. H. Han, S. P. Sena and H. J. Blythe, *Journal of Applied Physics* **91** (12), 9930-9936 (2002).
30. R. L. Fagaly, *Review of Scientific Instruments* **77** (10), 101101-101145 (2006).
31. M. P. Janawadkar, R. Baskaran, R. Saha, K. Gireesan, R. Nagendran, L. S. Vaidhyathan, J. Jayapandian and T. S. Radhakrishnan, *Current Science* **77** (6), 759-769 (1999).
32. J. Clarke, *Proceedings of the IEEE* **77** (8), 1208-1223 (1989).
33. Y. Zhuravlev and D. Rassi, *Squids and their applications*. (World Scientific Publ Co Pte Ltd, Singapore, 2000).
34. H. Prance, T. D. Clark, R. Whiteman, R. J. Prance, M. Everitt, P. Stiffell and J. F. Ralph, *Physical Review E* **64** (1), 016208 (2001).
35. Josephso.Bd, *Science* **184** (4136), 527-530 (1974).
36. A. Behan, Sheffield university, 2008.
37. S.P.Sena, Sheffield University, 1998.

38. K. Sato, Japanese Journal of Applied Physics **20** (12), 2403-2409 (1981).
39. K. W. Hipps and G. A. Crosby, The Journal of Physical Chemistry **83** (5), 555-562 (1979).
40. N. G. Patel and B. H. Lashkari, Journal of Materials Science **27** (11), 3026-3031 (1992).

Chapter 4

Lanthanum Strontium Manganite (LSMO)

4.1 Introduction

In the last decades, mixed-valence perovskite manganites have been shown to have very exciting characteristics from both a basic research and a technological viewpoint. This is due to the discovery of the phenomenon of colossal magnetoresistance (CMR) in thin manganite films. CMR is the very large change in resistance produced by the application of an external magnetic field [1].

The general chemical formula of the perovskites is $T_{1-x}D_x \text{MnO}_3$ where T is a trivalent rare earth cation (T = La, Pr, Nd.....) and D is a divalent alkaline-earth cation (D = Ca, Sr, Ba.....). Amongst a wide range of perovskite-type of manganites with different combinations of T and, D, $(\text{La}_{1-x} \text{Sr}_x) \text{MnO}_3$ (LSMO) is considered to be an ideal reference material [2-7]. The compound LaMnO_3 is found to be an antiferromagnetic insulator with a Néel temperature (T_N) of about 140 K. Below its Curie temperature (T_C) the ferromagnetic state in LSMO is found to be dependent upon oxygen stoichiometry and the doping level of Sr ions [4]. The maximum value of T_C has been found to be 380 K for the bulk crystals at a doping level of $x = 0.3$ [8]. Magneto-optics and optical properties of thin films provide useful information about the spin-dependent electronic structure which is very useful to determine the nature of the ferromagnetism. The intention is that these films could be used as magnetic devices such as magnetic field sensors [4, 9-10].

This chapter investigates the magnetic properties of LSMO thin films deposited under various growth conditions. Magneto-optical properties were investigated in order to provide information about the polarisation of mobile electrons below the T_C of the LSMO films.

4.2 Literature Review on LSMO

The ideal perovskite structure consists of six oxygen atoms arranged around each Mn atom to form an octahedron as indicated in fig 4.1.

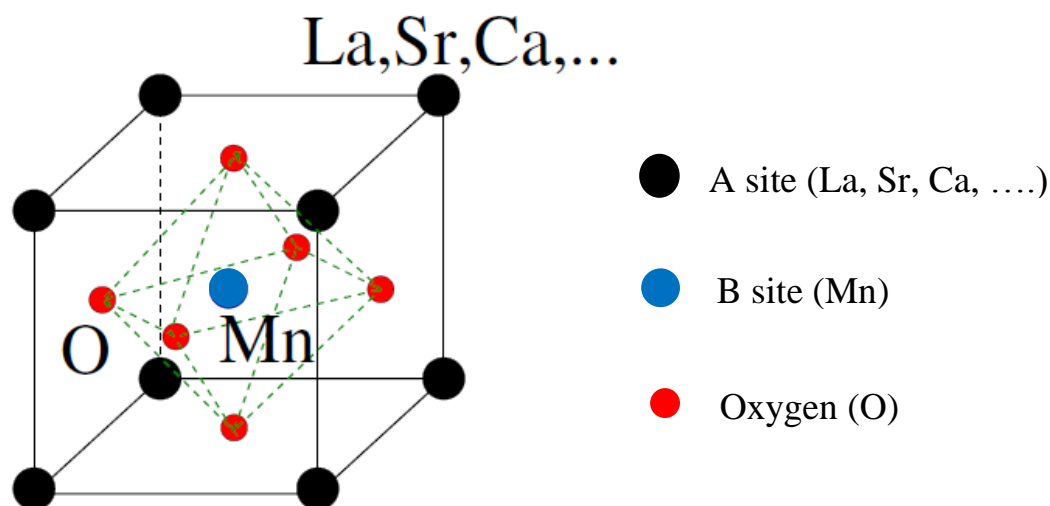


Figure (4.1): Sketch of the cubic perovskite unit-cell for manganites.

There are a large number of cations that can occupy the A and B sites in the ABO_3 cubic perovskite structure, which may be set at body-center or cube corner. The A sites of this structure are occupied by a trivalent T or divalent D ion, which leads to mixed valency of the transition metal ions Mn^{3+}/Mn^{4+} which occupy B sites [2, 11-13]. In this thesis we consider compounds where the B sites are always

occupied by Mn atoms. The mixed-valence oxides can be regarded as solid solutions between end members LaMnO_3 and SrMnO_3 with formal valence states $\text{La}^{3+}\text{Mn}^{3+}\text{O}_3^{2-}$ and $\text{Sr}^{2+}\text{Mn}^{4+}\text{O}_3^{2-}$, leading to mixed-valence compounds such as $(\text{La}_{1-x}^{3+}\text{Sr}_x^{2+})(\text{Mn}_{1-y}^{3+}\text{Mn}_y^{4+})\text{O}_3$. The electronic configurations of Mn^{3+} and Mn^{4+} are $3d^4$ and $3d^3$, respectively [14].

The crystal structure of $(\text{La}_{1-x}\text{Sr}_x)\text{MnO}_3$ was studied towards the end of the 1940s by Janker and Van Santen [12, 14]. It was found that the ferromagnetism is related to the simultaneous existence of Mn^{3+} and Mn^{4+} ions and [15-16] appears in the range of $0.1 < x < 0.5$. Both of the end members are antiferromagnetic and insulating, whereas when $x = 0.3$ the solid-solutions are both ferromagnetic and conducting. The $\text{La}_{1-x}\text{Sr}_x\text{MnO}_3$ system at $x = 0.16$ exhibits a very interesting state because it becomes ferromagnetic and exhibits a metal-insulator transition at 160 K [14, 17]. The expected magnetisation (M) from the LSMO per Mn ion can be calculated as following:

$$\begin{aligned} M &= [4 \times (1 - x) + 3 \times (x)]\mu_B \\ &= (4 - x)\mu_B, \end{aligned} \tag{1}$$

where x , is the doping level and μ_B the Bohr magneton

The main effects of the various substitutions are to vary the strain and the number of electrons in the 3d band, where the mixed valency leads to a strong ferromagnetic interaction (FM). Verwey and de Boer discovered that the mixed valence can lead to metallic conduction [2, 14]. The phase diagram of the perovskite manganites is very complex, as is shown in fig. 4.2 for $(\text{La}_{1-x}\text{Sr}_x\text{MnO}_3)$ [18]. There are now hundreds of papers focused on the phase diagrams of the manganites [18-22]

Removed by the author for copyright reasons

Figure (4.2): phase diagram of $(\text{La}_{1-x}\text{Sr}_x)\text{MnO}_3$ as a function of temperature and doping level x . PI - paramagnetic insulator; PM - paramagnetic metal; CI- spin canted insulator; FI- ferromagnetic insulator; FM- ferromagnetic metal; AFM- antiferromagnetic metal ; T_c - Curie temperature; T_N - Neel temperature [18].

Theoretically, the manganite system is usually described by the 3d orbitals of the Mn in a cubic lattice, because the other orbitals are some distance from the Fermi level. The crystal field splits the 3d orbitals into two e_g higher energy levels and three t_{2g} lower energy levels. The t_{2g} states are occupied by three electrons with parallel spin. There is only one electron in one of the two e_g states for Mn^{3+} . This electron has its spin parallel to the three electrons in the t_{2g} levels due to Hund's rule [15]. It has been found that the width of the e_g band is approximately 1eV and the separation between t_{2g} and e_g is about 1.5 eV [15, 23]. Several studies predict that the band structure of $(\text{La}_{1-x}\text{Sr}_x)\text{MnO}_3$ is very close to be half-metallic system. However, 100% spin polarization of conduction electron is still not proven [10]. Hence the half-metal has an energy gap in one spin and metal with Fermi surface for the opposite

spins. In the optimally doped manganite $(\text{La}_{0.7} \text{Sr}_{0.3}) \text{MnO}_3$ the up-spins are localized and the down-spins are delocalized or *vice versa*. As far as conduction is concerned, only one spin contributes to the conduction. In the particular example shown in fig. 4.3 spin-up electrons can travel through the system, and the LSMO behaves as a half-metal. In this case the magnetic moment should be $3.7 \mu_B$. However the measurement values did not exceed $3.6 \mu_B$ and there is evidence from band calculations for some minority spin electrons at the bottom of the spin-down band due to occupation of the Mn t_{2g} spin states. Hence the spin-up Mn(e_g) are the mobile electrons and the spin-down Mn(t_{2g}) are immobile electrons, as shown in the schematic band structure fig. 4.3 [24-25].

**Removed by the
author for copyright reasons**

Figure (4.3): Schematic representation of the electronic band structure of half-metallic $(\text{La}_{0.7} \text{Sr}_{0.3}) \text{MnO}_3$ [24].

Double exchange (DE) is the first theory that explains the mechanism of both ferromagnetism and antiferromagnetism. It can be considered as a system of two Mn cations separated by an O^- anion. The DE mechanism describes the localized t_{2g} electrons as classical spins of value $s = \frac{3}{2}$ and coupled to the mobile e_g electrons according to Hund's rules. The requirement to optimise the kinetic energy of the mobile electrons favours a spin polarised ground state [2, 11, 26-27]. In the case of the undoped manganite material $(La_{1-x} Sr_x)MnO_3$ ($x = 0$) only $Mn^{3+}(3d^4)$ ions are present. The Jahn-Teller effect splits the e_g band making $LaMnO_3$ an antiferromagnetic insulator. Doping with a small amount of Sr^{2+} ions lead to an increase in the Mn^{4+} , introduced holes into the e_g band, because the La^{3+} ion is replaced by the Sr^{2+} ion. Therefore, Mn^{4+} exchanges the extra electron with Mn^{3+} and this exchange occurs via $2p$ orbitals of the O^{2-} ions. According to Hund's coupling, this only will become possible if the spins of e_g electrons are parallel to the core spin of the t_{2g} electrons. The DE mechanism occurs by transfer of a p electron from the O^{2-} ion to the Mn^{4+} ion. This is accompanied by transfer of an e_g electron from the Mn^{3+} to the O ion, replacing the previous one, as indicated in fig. 4.4.

Hund's rule requires that, for the lowest energy, the electron in the d shell should always be spin-aligned, because of the large Hund's rule coupling. However, the strain influences spin-ordering and orbital-ordering in manganite via an elongation or compression of the oxygen octahedron (MnO_6). This leads to a Jahn-Teller distortion which splits the degeneracies of the e_g and t_{2g} levels [28].

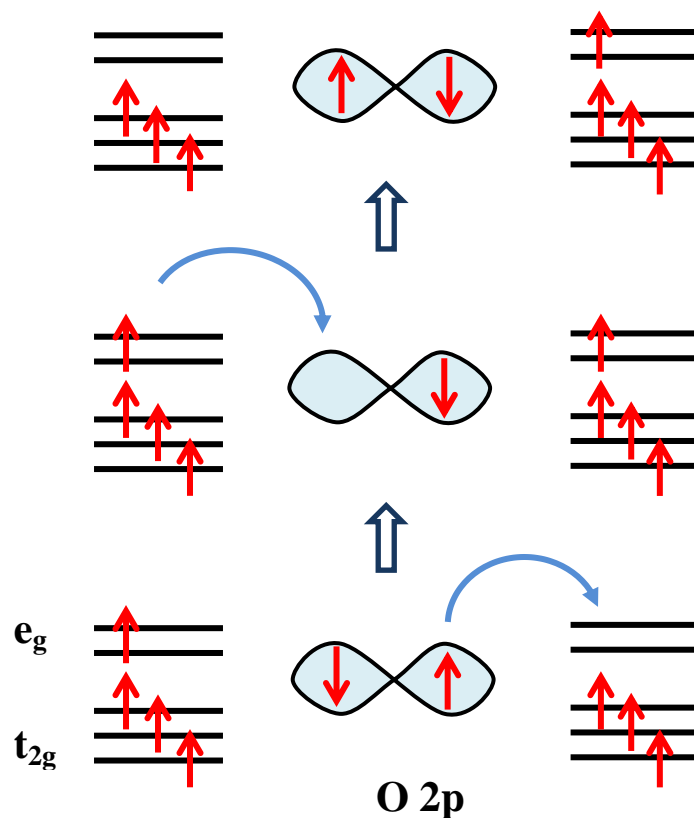


Figure (4.4): DE process with one electron hopping from the intermediate O^{2-} ion to the right Mn^{4+} ion and simultaneously one electron hopping from the left Mn^{3+} ion to the O^{2-} ion.

Moreover, strain plays a crucial role in modifying the Mn-O-Mn bond angle (ϕ) in manganite see fig. 4.5. This angle influences the strength of DE and also the magnetism and the electron-hopping between Mn atoms. The decrease of the 180° Mn-O-Mn bond angle (ϕ) leads to a reduction of the overlap between the 2p electron of O and 3d electron of Mn, this varies as $\cos^2\phi$. As a result, this weakens the ferromagnetic exchange interaction and electric conductivity [29]. The probability for hopping of the e_g electron from Mn^{3+} to Mn^{4+} is also proportional to $t_0 \cos(\theta/2)$, where θ is the angle between Mn spins as shown in fig. 4.6 [30].

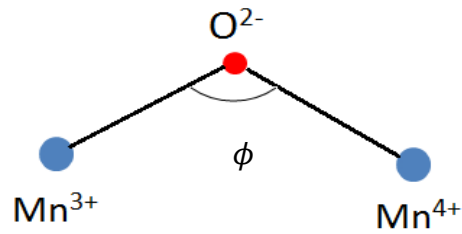


Figure (4.5): schematic diagram shows the Mn-O- Mn bond angle in LSMO.

**Removed by the
author for copyright reasons**

Figure (4.6): Schematic diagram of the influence of relative spin directions on the DE mechanism [30].

Among the various $(\text{La}_{1-x}\text{Sr}_x)\text{MnO}_3$ compositions many of research groups have focused on thin films of composition $(\text{La}_{0.7}\text{Sr}_{0.3})\text{MnO}_3$, which exhibit high T_C . The T_C and metal-insulator transition T_{MI} are required to be above room temperature in spintronics application. However, T_{MI} is found to be very close to T_C for bulk single crystals and epitaxial films, whereas T_{MI} is much lower in polycrystalline LSMO. This difference is related to the structural defects which depend on the growth conditions [6, 31-33]. The highest T_C is found to be about 380 K for the bulk crystals of $(\text{La}_{0.7}\text{Sr}_{0.3})\text{MnO}_3$ whereas T_C is reduced in the case of thin films of this composition [8].

Magnetic properties and T_C are found to be very sensitive to the particular growth conditions such as: method of fabrication, substrate material, growth temperature, annealing temperature and film thickness [31, 34]. Many studies reported that the observed differences in magnetic properties are related to strain which, in turn, depends on the lattice mismatch between the film and the substrate [8, 35-37]. The effects of strain on the physical properties of the manganites are, at the present time, not fully understood. However, the strain is not only the factor that affects the film's properties.

Epitaxial LSMO films have been grown using PLD on different substrates with different orientations [31, 38-41]. It has been found that substrates play an important role for the magnetic and transport properties of the films [42]. The most common substrates that have been used to grow epitaxial LSMO films are strontium titanate, SrTiO_3 (STO), and lanthanum aluminate, LaAlO_3 (LAO), [43]. The c-axis lattice constant of the LSMO film is about 0.389 nm and the lattice constants for STO and LAO substrates are about 0.391 nm and 0.379 nm, respectively [35]. The LSMO films grown on STO substrates exhibit an in-plane easy magnetisation direction

whereas the films exhibit an out-of plan easy direction, on LAO substrates [35]. In addition, a LSMO thin film has been grown on a sapphire substrate using the PLD technique. However, the sapphire substrate and LSMO are completely different in symmetries and lattice spacings [43].

H.Y.Hwang *et al* have reported that the resistivity $\rho(T)$ for single crystal and polycrystalline $(La_{2/3} Sr_{1/3})MnO_3$ show a sharp drop at $T_C = 365$ K. Despite the temperature dependence of the magnetization, T_C measured in 0.5 T is very similar in single-crystal and poly-crystalline as indicated in fig. 4.7 [44].

**Removed by the
author for copyright reasons**

Figure (4.7) Top panel: $\rho(T)$ of $(La_{2/3} Sr_{1/3})MnO_3$ for a single-crystal sample and two polycrystalline samples with final sintering temperatures of 1300 °C and 1700 °C. Bottom panel: the temperature dependence magnetisation for three samples at 0.5 T. Inset: The field dependent magnetisation of these samples at 5 and 280 K [44].

It is clear that the resistivity (ρ) depends on the sample quality, whereas the magnetisation is far less dependent. Hence the magnetisation is dominated by grain volumes whereas the resistivity is dominated by the intermediate area between the grains which act as an insulating and spin-scattering zone when the electrons hop from one magnetic domain to another [31, 45].

Thin films of $(\text{La}_{2/3}\text{Sr}_{1/3})\text{MnO}_3$ grown on STO substrates showing superior magnetic and electrical properties have been reported [9] where the magnetisation (M_s), and T_C were 170 emu/cm^3 and 360 K , respectively. The metal-insulator transition temperature, T_{MI} was 360K , coinciding with T_C .

A.K.Pradhan *et al* reported that for $(\text{La}_{0.6}\text{Sr}_{0.4})\text{MnO}_3$ deposited on STO the T_C was close to that for bulk material. However, T_C decreases sharply with decreasing film thickness below a critical thickness of about 55 nm [13] as illustrated in fig. 4.8. This unusually large thickness dependence could be attributed to the strain or to a dead layer.

**Removed by the
author for copyright reasons**

Figure (4.8): The temperature dependence of magnetization of LSMO/STO films of varying thickness. The inset shows the enlarged graphs for 22 nm and 12 nm thick films [13].

The effect of annealing in a chosen gas such as O₂ or N₂ can lead to a change of the physical properties such as the metal-insulator transition temperature T_{MI}, the T_c and the CMR effect. (La_{1-x}Sr_x)MnO₃ thin films which have been annealed in O₂ have a higher T_c and magnetization than do as-grown films [5, 46-48].

The first optical studies of mixed-valence manganites were to estimate the potential of these materials for magneto-optical reordering. The magneto-optical measurements provide very important information about electron transitions and the spin structure of manganites such as (La_{1-x}Sr_x)MnO₃ [10, 49]. This may correlate to the d → d transition and O(2p) → 3d(Mn) charge transfer, respectively. The magneto-optical Faraday and Kerr effects have been studied as a function of wavelength [14, 23].

Magneto-optical effects for (La_{1-x}Sr_x)MnO₃ thin films with 0 < x ≤ 0.3 were reported in the photon energy range 0.9 eV to 5.3 eV at room temperature. Charge transfer excitations at 1.2 eV and 3.5 eV corresponding to the transitions, t_{2g}³ e_g¹ → t_{2g}³ e_g² and t_{2g}³ e_g¹ → t_{2g}⁴ e_g¹ respectively have been observed [10, 50].

Magnetic Circular Dichroism (MCD), which is the difference in absorption between right and left circularly polarization light, is a very efficient tool for investigating the electronic structure. MCD provides information about the polarisation of the mobile electrons [10, 51].

Pellegrin *et al.* have recorded the MCD spectra of X-ray absorption of single-crystal films of (La_{1-x}Sr_x)MnO₃ with x = 0.15, x = 0.18 and x = 0.40 at 30 K. The X-ray absorption was found to vary with the value of x [14, 52]

Gehring *et al* reported MCD spectra of (La_{0.7}Sr_{0.3})MnO₃ thin films of thickness 500 Å in magnetic fields up to 0.5 T and temperature ranging from 10 K to

450 K. It was found that the spectra peak at about 3 eV and the peak position moved toward lower energy when the temperature is increased, as indicated in fig. 4.9 [10].

**Removed by the
author for copyright reasons**

Figure (4.9): MCD measurements of 500 Å epitaxial LSMO films grown on (001) $\text{La}_{0.3}\text{Sr}_{0.7}\text{Al}_{0.65}\text{Ta}_{0.35}\text{O}_9$ (LSAT) substrates at T= 10, 55, 100, 150, 200, 250, 300, 350 and 400 K with a magnet field of 0.5 T applied along the [001] direction of the film [10] .

4.3 Experiment Results and Discussion

In order to investigate the magnetic and magneto-optical properties of LSMO, two groups of $(\text{La}_{1-x}\text{Sr}_x)\text{MnO}_3$ films with $x = 0.15, 0.3$ and 0.5 were deposited onto STO (001) and sapphire (0001) substrates. The LSMO target was prepared from high purity La_2O_3 , SrCO_3 and MnO_2 powders. The stoichiometric mixture were heated and re-ground in air at 800, 1000 and 1200 °C for 16 hours. The result is LSMO calcined powder that was then pressed at 25,000 Pa and sintered at 1400 °C for 12 hours in order to give a high density target. The film growth was carried out by PLD. The films were grown at a deposition temperature of 650 °C in an oxygen

partial pressure ranging from 4×10^{-3} mTorr to 300 mTorr. Fig. 4.10 shows the XRD patterns of the LSMO film grown on an STO substrate at base pressure (4×10^{-3} mTorr) and at 300 mTorr. These data were measured by Ali Hakimi in the laboratory of Cambridge University. XRD patterns indicate a number of secondary phases in the film grown at base pressure. The film grown in a higher oxygen pressure (300 mTorr) is single-phase (red line), is oriented with the STO substrate and we see reflection peaks which correspond to LSMO (002), (004), (006). Many STO substrate peaks are present; these peaks are obviously very sharp.

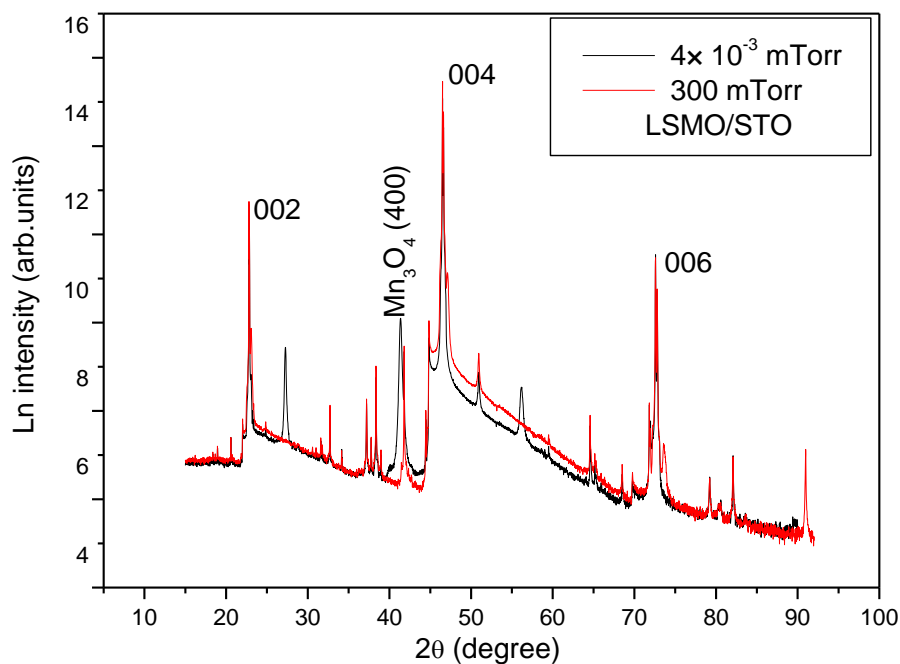


Figure (4.10): The XRD pattern of $(\text{La}_{0.7}\text{Sr}_{0.3})\text{MnO}_3$ films grown on STO at base pressure and 300 mTorr. The X-ray wavelength was 1.5406 \AA .

4.3.1 The Dependence of Magnetic Properties on Oxygen Pressure and Type of Substrate

The effect of oxygen pressure on the magnetic properties was investigated for the $(\text{La}_{1-x}\text{Sr}_x)\text{MnO}_3$ films grown on STO and sapphire substrates at different oxygen pressure ranging from 100 mTorr to 300 mTorr. The magnetic properties of the films were investigated using the SQUID. The measurement was achieved in the temperature range 5-400 K with in-plane magnetic fields up to 1 Tesla. Fig. 4.11 shows the variation of the magnetisation in LSMO films at 300 K as a function of doping level and oxygen pressure for films grown on STO and sapphire substrates. In general, the magnetisation increased with increase of oxygen pressure. It is believed that the ferromagnetism in the LSMO is due to the DE interaction between Mn^{3+} and Mn^{4+} ions. The chemical formula of this material (LSMO) can be written as $\text{La}_{1-x}^{3+}\text{Sr}_x^{2+}\text{Mn}_{1-y}^{3+}\text{Mn}_y^{4+}\text{O}_{3-\delta}^{2-}$, and consequently $y = x - 2\delta$ where δ is the oxygen content deviation. Therefore, any change of oxygen content is expected to change y , which determines the ratio of Mn^{4+} to Mn^{3+} ions which, in turn, changes the magnetic properties of the LSMO films as if a shift of Sr doping level (x) will do see fig. 4.2. Therefore, the ratio $\text{Mn}^{4+}/\text{Mn}^{3+}$ can be controlled by oxygen content and an increase of oxygen pressure will cause the $\text{Mn}^{4+}/\text{Mn}^{3+}$ ratio to be increased and will thus enhance the magnetic properties of LSMO films.

The films grown at 300 mTorr and 30% Sr on both STO and sapphire substrates exhibited higher magnetisations. However, the magnetisation is higher for the film grown on the STO substrate. This indicate that, at $x = 0.3$, the films have more Mn^{4+} ions, which increases the DE interaction ($\text{Mn}^{4+} - \text{O} - \text{Mn}^{3+}$) whereas at other values of x the films have more pairs of ions ($\text{Mn}^{4+} - \text{O} - \text{Mn}^{4+}$) or ($\text{Mn}^{3+} - \text{O} - \text{Mn}^{3+}$).

Subsequently, the LSMO films with 30% Sr doping level grown on STO and sapphire substrates were used for further studies in order to investigate their magnetic and magneto-optical properties.

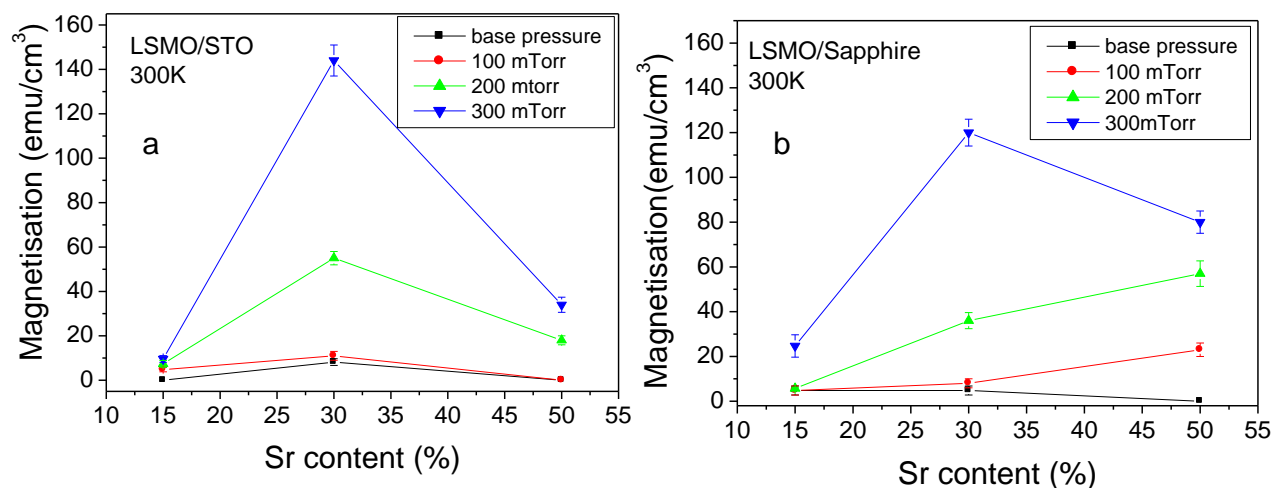


Figure (4.11): The saturation magnetisation at 300 K as a function of Sr doping level and oxygen growth pressure of $(La_{1-x}Sr_x)MnO_3$ films grown on a) STO substrate b) Sapphire

Fig. 4.12 shows the T_C dependence on Sr doping level for films grown at 300 mTorr and the T_C dependence on oxygen pressure for a 30% Sr doping of LSMO films on STO and sapphire substrates. The temperature dependence of the magnetisation was measured using the ZFC mode under in-plane field of 0.1 T and the T_C was defined as the temperature corresponding to the minimum of dM/dT . The highest value of T_C was at $x = 30\%$ and increased with increasing oxygen pressure. The T_C value is 340 K for the LSMO film grown at 300 mTorr on both STO and sapphire substrates. This reveals that the magnetic properties of LSMO films are strongly affected by oxygen pressure during the growth, as well as by the doping

level. Moreover, the result displayed very good evidence that the quality of the LSMO films was improved by increasing oxygen pressure, especially for films grown on the sapphire substrates.

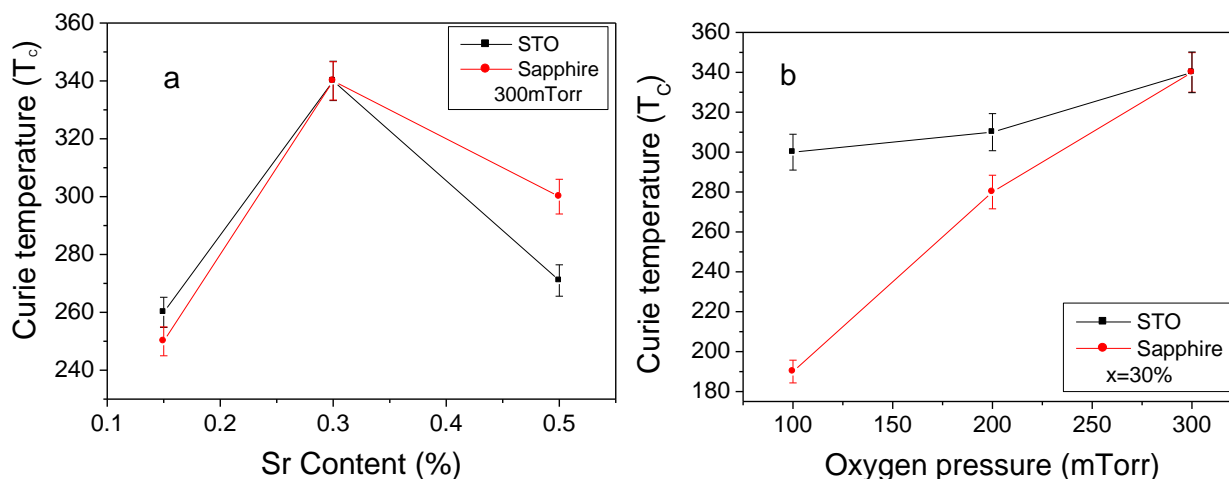


Figure (4.12): a) Variation of T_C of $(La_{1-x}Sr_x)MnO_3$ films grown on STO and sapphire substrate at 300 mTorr as a function of Sr doping level. b) Variation of T_C of $(La_{0.7}Sr_{0.3})MnO_3$ films grown on STO and sapphire substrate as a function of oxygen pressure.

Fig.4.13 shows ZFC measurement made in-plane in a field of 0.1 T with variation of oxygen pressure; the ferromagnetic order and T_C of these films are enhanced. A value of 340 K was obtained for both films grown on STO and sapphire substrates at 300 mTorr with thickness of 87 nm and 80 nm respectively. This LSMO film exhibits a high value of $T_C=340$ K compared to the previous study for the same composition, in which a film of 300 nm of LSMO grown on STO gave $T_C=358$ K and 360 K for the film of 100-200 nm thick [13, 53].

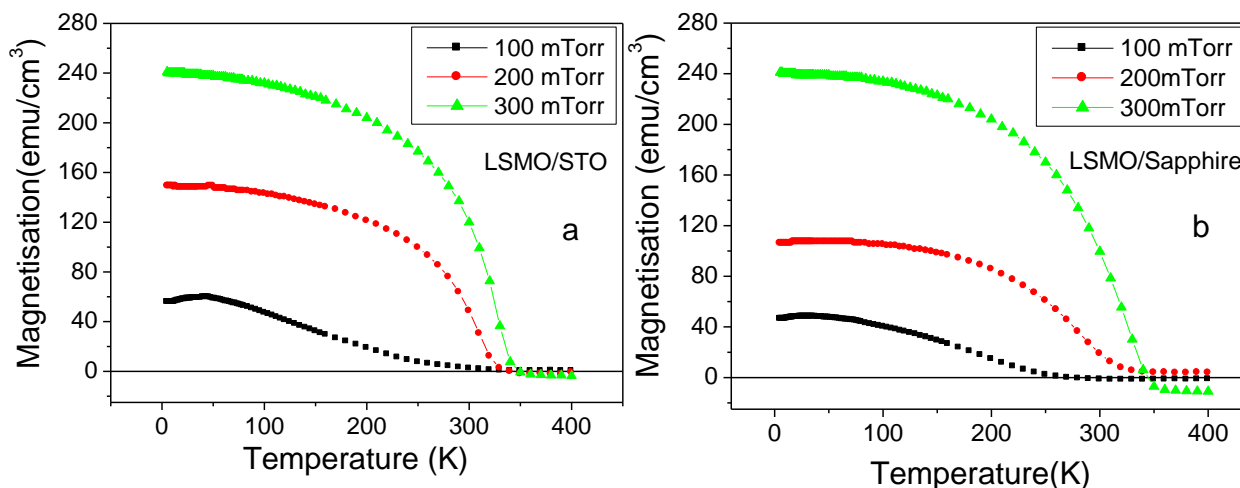


Figure (4.13): ZFC magnetisation, measured at 1000 Oe, as a function of temperature for $(\text{La}_{0.7}\text{Sr}_{0.3})\text{MnO}_3$ films grown at 100 mTorr, 200 mTorr and 300 mTorr on a) STO and b) sapphire substrates.

Figure (4.14) shows the hysteresis loop of LSMO films grown on STO substrate and measured under an applied magnetic field up to 1 T in the plane of the films. The films show hysteresis loops at 5 K and 300 K, which is strong evidence for ferromagnetism in LSMO films above room temperature. The coercive fields of these films are 450, 84 and 34 Oe at 5 K, while the coercive fields at 300 K are 133, 98 and 16 Oe for the films grown at 100, 200 and 300 mTorr, respectively. The coercivity depends on defects such as grain boundaries, point defects and surface roughness [9, 54-55]. The coercive field for these LSMO films decreases sharply with increasing oxygen pressure due to the improvement in crystalline quality. This verifies that the film grown at higher oxygen pressure has a low level of defects and is of a high quality.

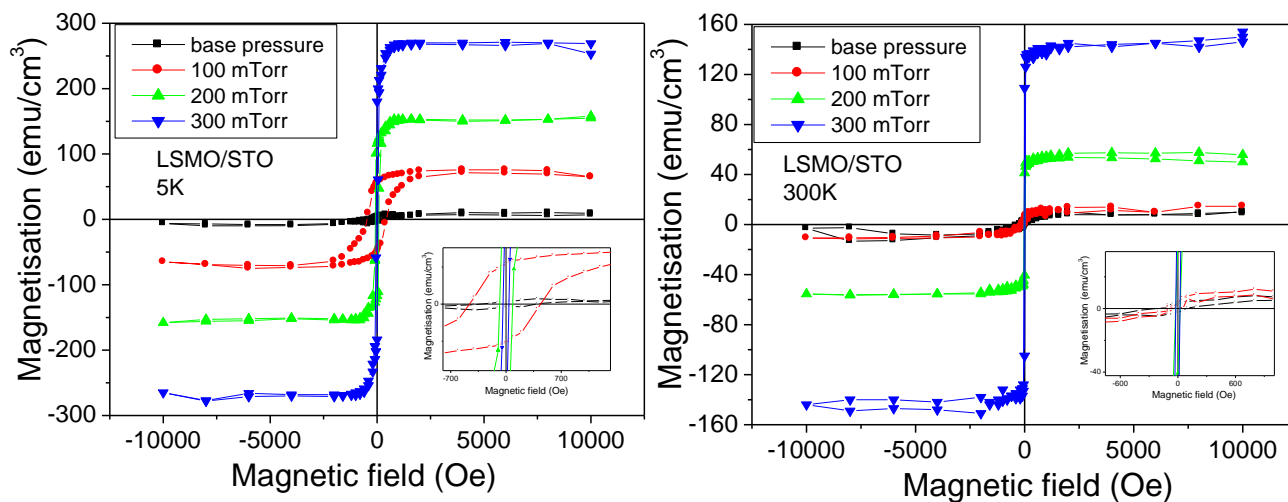


Figure (4.14): Hysteresis loops measured at 5 K and 300 K for $(\text{La}_{0.7}\text{Sr}_{0.3})\text{MnO}_3$ films grown by PLD on STO substrates at oxygen pressures of 4×10^{-3} , 100, 200 and 300 mTorr with thicknesses of 81, 74, 130 and 87 nm, respectively (the diamagnetic contributions from the substrates have been subtracted). The insets show the blow-up of the region around the origin.

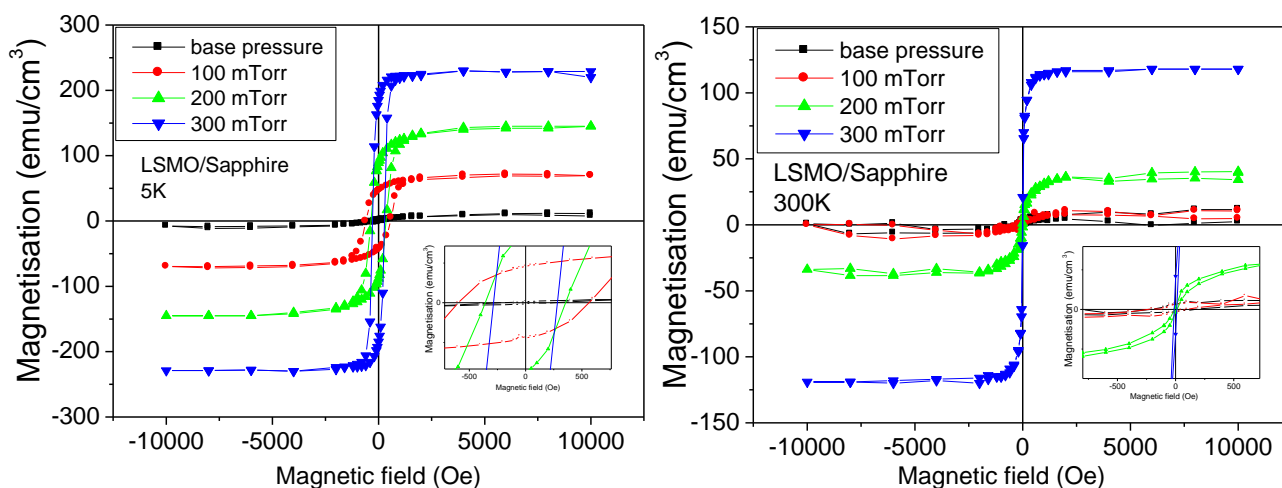


Figure (4.15): Hysteresis loops measured at 5 K and 300 K for $(\text{La}_{0.7}\text{Sr}_{0.3})\text{MnO}_3$ films grown by PLD on sapphire substrates at oxygen pressures of 4×10^{-3} , 100, 200 and 300 mTorr with film thicknesses of 100, 115, 110 and 80 nm, respectively (the diamagnetic contributions from the substrates have been subtracted). The insets show the blow-up of the region around the origin.

The hysteresis loops corresponding to the LSMO films grown on sapphire substrates (Fig. 4.15) show that the magnetisation behaviour is similar to the LSMO films grown on STO. The magnetisation increases with increase of oxygen pressure, whereas the coercive fields of these films decrease with increase of oxygen pressure.

4.3.2 Dependence of Magnetic Properties on Film Thickness

In order to investigate the influence of film thickness on the physical properties of LSMO thin films, three thin films of $(\text{La}_{0.7}\text{Sr}_{0.3})\text{MnO}_3$ with thicknesses of 50, 87 and 200 nm were grown on STO (001) substrates by PLD. The films were deposited under 300 mTorr of oxygen and the substrate temperature was maintained at 650 K. Fig. 4.16 shows temperature dependence of ZFC measurements with an in-plane field of 0.1 T. The LSMO films with thickness 50, 87 and 200 nm exhibit T_C at 320 ± 16 , 340 ± 10 and 350 ± 12 K respectively. The variation of T_C with film thickness may be related to a strain induced lattice mismatch between films and substrates. It has already been reported that the strain relaxation of lattice mismatch between the film and the substrate at the interfaces occurs as the film thickness increases [13]. These data show a magnetisation of about 140 emu/cm^3 for the film with thickness 50 nm as compared with the previous study [13] fig. 4.5, which had a magnetisation at about 180 emu/cm^3 for the film with thickness 55 nm.

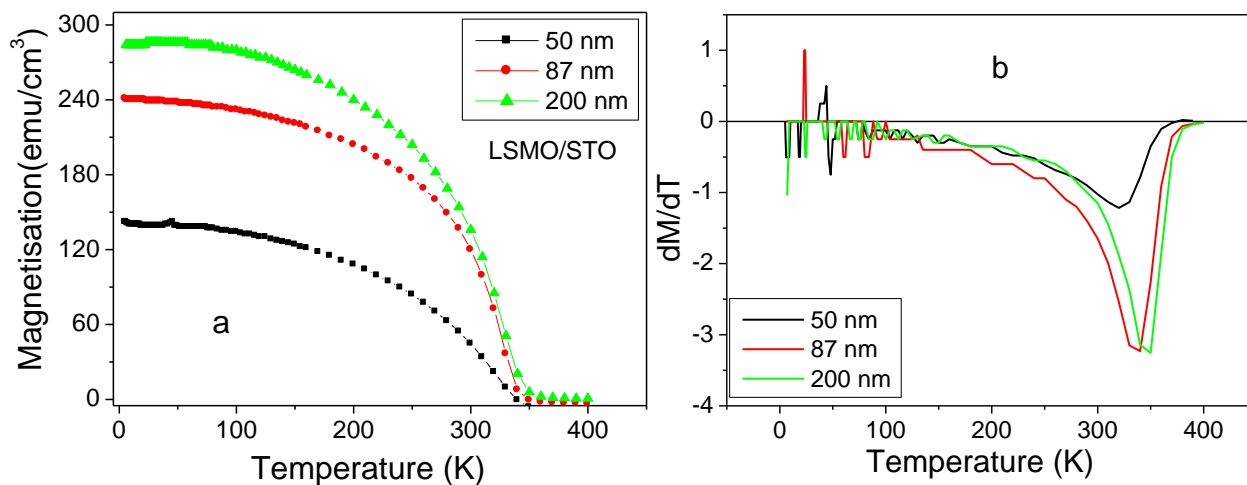


Figure (4.16): a) ZFC magnetisation, taken at 1000 Oe, as a function of temperature for $(\text{La}_{0.7}\text{Sr}_{0.3})\text{MnO}_3$ films grown at 300 mTorr on STO substrates. b) Temperature dependence of the derivative dM/dT

Hysteresis loops of $(\text{La}_{0.7}\text{Sr}_{0.3})\text{MnO}_3$ (LSMO) films with thicknesses of 50, 87 and 200 nm have been measured under an applied magnetic field up to 1 T in the plane of the films. The effect of the surface and the interface on the magnetic properties of LSMO films was estimated using the formula $Ml = M_s(l - d)$ [56] where l is the film thickness, M the total magnetisation, M_s is the saturation magnetisation and d is the dead layer thickness. Fig.4.17 shows the saturation magnetisation multiplied by the thickness versus the film thickness for these films. A linear relationship indicated a dead-layer below a critical thickness and the intercept of the horizontal axis provides an inactive, magnetically dead layer of about 23 nm, which is larger than the 1.2 nm reported previously [57]. This result could be a possible reason for the reduction of the magnetisation in our LSMO films.

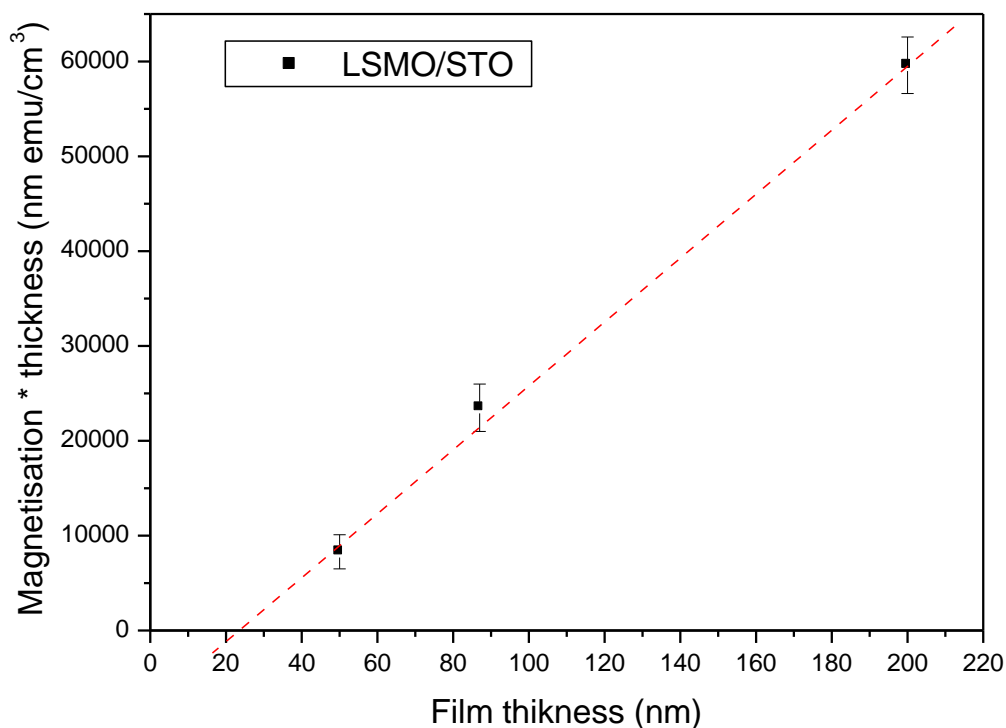


Figure (4.17): The saturation magnetisation multiplied by film thickness versus thickness for LSMO films grown on STO at 300 mTorr oxygen pressure.

The saturation magnetisation (M_s) and remnant magnetisation (M_r) values at 300 K decreased from 142 emu/cm³ and 107 emu/cm³ to 62 emu/cm³ and 8 emu/cm³ for the 87 nm film and 50 nm film, respectively. This suggests that there is a critical thickness for this material below which the ferromagnetic state is no longer maintained above room temperature. Table 4.1 shows a summary of the magnetization data taken at 5 K and 300 K.

Film thickness (nm)	$M_s(5K)$ (emu/cm ³)	$\mu_o H_C(5K)$ (Oe)	$M_r(5K)$ (emu/cm ³)	$M_s(300 K)$ (emu/cm ³)	$\mu_o H_C(300 K)$ (Oe)	$M_r(300 K)$ (emu/cm ³)
50	166 ± 7	284 ± 7	115 ± 5	62 ± 3	9 ± 0.36	8 ± 0.4
87	270 ± 9	38 ± 2	182 ± 8	142 ± 7	22 ± 1.1	107 ± 5
200	298 ± 12	140 ± 6	197 ± 9	142 ± 7	20 ± 1.2	80 ± 4

Table (4.1): summary of magnetisation data for $(La_{0.7} Sr_{0.3})MnO_3$ films measured at 5 K and 300 K. M_s denotes the saturation magnetisation, $\mu_o H_C$ the coercive field and M_r the remnant magnetisation.

4.3.3 Dependence of Magnetic Properties on Annealing

The as-grown $(La_{0.7} Sr_{0.3})MnO_3$ film, deposited on STO substrate by PLD at base pressure 4×10^{-3} mTorr, exhibit low saturation magnetisation and low T_C . This might be related to the low oxygen content of the film due to the low oxygen partial pressure during deposition. It has been found that the oxygen content of LSMO film could be influenced by the oxygen pressure during the growth [54, 58]. In order to investigate the effect of annealing on the magnetic properties of LSMO films, the as-grown films were annealed ex situ at 800 °C temperatures in air at atmospheric pressure for one hour. Fig. 4.18 shows ZFC measurement, under in-plane field of 0.1 T for as-grown and annealed LSMO films.

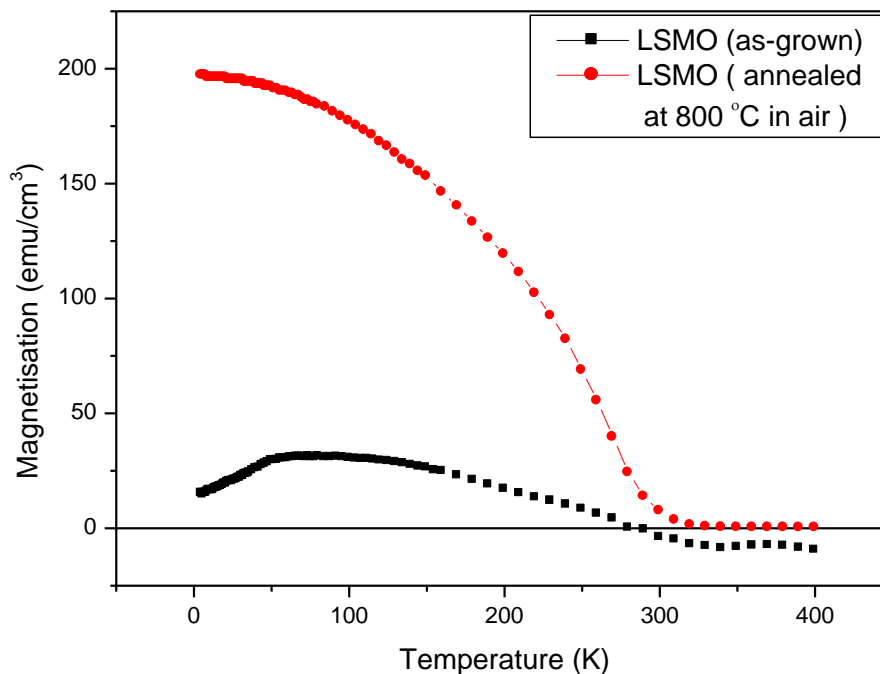


Figure (4.18): ZFC magnetisation, measured at 1000 Oe, as a function of temperature of as-grown and annealed ($\text{La}_{0.7}\text{Sr}_{0.3}\text{MnO}_3$) film. The film thickness was 81 nm grown by PLD on STO substrate.

The magnetisation and T_C were enhanced by annealing the as-grown LSMO film. This is because the LSMO film absorbed oxygen from the air during the annealing procedures and thus the ratio of $\text{Mn}^{4+}/\text{Mn}^{3+}$ is increased in the film so that the ferromagnetic order is enhanced. However, the magnetisation and T_C values for the film grown at low oxygen pressure then annealed in air are below the values of the film grown at higher oxygen pressure (300 mTorr).

Typical hysteresis loops at 5 K and 300 K for the as-grown and the annealed LSMO films are plotted in fig.4.19. The coercive fields values at 5 K are 352 and

126 Oe while the coercive fields at 300 K are 160 and 25 Oe for the as-grown and annealed LSMO films, respectively. The coercivities are always lower for the annealed film than for the as-grown film. This might be related to the presence of structural defects because the as-grown LSMO film contain more oxygen vacancies, whereas the annealed LSMO film structure was improved due to the increase of the oxygen content in the film during the annealing process.

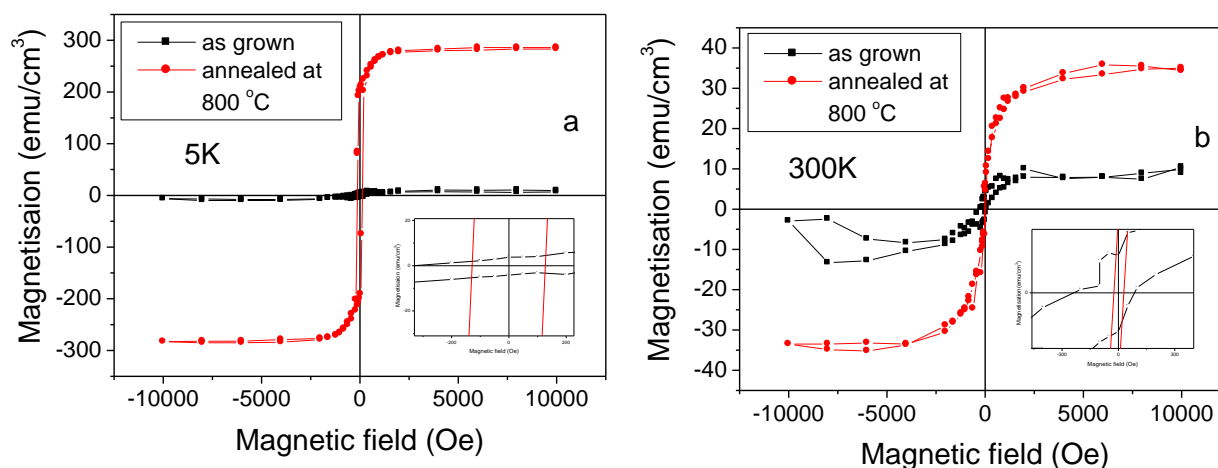


Figure (4.19): Hysteresis loops measured at 5 K and 300 K for as-grown and annealed (La_{0.7} Sr_{0.3})MnO₃ films. The film thickness was 81nm; film was grown by PLD on STO substrate (the diamagnetic contribution from the substrate has been subtracted). The insets show the enlarged region around the origin.

4.3.4 Magneto- Optical Properties of LSMO Thin Films

This section gives measurements of MCD on the $(La_{0.7} Sr_{0.3})MnO_3$ films in order to obtain information about the polarisation of mobile electrons. The MCD signal depends on the spin polarisation and electron transition strength. This makes the MCD a very sensitive tool to study the electronic transition and the nature of magnetic state in LSMO. Fig. 4.20 shows the MCD spectra of $(La_{0.7} Sr_{0.3})MnO_3$ films as a function of oxygen pressure. These LSMO films were grown on sapphire substrates at oxygen partial pressures of 4×10^{-3} , 100, 200 and 300 mTorr. The MCD was recorded at room temperature in fields of up to 1.8 T and in the energy range 1.7 eV to 4.5 eV. The plot shows two main spectral features at 1.7 eV and 3.28 eV. The spectral feature at 1.7 eV was assigned to a charge transfer excitation from 2p (O) to the majority-spin e_g (3d Mn) or $(t_{2g}^3 e_g^1 \rightarrow t_{2g}^3 e_g^2)$. The strong peak at 3.28 eV was assigned to an electron excitation 2p (O) to the minority-spin t_{2g} (3d Mn) band or $(t_{2g}^3 e_g^1 \rightarrow t_{2g}^4 e_g^1)$ [10, 50]. The height of the peaks increases with increase of oxygen growth pressure; this could be attributed to the increase of oxygen content in the film. A strong peak was found at about 3.28 eV at the highest oxygen pressure and the peak is found to be shifted to lower energy with decrease of oxygen pressure. This result could be attributed to the decrease of the Mn^{4+} fraction and bandwidth with reduced oxygen content/pressure. The strength of the peak increased with increase of the oxygen growth pressure and is related to the ferromagnetic ordering. The spectral feature at 1.7 eV is broad and is observed in the film with oxygen growth pressure above 200 mTorr.

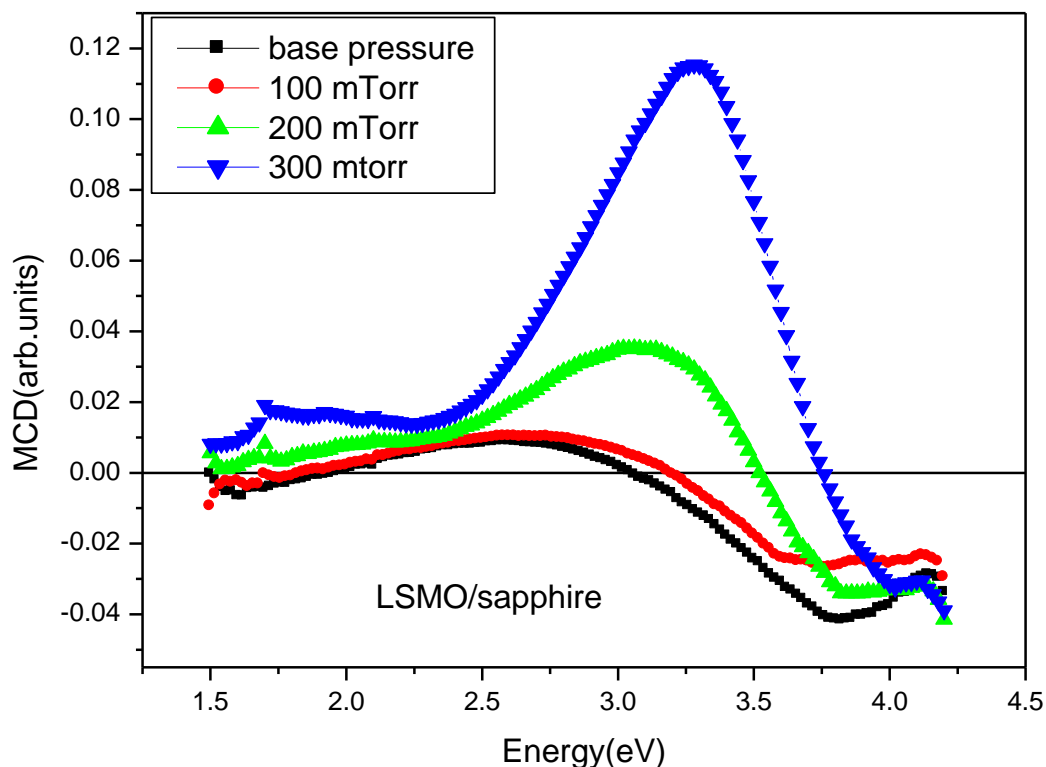


Figure (4.20): The MCD spectra at 300 K of $(\text{La}_{0.7}\text{Sr}_{0.3})\text{MnO}_3$ films as a function of oxygen growth pressure and grown on sapphire substrates.

Fig.4.21 shows similar MCD spectra for LSMO films grown on STO substrates. Once again, two significant spectral features can be distinguished from the plot: one at 1.8 eV and the other at about 3.18 eV. However, The MCD spectra of LSMO films on STO substrates showed different behaviour from the LSMO spectra on sapphire a substrate which could be due to the fact that the STO substrate undergoes a structural transition at 100 K, which gives rise to the birefringence [59]. This is because the absorption is dominated by the STO absorption edge at higher energies [60] above the band gap at 3.26 eV as shown in fig.4.22.

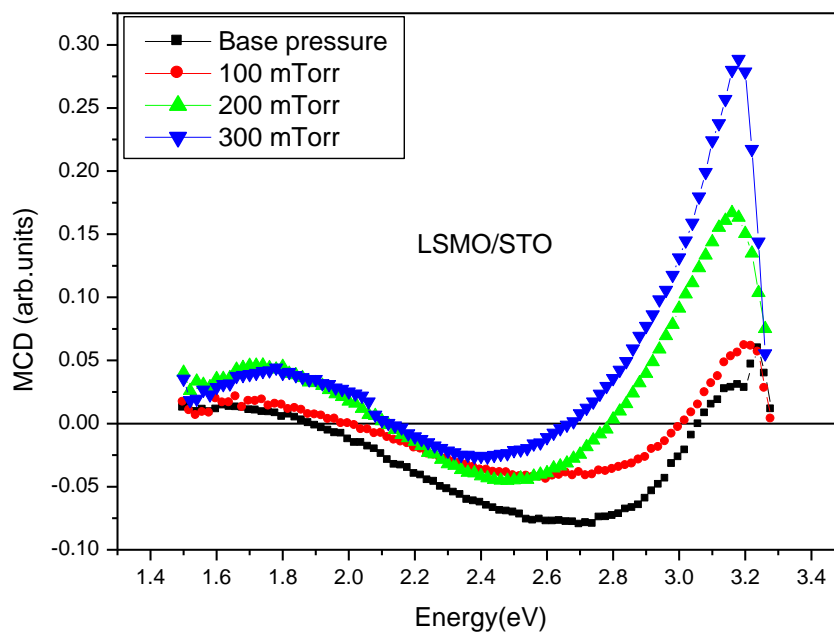


Figure (4.21): The MCD spectra at 300 K of $(\text{La}_{0.7}\text{Sr}_{0.3})\text{MnO}_3$ films as a function of oxygen growth pressure and grown on STO substrates,

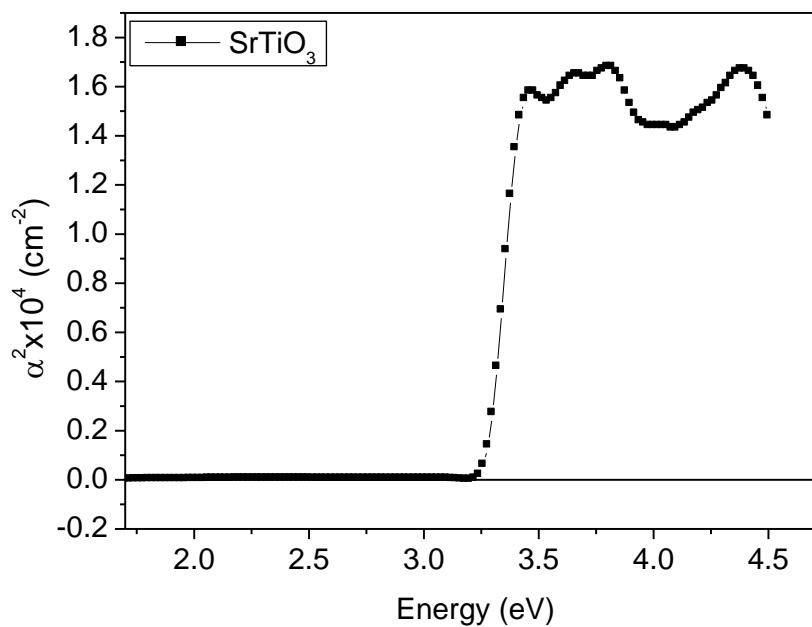


Figure (4.22): The absorption α squared as a function of energy for STO substrate, $E_g = 3.26$ eV.

The LSMO films grown at 300 mTorr oxygen pressure on both sapphire (0001) and STO (001) substrates exhibited both high magnetisation and high MCD. These films were used in order to study the temperature dependence of the MCD which may be assumed to be proportional to the polarisation of the conduction electrons of the films. The MCD were measured at different temperatures in magnetic fields up to 0.5 T and over an energy range of 1.7 eV to 4.5 eV. Fig. 4.23 shows the raw MCD spectra of LSMO films grown on (001) STO and (0001) sapphire substrates. The spectral feature was observed at about 1.8 eV and 3.22 eV for LSMO films grown on STO. For the film grown on sapphire, the spectral feature was observed at about 1.8 eV and 3.3 eV. The strong MCD peak at 3.3 eV was found to be shifted to lower energy with increase of temperature. In addition the amplitude of these peaks decreases rapidly with temperature.

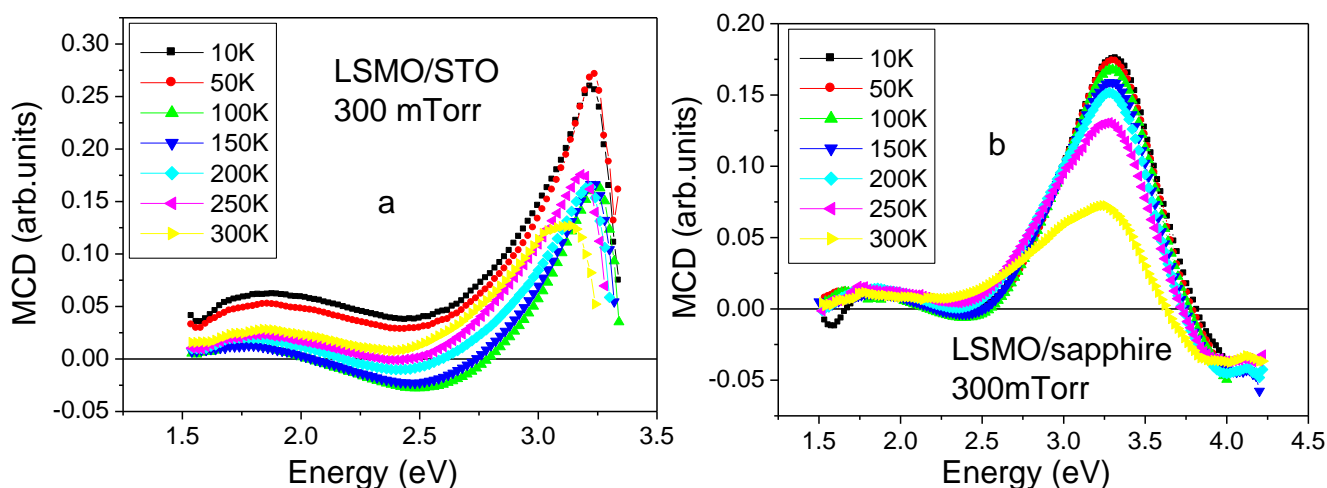


Figure (4.23): The MCD spectra as a function of temperature of $(La_{0.7}Sr_{0.3})MnO_3$ films grown at 300 mTorr on a) STO substrate and b) sapphire substrate.

This behaviour is similar to that found in a previous study of LSMO on LSAT and LAO substrate [10]. However, the MCD spectrum of LSMO films on STO substrates seems to be affected by the substrate because of the birefringence behaviour; and the magneto-optical properties of the STO substrate as will be discussed later in chapter 6.

In order to study these peaks in a more optimal way, the MCD spectrum at remanence was measured as a function of temperature, as shown in fig.4.24. The spectrum at remanence was measured in zero magnetic field after reducing the field to zero from values of $\pm 0.5 T$.

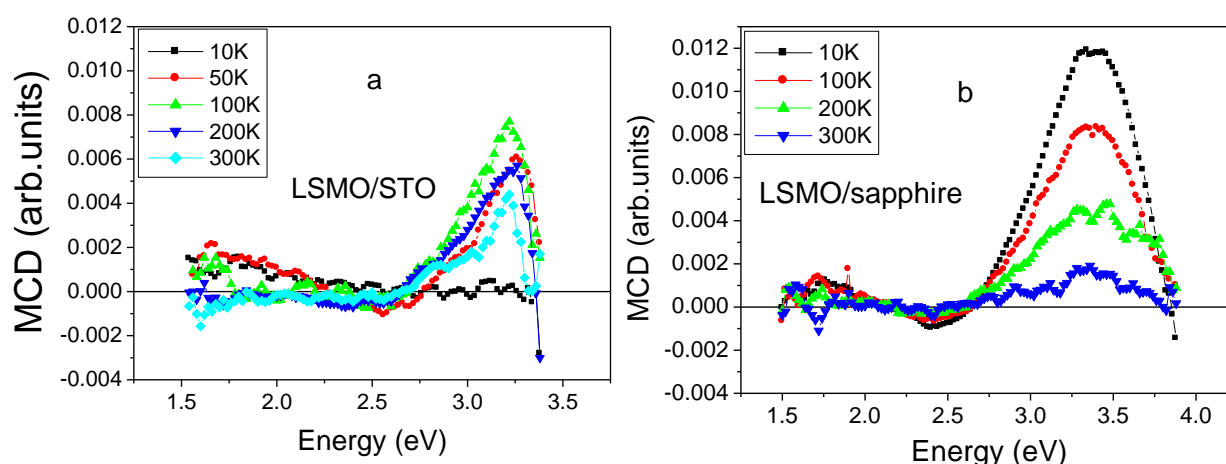


Figure (4.24): The MCD spectrum at remanence as a function of temperature for $(La_{0.7} Sr_{0.3})MnO_3$ films grown at 300 mTorr oxygen pressure on a) STO b) sapphire substrates.

The MCD spectrum at remanence is expected to have the same shape of the spectrum measured in field but with different magnitude. From Fig. 4.24 the remnant spectrum for a LSMO film on sapphire has a similar shape to the spectrum measured in-field but have different magnitudes. In addition, both the remnant spectrum and the in-field spectrum are temperature dependent and the ratio of the peak at remanence

and in-field is comparable to the ratio of M_r/M_s observed in the SQUID data at 300 K shown in fig.4.15. On the other hand, the shape of the remnant spectrum for the LSMO film grown on STO is unlike to the shape of the MCD spectrum measured in-field. Furthermore, the peak at about 3 eV has a minimum value at 10 K and a maximum value at 100 K; the peak then subsequently decreased with increasing temperature. This is extremely good evidence that this peak is affected by the contribution from the STO substrate. This could be related to the fact that STO has a cubic perovskite structure at room temperature, but undergoes a structural transition to a tetragonal phase at about 100 K which gives rise to a birefringence. Moreover, the birefringence is linearly dependent on temperature and decrease with increase of temperature, and the birefringence falls to zero at about 100 K [37, 59]. In addition, for the LSMO film grown on STO, the peak at about 3 eV is found to be shifted to lower energy, compared to the film on sapphire. In summary, the MCD spectrum of the LSMO film on STO was dominated by the birefringence and the magneto optical properties arising from the STO substrate. Consequently, the STO substrate was then studied carefully with a regard to the orientation of the substrate; this will be discussed in chapter 6.

Fig.4.25 shows a comparative study of Magnetisation temperature dependence and MCD temperature dependence for both LSMO films grown on STO and sapphire substrates. The magnetisation data obtained from the SQUID using ZFC measurements in a field of 0.1 T. The SQUID data were normalized with magnetisation at 5K and the MCD data were normalized with data at 10 K. The MCD signal follows the magnetisation for the LSMO film grown on sapphire, but shows different behaviour for LSMO film grown on STO. This result displayed very good evidence that the conduction electrons follow the magnetisation for LSMO films

grown on sapphire substrate, but for LSMO films grown on STO the MCD data was dominated by birefringence and the magneto-optical properties arising from the STO substrate. The anomaly in the MCD data at 100 K compared with SQUID data in fig.4.24a is due to the birefringence arising from the structural transition of the STO substrate.

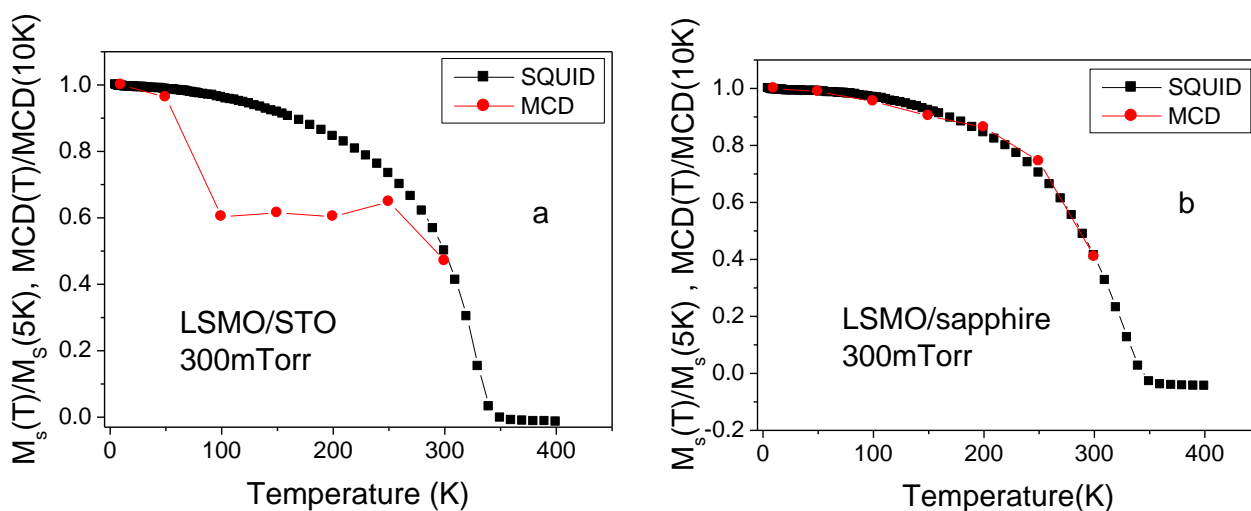


Figure (4.25): Temperature dependence of $M(T)/M(5K)$ and $MCD(T)/MCD(10K)$ of $(La_{0.7} Sr_{0.3})MnO_3$ films grown at 300 mTorr on a) STO and b) sapphire substrates.

4.4 Summary and Conclusions

This chapter reported results of the investigation of the magnetic and magneto-optical properties of $(\text{La}_{1-x}\text{Sr}_x)\text{MnO}_3$ thin films deposited under different growth conditions. LSMO thin films were deposited successfully by PLD on (001) STO and (0001) sapphire substrates. The films were prepared with various concentrations ($x=0.15, 0.30$ and 0.50) and various oxygen pressures. The LSMO films grown on STO and sapphire substrate show a pronounced hysteresis loops at 300 and 5 K, which verify that LSMO maintains strong ferromagnetic properties at room temperature and this is consistent with previous studies. The films grown with 30% of Sr on both STO and sapphire substrates exhibited higher magnetisation and the magnetisation increased with increase of oxygen pressure.

The MCD spectral feature was observed at about 1.7 eV and 3.28 eV for $(\text{La}_{0.7}\text{Sr}_{0.3})\text{MnO}_3$ films grown at different oxygen pressures on sapphire substrates. The strong MCD peak at 3.28 eV was found to be shifted to lower energy with decreasing oxygen pressure; this could be attributed to the decrease of the Mn^{4+} fraction and band width with reduced oxygen. The temperature dependence of the MCD spectra displayed peaks at 1.8 eV and 3.3 eV for $(\text{La}_{0.7}\text{Sr}_{0.3})\text{MnO}_3$ films grown at 300 mTorr oxygen pressure on sapphire substrates. The strong MCD peak at 3.3 eV was found to be shifted to lower energy with increase of temperature and the strength of these peaks weakens rapidly with temperature. The MCD spectra of LSMO films on STO substrates seems to be dominated by the magneto-optical properties and birefringence behaviour arising from the STO substrate. The MCD signal follows the magnetisation for the LSMO film grown on sapphire, but shows a different behaviour for LSMO film grown on STO.

Overall, STO substrate was chosen because it suitable for the growth of high quality epitaxial thin films. However, this did have some disadvantages for an optical study. The band gap energy at 3.2 eV was unfortunate; it reduced the useful energy range over which absorption of the films could be measured. However, another disadvantage was the structural transition at ~100 K, which gives rise to a birefringence, unless the E vector of the light is along an optic axis. The magneto-optical data of LSMO on sapphire substrates are significantly better than LSMO grown on STO substrates. This makes sapphire an optimal substrate for the growth of LSMO.

4.5 References

1. N. A. Spaldin, *Magnetic materials : fundamentals and device applications*. (Cambridge University Press, Cambridge, Uk ; New York, 2003).
2. M. El-Hagary, Y. A. Shoker, S. Mohammad, A. M. Moustafa, A. A. El-Aal, H. Michor, M. Reissner, G. Hilscher and A. A. Ramadan, *Journal of Alloys and Compounds* **468** (1–2), 47-53 (2009).
3. K. X. Jin, S. G. Zhao, X. Y. Tan and C. L. Chen, *Journal of Physics D: Applied Physics* **41** (4), 045105 (2008).
4. H. L. Liu, K. S. Lu, M. X. Kuo, L. Uba, S. Uba, L. M. Wang and H. T. Jeng, *Journal of Applied Physics* **99** (4), 043908-043907 (2006).
5. W. Prellier, L. Ph and B. Mercey, *Journal of Physics: Condensed Matter* **13** (48), R915 (2001).
6. A. P. Ramirez, *Journal of Physics: Condensed Matter* **9** (39), 8171 (1997).
7. H. Zenia, G. A. Gehring, G. Banach and W. M. Temmerman, *Phys. Rev. B* **71** (2), 024416 (2005).
8. M. Veis, S. Visnovsky, P. Lecoeur, A. M. Haghiri-Gosnet, J. P. Renard, P. Beauvillain, W. Prellier, B. Mercey, J. Mistrik and T. Yamaguchi, *Journal of Physics D-Applied Physics* **42** (19) (2009).
9. D. Liu and W. Liu, *Ceramics International* **37** (8), 3531-3534 (2011).
10. T. K. Nath, J. R. Neal and G. A. Gehring, *Journal of Applied Physics* **105** (7), 07D709-703 (2009).
11. J. B. Goodenough, *Physical Review* **100** (2), 564-573 (1955).
12. G. H. Jonker and J. H. Van Santen, *Physica* **16** (3), 337-349 (1950).

13. A. K. Pradhan, D. Hunter, T. Williams, B. Lasley-Hunter, R. Bah, H. Mustafa, R. Rakhimov, J. Zhang, D. J. Sellmyer, E. E. Carpenter, D. R. Sahu and J. L. Huang, *Journal of Applied Physics* **103** (2), 023914-023918 (2008).
14. J. M. D. Coey, M. Viret and S. von Molnár, *Advances in Physics* **48** (2), 167-293 (1999).
15. J. M. D. Coey, M. Viret, L. Ranno and K. Ounadjela, *Physical Review Letters* **75** (21), 3910-3913 (1995).
16. J. G.H, *Physica* **22** (6–12), 707-722 (1956).
17. M. M. Savosta, P. Novák and Z. Jirák, *Phys. Rev. B* **67** (10), 100411 (2003).
18. E. Dagotto, T. Hotta and A. Moreo, *Physics Reports-Review Section of Physics Letters* **344** (1-3), 1-153 (2001).
19. H. Kuwahara, Y. Tomioka, A. Asamitsu, Y. Moritomo and Y. Tokura, *Science* **270** (5238), 961-963 (1995).
20. M. B. Salamon and M. Jaime, *Reviews of Modern Physics* **73** (3), 583-628 (2001).
21. Y. Tokura and Y. Tomioka, *J. Magn. Magn. Mater.* **200** (1-3), 1-23 (1999).
22. A. Urushibara, Y. Moritomo, T. Arima, A. Asamitsu, G. Kido and Y. Tokura, *Phys. Rev. B* **51** (20), 14103-14109 (1995).
23. J. F. Lawler, J. G. Lunney and J. M. D. Coey, *Applied Physics Letters* **65** (23), 3017-3018 (1994).
24. J. M. D. Coey and S. Sanvito, *Journal of Physics D: Applied Physics* **37** (7), 988 (2004).
25. J. M. D. Coey and M. Venkatesan, *Journal of Applied Physics* **91** (10), 8345-8350 (2002).
26. C. Zener, *Physical Review* **81** (3), 440-444 (1951).

27. C. Zener, *Physical Review* **82** (3), 403-405 (1951).
28. A. Tebano, C. Aruta, S. Sanna, P. G. Medaglia, G. Balestrino, A. A. Sidorenko, R. De Renzi, G. Ghiringhelli, L. Braicovich, V. Bisogni and N. B. Brookes, *Physical Review Letters* **100** (13), 137401 (2008).
29. M. Opel, *Journal of Physics D-Applied Physics* **45** (3) (2012).
30. A. M. Haghiri-Gosnet and J. P. Renard, *Journal of Physics D: Applied Physics* **36** (8), R127 (2003).
31. M. Cesaria, A. P. Caricato, G. Maruccio and M. Martino, *Journal of Physics: Conference Series* **292** (1), 012003 (2011).
32. J. F. Mitchell, D. N. Argyriou, C. D. Potter, D. G. Hinks, J. D. Jorgensen and S. D. Bader, *Phys. Rev. B* **54** (9), 6172-6183 (1996).
33. M. L. Wilson, J. M. Byers, P. C. Dorsey, J. S. Horwitz, D. B. Chrisey and M. S. Osofsky, *Journal of Applied Physics* **81** (8), 4971-4973 (1997).
34. A. I. Tovstolytkin, A. N. Pogorily, A. I. Matviyenko, A. Y. Vovk and Z. Wang, *Journal of Applied Physics* **98** (4), 043902-043906 (2005).
35. R. Desfeux, S. Bailleul, A. Da Costa, W. Prellier and A. M. Haghiri-Gosnet, *Applied Physics Letters* **78** (23), 3681-3683 (2001).
36. S. Mukhopadhyay, I. Das and S. Banerjee, *Journal of Physics-Condensed Matter* **21** (2) (2009).
37. D. Pesquera, V. Skumryev, F. Sánchez, G. Herranz and J. Fontcuberta, *Phys. Rev. B* **84** (18), 184412 (2011).
38. V. Garcia, M. Bibes, A. Barthélémy, M. Bowen, E. Jacquet, J. P. Contour and A. Fert, *Phys. Rev. B* **69** (5), 052403 (2004).

39. C. Kwon, M. C. Robson, K. C. Kim, J. Y. Gu, S. E. Lofland, S. M. Bhagat, Z. Trajanovic, M. Rajeswari, T. Venkatesan, A. R. Kratz, R. D. Gomez and R. Ramesh, *J. Magn. Magn. Mater.* **172** (3), 229-236 (1997).
40. C. Thiele, K. Dörr, O. Bilani, J. Rödel and L. Schultz, *Phys. Rev. B* **75** (5), 054408 (2007).
41. F. Yang, N. Kemik, M. D. Biegalski, H. M. Christen, E. Arenholz and Y. Takamura, *Applied Physics Letters* **97** (9), 092503-092503 (2010).
42. S. M. Liu, X. B. Zhu, J. Yang, W. H. Song, J. M. Dai and Y. P. Sun, *Ceramics International* **32** (2), 157-162 (2006).
43. V. Bhosle and J. Narayan, *Applied Physics Letters* **90** (10), 101903-101903 (2007).
44. H. Y. Hwang, S. W. Cheong, N. P. Ong and B. Batlogg, *Physical Review Letters* **77** (10), 2041-2044 (1996).
45. R. Mahesh, R. Mahendiran, A. K. Raychaudhuri and C. N. R. Rao, *Applied Physics Letters* **68** (16), 2291-2293 (1996).
46. M. Jaime, M. B. Salamon, K. Pettit, M. Rubinstein, R. E. Treece, J. S. Horwitz and D. B. Chrisey, *Applied Physics Letters* **68** (11), 1576-1578 (1996).
47. H. L. Ju, C. Kwon, Q. Li, R. L. Greene and T. Venkatesan, *Applied Physics Letters* **65** (16), 2108-2110 (1994).
48. D. W. Visser, A. P. Ramirez and M. A. Subramanian, *Physical Review Letters* **78** (20), 3947-3950 (1997).
49. Y. P. Sukhorukov, A. M. Moskvin, N. N. Loshkareva, I. B. Smolyak, V. E. Arkhipov, Y. M. Mukovskii and A. V. Shmatok, *Technical Physics* **46** (6), 778-781 (2001).

50. S. Yamaguchi, Y. Okimoto, K. Ishibashi and Y. Tokura, *Phys. Rev. B* **58** (11), 6862-6870 (1998).
51. E. O. Wollan and W. C. Koehler, *Physical Review* **100** (2), 545-563 (1955).
52. E. Pellegrin, L. H. Tjeng, F. M. F. deGroot, R. Hesper, G. A. Sawatzky, Y. Moritomo and Y. Tokura, *Journal of Electron Spectroscopy and Related Phenomena* **86** (1-3), 115-118 (1997).
53. Y. P. Sukhorukov, A. P. Nosov, N. N. Loshkareva, E. V. Mostovshchikova, A. V. Telegin, E. Favre-Nicolin and L. Ranno, *Journal of Applied Physics* **97** (10), 103710-103715 (2005).
54. Y. S. Du, B. Wang, T. Li, D. B. Yu and H. Yan, *J. Magn. Magn. Mater.* **297** (2), 88-92 (2006).
55. M. Pardavihorvath, *IEEE Trans. Magn.* **21** (5), 1694-1699 (1985).
56. S. K. Arora, H.-C. Wu, R. J. Choudhary, I. V. Shvets, O. N. Mryasov, H. Yao and W. Y. Ching, *Phys. Rev. B* **77** (13), 134443 (2008).
57. M. Huijben, L. W. Martin, Y. H. Chu, M. B. Holcomb, P. Yu, G. Rijnders, D. H. A. Blank and R. Ramesh, *Phys. Rev. B* **78** (9) (2008).
58. H. Boschker, M. Huijben, A. Vailionis, J. Verbeeck, S. van Aert, M. Luysberg, S. Bals, G. van Tendeloo, E. P. Houwman, G. Koster, D. H. A. Blank and G. Rijnders, *Journal of Physics D-Applied Physics* **44** (20) (2011).
59. M. A. Geday and A. M. Glazer, *Journal of Physics-Condensed Matter* **16** (20), 3303-3310 (2004).
60. K. van Benthem, C. Elsasser and R. H. French, *Journal of Applied Physics* **90** (12), 6156-6164 (2001).

Chapter 5

Multiferroic Manganite GdMnO₃

5.1 Introduction

In recent years, multiferroic materials have attracted much attention due to both their physical properties and their promising applications. Multiferroic materials exhibit ferroelectric and ferromagnetic properties simultaneously in the same phase. This allows one to control the electric polarisation by the application of a magnetic field or, *vice versa*, to control the magnetic properties by an electric field. Together with recent unprecedented progress in epitaxial thin film growth, this unique property makes these well-known materials very good candidates with which to build multifunctional spintronic devices [2-3].

Currently, the heart of the problem is to find examples of multiferroic materials. The coupling of both ferroelectric and ferromagnetic properties in a multiferroic can be controlled indirectly through the strain [4]. This phenomenon in multiferroic materials is the key to developing novel spintronic devices. However, these novel devices require a very high quality of thin film, rather than bulk material, this requirement being the central challenge for the researcher. Probably the most promising class of multiferroic materials are the perovskite manganites, RMnO₃, where R is a rare-earth element or bismuth (R=Ho, Er, Tm, La, Sm, Gd,.....) [4-6]. In this chapter we shall study the magnetic, optical and magneto-optical properties of epitaxial films of gadolinium manganite (GdMnO₃) in order to obtain detailed information on the magnetic polarisation of the electronic states. The first section of

this chapter provides a literature review of multiferroic materials and the second section investigates the magnetic and magneto-optical properties. The data presented in this chapter have been accepted for publication.

5.2 Literature Review on the Multiferroic, Gadolinium Manganite (GdMnO₃)

The study of multiferroic materials began in the 1960's by Smolenskii and Venevtsev in the then Soviet Union [7]. This field was very quiet for some time, and renewed interest in multiferroics started around 2001-2003. In recent years, the rare-earth manganites (RMnO₃) have been found to have large magneto-electric effects [7-9]. This makes the perovskite manganites (RMnO₃) very promising multiferroic materials. with regard to the structure, these manganites can be classified into two groups: a hexagonal phase with R (= Ho, Er, Tm, Yb or Y) and an orthorhombic phase with R (= La, Pr, Nd, Sm, Eu, Gd, Tb or Dy) [9]. However, some compounds in the orthorhombic group could be grown in a metastable hexagonal phase and *vice versa*. This could be achieved by an epitaxial stabilization technique, which required high oxygen pressure and a suitable substrate [10-12].

On lowering the temperature, most of the hexagonal RMnO₃ manganites display three kind of magnetic ordering transitions: 120°-oriented antiferromagnetic at 70-85 K, 90° rotation of Mn³⁺ spins, known as reorientation transition, at 40 K and ferromagnetic ordering below 5K due to the magnetic interaction between rare-earth ions [10, 13-14]. In the structure of hexagonal manganites, the ferroelectric and magnetic ordering do not occur together, since the electric polarization appears far above room temperature and the magnetism appears below this temperature [8, 15]. In

contrast, the magnetic and the ferroelectric ordering transition temperatures are comparable for manganites with orthorhombic structure [8, 16-17].

The orthorhombic structures occur where the lanthanide ions have a large ionic radius, whereas hexagonal structures occur where the lanthanide ions have a small ionic radius. A decrease of rare-earth ionic radius (r_R) in orthorhombic manganites $RMnO_3$ enhances the competition in magnetic interaction [1]. The FM interaction occurs between nearest-neighbour Mn ion and the AF interaction occurs between next-nearest neighbour ions [1, 18].

T.Kimura et al reported [1] the magnetic phase diagram for the orthorhombic manganites $RMnO_3$ as a function of ionic radius as indicated in fig.5.1.

**Removed by the
author for copyright reasons**

Figure (5.1): The magnetic phase diagram of $RMnO_3$ as a function of ionic radius R . The open triangles denote the Néel temperature for Mn moments T_N (Mn), closed triangles denote the lock-in transition temperature T_{lock} and cross the Néel temperature for R moments $T_N(R)$ [1].

The Néel temperature (T_N) increases with increasing ionic radius, where T_N for GdMnO₃ is about 43 K and the lock-in temperature (T_{lock}) about 23 K. T_{lock} is the temperature at which the ferroelectric polarisation vector is switched from being directed along a given axis to a different axis by the application of a magnetic field [17]. Among R³⁺ 4f ions in rare-earth manganites RMnO₃, the Gd³⁺ ion in GdMnO₃ has a large effective spin moment ($S=7/2$) and large $g[J(J+1)]^{1/2}$ factor. These two properties could give a significant enhancement of ferromagnetic properties in GdMnO₃ [10].

The magnetic transitions in the orthorhombic manganites RMnO₃ is currently understood with the help of two key ingredients. Firstly, magnetic frustration due to competing exchange integrals between successive neighbours stabilizes a spiral magnetic phase below the T_N [17, 19]. Secondly, there is a lock-in transition to a canted A-type antiferromagnetic phase. At lower temperature still the Gd moments order and the oxygen atoms are pushed off the Mn-Mn bond, driving an electric polarisation at this transition for GdMnO₃. Therefore, the charge, spin orbital and lattice subsystems are linked very tightly in these materials and the strain in the thin films plays a crucial role in determining the properties of the materials.

The magnetic phase diagram (H-T) has been mapped out for bulk crystals [20-21] as a function of temperature and magnetic field. It was found that the H-T phases are field-orientation dependent along the a, b and c axes. As shown in fig.5.2 the transition from the paramagnetic (PM) to an incommensurate antiferromagnetic (ICAFM) occurs with around $T_N=42$ K. The transition from (ICAFM) to a canted A-type antiferromagnet (cAFM) and a transition to ferroelectric (FE) occurs at $T_c=20$ K and 12 K, respectively for magnetic fields above 2 T.

Removed by the author for copyright reasons

Figure (5.2): Phase diagram of GdMnO₃ for magnetic field along the b axis. Closed and open symbols are obtained with increasing and decreasing T or H , respectively. Shaded areas indicate regions of strong hysteresis [8].

It was found that, as the temperature is lowered, the spiral magnetic order in GdMnO₃ occurs at $T_N=47$ K and there is a transition between the paramagnetic phase and an antiferromagnetic phase and an A-type antiferromagnetic transition at 19 K [8, 17, 22]. In zero field there is a transition to a canted phase at about 18 K and the Gd spins order at close to 7 K. However, below 20 K there is strong hysteresis so that several phases can co-exist [21]. The phase boundaries depend both on the magnitude of the magnetic field and its direction. In particular a ferroelectric phase appears below 7 K for magnetic fields greater than 2 T along the b axis. The phase diagram is very dependent on pressure [8, 22], as expected due to the existence of a ferroelectric phase. The first phase transition was found to be shifted to 44 K for nanoparticles with a mean size of 52 nm [23] as indicated in fig.5.3. Weak ferromagnetism appears in FC mode at 20 K, which is attributed to the canted Mn spins and polarisation of Gd 4f

spins. At 7 K, the canted Gd spins are antiparallel to those of the canted Mn spins, due to the interaction of Gd 4f spins. Moreover, a ferromagnetic-like loop was reported at 2 K for GdMnO₃ nanoparticles [23] this is due to large contribution of the net moment of Gd spins compared to that of the antiferromagnetic canted Mn spins.

**Removed by the
author for copyright reasons**

Figure (5.3): ZFC and FC magnetisation of GdMnO₃ nanoparticles measured in 100 Oe between 2 and 60 K. The inset is the temperature dependence of the derivative dM/dT [23].

The optical absorption spectra for rare-earth manganite RMnO₃ including GdMnO₃ show a strong transition at the 3.53 eV band edge. However, in LaMnO₃ a particular interesting feature is seen at about 2 eV as is shown in fig.5.4. This clear peak is due to a charge transfer excitation between neighbouring Mn ions; the reduction in the intensity has been related to the different canting of the Mn d-orbitals

and also on the directions of Mn spins and the Mn-O-Mn bond angle [24-25]. The only magneto-optical studies on a related material reported a strong magnetic field dependent peak at near 3 eV in single-crystal of TbMnO₃ [26].

**Removed by the
author for copyright reasons**

Figure (5.4): Absorption spectra of RMnO₃ thin films measured at room temperature shows a transition peak at 2 eV being suppressed for Gd and Tb [25].

5.3 Experimental Results and Discussion

The GdMnO₃ target was prepared from a high-purity stoichiometric mixture of Gd₂O₃ and MnO₂ powders. Films were grown by Ya. Mukovski in the laboratory of the National University of Science and Technology, Moscow, Russia. The films were sputtered in an atmosphere of Ar and O₂ at a pressure of 1-2 mTorr. The substrate temperature was maintained at 650 °C during the growth process. Epitaxial films of thickness 100-200 nm were grown on LaAlO₃ (LAO) and SrTiO₃ (STO) substrates with the [110]-direction parallel to the plane of the substrate. X-ray diffraction (XRD) was also used to study the structure of the films, as shown in fig.5.5.

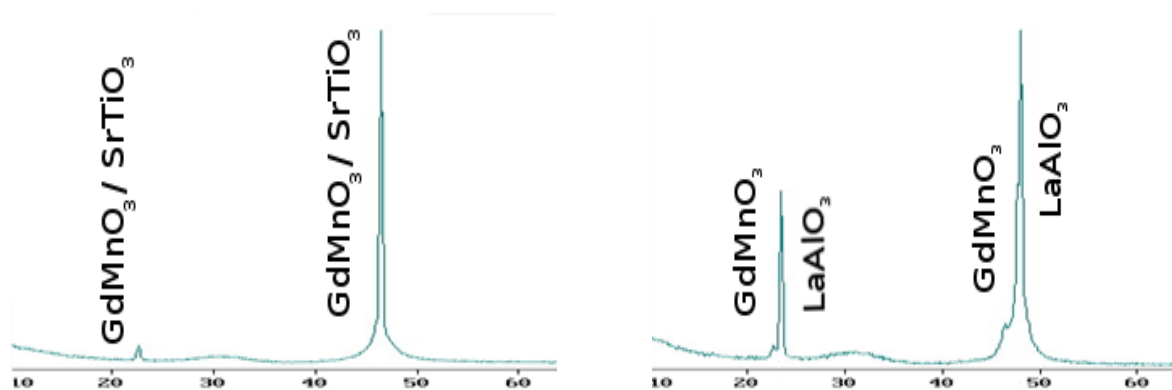


Figure (5.5): X-ray data of GdMnO₃ films grown on STO₃ and LAO substrate.

Fig.5.5 shows XRD patterns taken at room temperature for the GdMnO₃ films grown on the STO and LAO substrates. The data indicates an epitaxial growth for both films with films oriented with the substrates. The strong reflection peak at $2\theta = 47^\circ$ corresponds to the (431) GdMnO₃ orientation. The LAO was found to be heavily twinned and the STO substrate undergoes a structural transition at about

100K; this may produce further strains on the film in the temperature range where the magnetic ordering occurs.

5.3.1 Magnetic Measurements

Magnetic properties of the GdMnO₃ films were investigated using the SQUID magnetometer. Measurement was made in the temperature range of 5-400 K with a field up to 1 T in-plane. FC and (ZFC) measurement was achieved in a field of 0.01 T. Fig.5.6 shows the ZFC and FC magnetization of GdMnO₃ films after the contribution from the substrates has been subtracted.

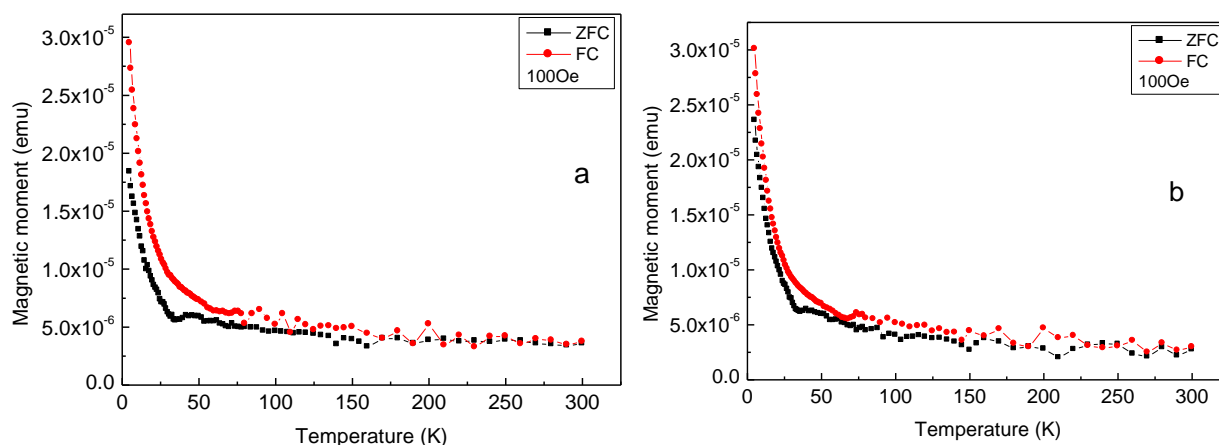


Fig.5.6: ZFC and FC data taken in an in-plane field of 100 Oe for films of GdMnO₃ on a) STO and b) LAO substrates. The data for the bare substrate has been subtracted.

The transition to the antiferromagnetic phase shows up most clearly in the ZFC plots; however it is shifted to lower temperature. For the films on the STO substrate, it occurs at 44 K and for the film on LAO substrate 40 K. These should be compared with the temperature of 44 K observed for GdMnO₃ nanoparticles [23] and 47 K in bulk material. This indicates that the strain induced by the substrate is

significant in reducing T_N . Moreover, the exchange interactions between the Mn ions are very sensitive to strain [17].

Fig.5.7 shows the temperature dependence of the inverse susceptibility taken from both the FC and ZFC measurements. There are small changes in the slope of the inverse susceptibility, which are marked with arrows on the plots. These occur at 14 K for both films; this is tentatively identified as the lock-in temperature. There is an additional, weak change of slope at 8 K for the film on STO, which is identified as the ordering temperature of the Gd ions; another weak feature also occurs at 108 K, which is the temperature of the structural transition in the STO substrate.

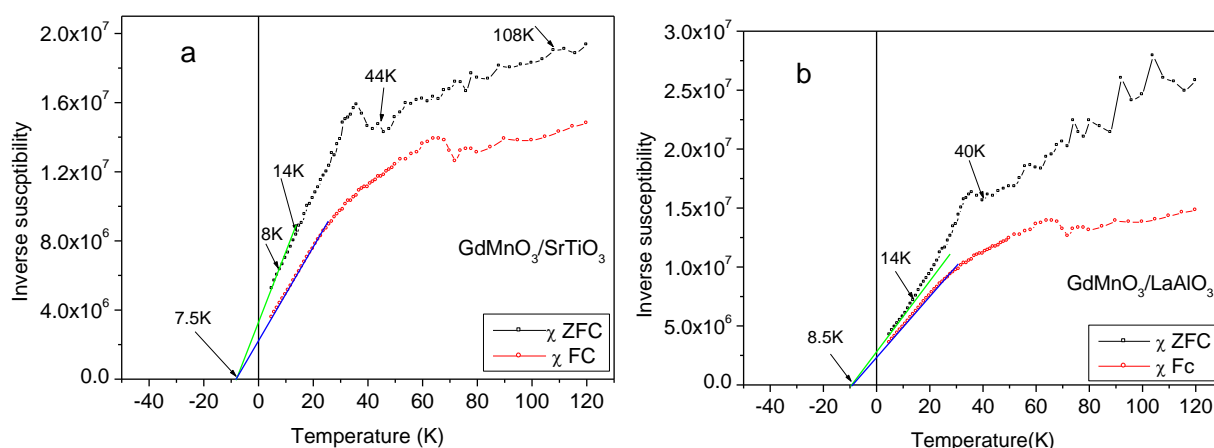


Figure (5.7): The inverse susceptibilities, evaluated from both the FC and ZFC data are plotted as a function of temperature for the films on (a) STO and (b) LAO substrates. The magnetic transitions are marked on these plots.

The slope of the inverse susceptibility is extrapolated to give the Curie-Weiss constant. This gives a value of 7.5 ± 0.23 K and 8.5 ± 0.30 K for the films on the STO and LAO respectively. The slope of the line is the inverse Curie constant, which is expected to arise from the paramagnetic Gd spins and a weakly temperature

dependent susceptibility from the Mn ions. The expected paramagnetic susceptibility (χ) from Gd ions was calculated using:

$$\chi = \frac{N \times g^2 \times \mu_B^2 \times s(s+1)}{3K_B \times (T+\theta)} = \frac{C(Gd)}{T+\theta}, \quad 5.1$$

where, N is the number of Gd ions per cm³ in the film, μ_B the Bohr magnetons, the electron spin, $s=7/2$ and $g=2$; the total susceptibility is then given as:

$$\chi_{meas} = \frac{C(Gd)}{T+\theta} + \chi_{Mn} = \frac{C(Gd) + \chi_{Mn}(T+\theta)}{T+\theta} = \frac{C_{meas}}{T+\theta} \quad 5.2$$

The measured values of the Curie constant (C_{meas}) for the FC and ZFC plots for both films and the calculated value of Gd ions (C (Gd)) are given in Table (5.1). The C_{meas} experimental are higher than the calculated values for Gd ions (C (Gd)) which is good evidence for the canted antiferromagnetic contribution from the Mn ions; this is enhanced with magnetic field.

The film	$C(Gd) \times 10^6$	$C_{meas}^{zfc} \times 10^6$	$C_{meas}^{fc} \times 10^6$
GdMnO ₃ on STO	1.13	2.55	3.77
GdMnO ₃ on ALO	1.13	3.41	3.82

Tale (5.1): shows the calculated and the measured values of the Curie constant for GdMnO₃ films grown on STO and ALO substrates. C (Gd) denote the Curie constant values calculated for Gd ions, C_{meas}^{zfc} the Curie constant values measured from ZFC and C_{meas}^{fc} the Curie constant values measured from FC.

The magnetisation hysteresis loops of the GdMnO₃ films grown on STO and LAO substrate were measured under an applied magnetic field up to 1 T parallel to the surface of all films. The contribution from the substrates, that varied linearly with

field in the range of 7 kOe -10 kOe, has been subtracted. Fig.5.8 shows the hysteresis loops at 5 K and 10 K, the moment is higher at 5 K in the film grown on LAO; there is no clear signal at 20 K or higher. A coercive field should appear as the canted phase is entered. The values of the coercive fields of these films are 330 ± 10 Oe and 301 ± 11 Oe at 5 K whereas the coercive fields at 10 K are 120 ± 6 Oe and 136 ± 8 Oe for the films grown on STO and LAO, respectively.

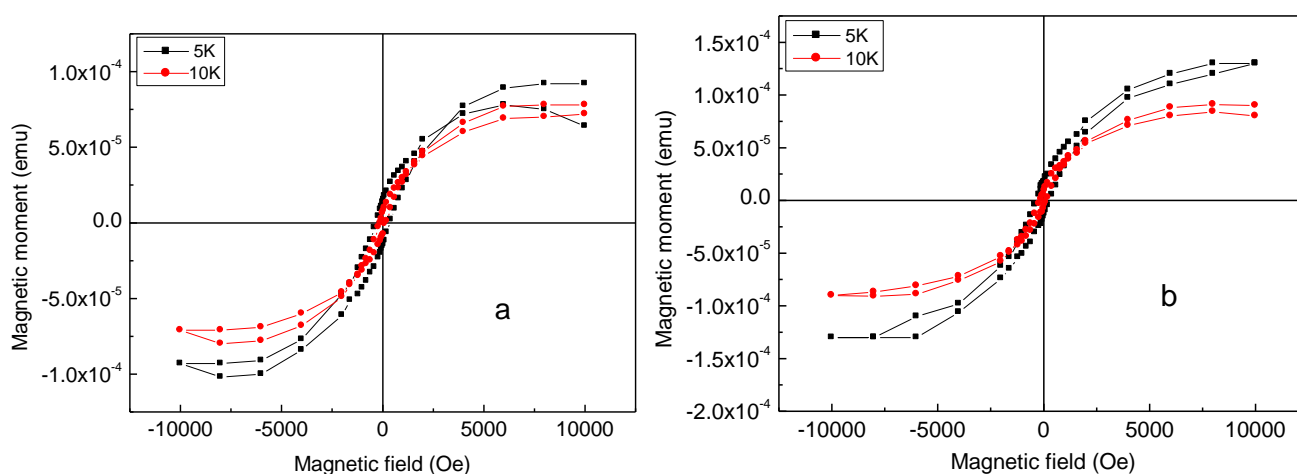


Figure (5.8): The hysteresis loops for the field in-plane (with linear background subtracted) at temperatures 5 K and 10 K for the films on (a) STO and (b) LAO substrates.

Fig. 5.9 shows the linear contribution that was subtracted from the raw data in order to obtain the hysteresis loops shown in fig.5.8 at 5 K and 10 K. The subtracted contribution was due to the diamagnetic signal from the substrate and a paramagnetic signal from the film. The susceptibility at 7 kOe for the GdMnO₃ films is shown in fig.5.10 after the contribution from the substrates has been subtracted. The high field susceptibility is large at low temperatures, following the low field susceptibility, as shown in fig.5.6.

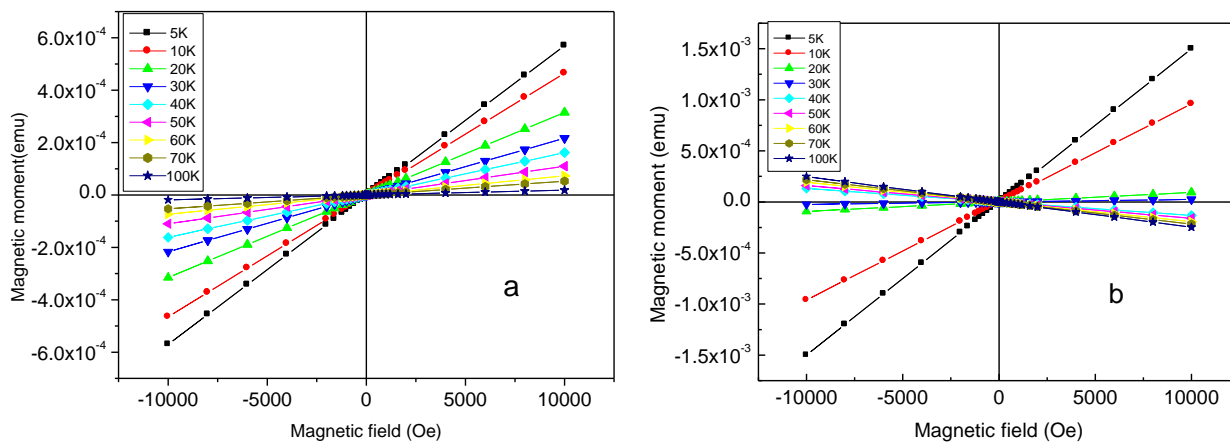


Figure (5.9): The linear contribution that was subtracted from the raw data to obtain the correct loops for the films (a) on the STO substrate (b) on the LAO substrate.

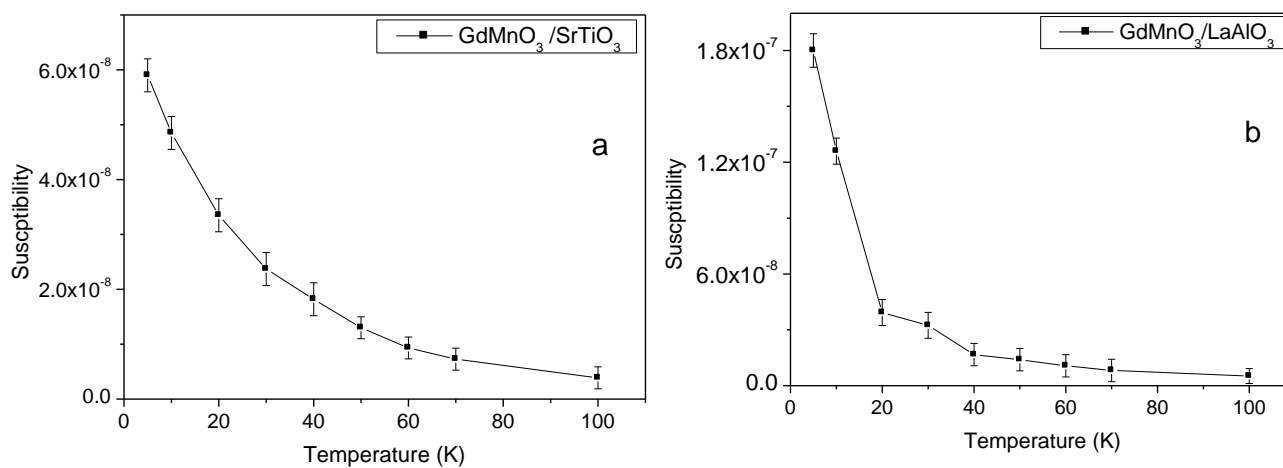


Figure (5.10): The susceptibility at 7 kOe for the GdMnO₃ (a) on the STO substrate (b) on the LAO substrate. The contribution from the substrates has been subtracted.

5.3.2 Optical Measurements

The transmission and reflection spectra of GdMnO₃ films were measured directly in order to determine the absorption spectrum. The optical data were recorded at room temperature using of a 250 watts tungsten halogen lamp to cover a wide spectral range from 1.7 eV to 4.5 eV. The transmission spectra for the blank substrates were measured, but the LAO data was excluded because of the birefringence behaviour. The transmission spectrum of the STO substrate shows no transmission at higher energies, then, with decrease of energy, the transmission increases sharply at 3.2eV to about 70% as shown in fig.5.11.

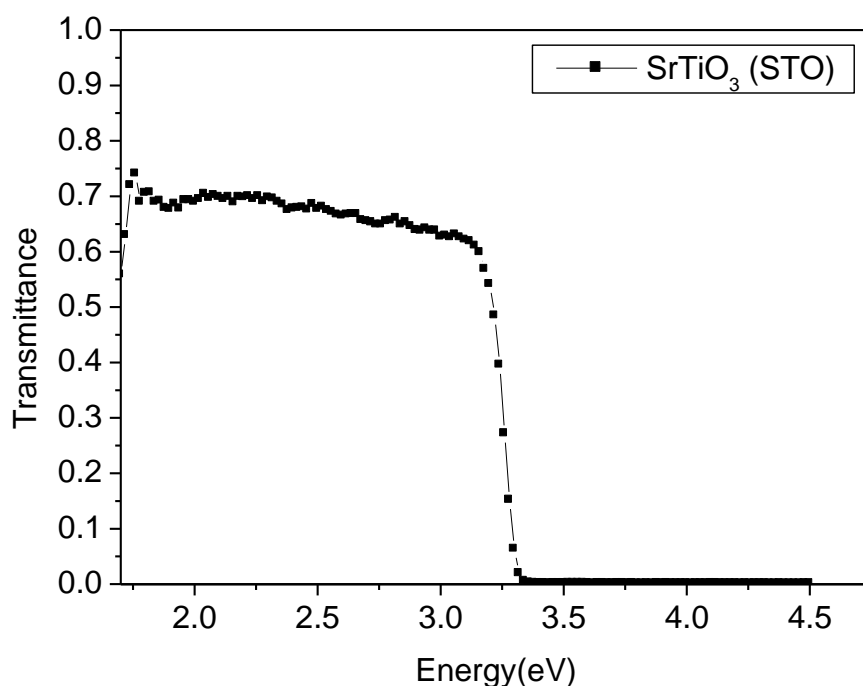


Figure (5.11): Transmittance spectrum for the STO substrate, which absorbs strongly above 3.2 eV.

Fig.5.12 shows the transmission spectra of the GdMnO₃ films grown on STO and LAO substrates and measured at room temperature

The absorption spectra were recorded for the both GdMnO₃ films grown on both STO and LAO substrates as shown in Fig.5.13. The absorption spectra of the GdMnO₃ films exhibit an absorption shoulder below the band gap energy; whereas this feature does not appear in the STO absorption spectrum (fig. 4.22 in chapter 4).

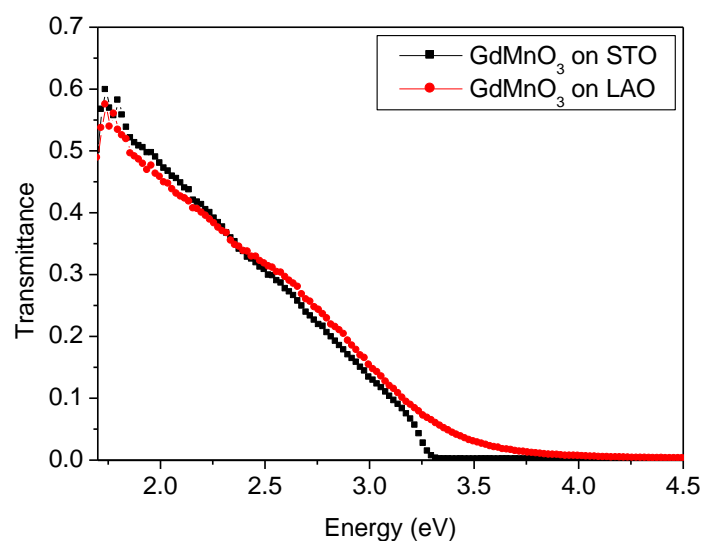


Figure (5.12): Transmittance spectra for GdMnO₃ films grown on STO substrate and LAO substrates.

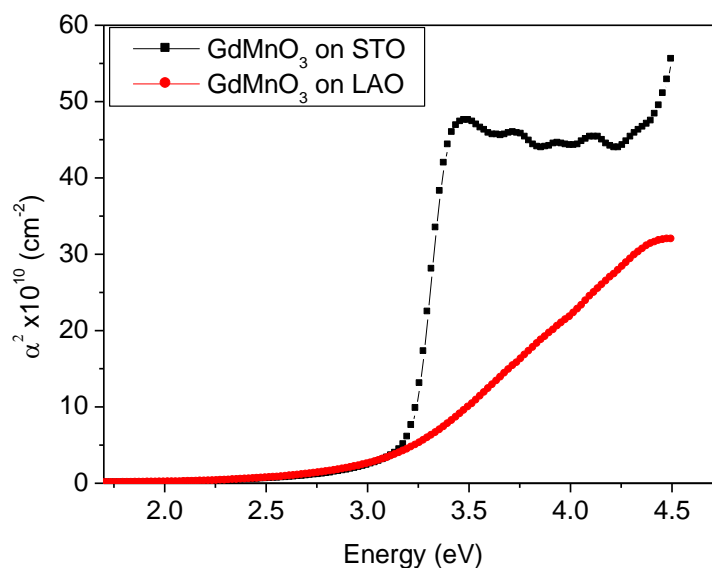


Figure (5.13): The absorption α^2 measured at room temperature for GdMnO₃ films grown on STO and LAO substrate.

The optical absorption coefficient of GdMnO₃ films grown on STO and LAO substrates confirms the formation of the absorption shoulder below 3.2 eV; once again, this shoulder does not appear in the STO data as shown in fig.5.14.

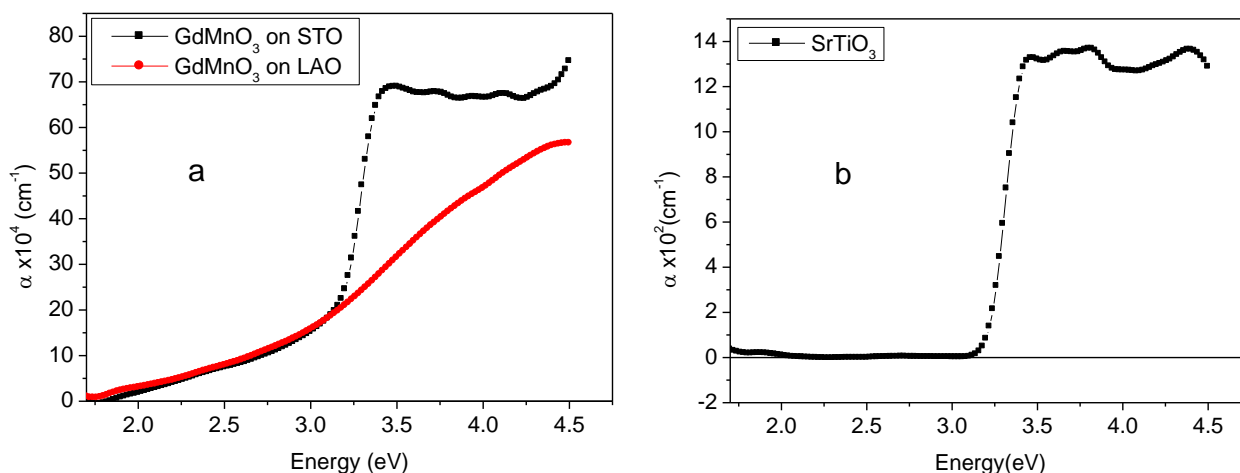


Figure (5.14): the optical absorption coefficient (α) measured at room temperature a) for GdMnO₃ films on STO and LAO substrate b) for STO substrate only.

The absorption for the sample on LAO behaves as expected; it rises smoothly from a gap at ~ 3.48 eV up to the highest energy measured, 4.5 eV. This is due to charge transfer transitions from the oxygen 2*p* band to the unoccupied Mn *d* states. These states are in the higher *e_g* orbital, but with spin parallel to that of the electron in the occupied *e_g* orbital [24]. The data for the film on the STO substrate is only meaningful below 3.2 eV, because the absorption at higher energies is dominated by the substrate absorption edge [27]. The absorption at ~ 2 eV that is seen in the spectrum of LaMnO₃, which is due to a charge transfer excitation between Mn ions, is strongly suppressed in these measurements; due to the canting of the Mn *d*-orbitals [24-26].

The magneto-optics, MCD, spectra were measured in Faraday geometry, where the magnetic field is applied normal to the plane of the film, *i.e.* along the *c*-axis. The MCD spectra of the GdMnO₃ on the LAO substrate exhibit a birefringence. Hence, if light passes through a crystal in the *z* direction and there are different fast and slow directions in the *x-y* plane with two refractive indices $n+\delta n$ and $n-\delta n$, then the MCD spectra will exhibit oscillations in intensity. The MCD spectrum for this film was measured in a field and in zero field at different orientations in order to avoid the birefringence. However, it seems that the birefringence arises entirely from the substrate and dominates the spectra measured in MCD geometry and there is no way to avoid it, see fig.5.15. Therefore, it does not seem possible to look for the strain effects related to the ferroelectricity in this film.

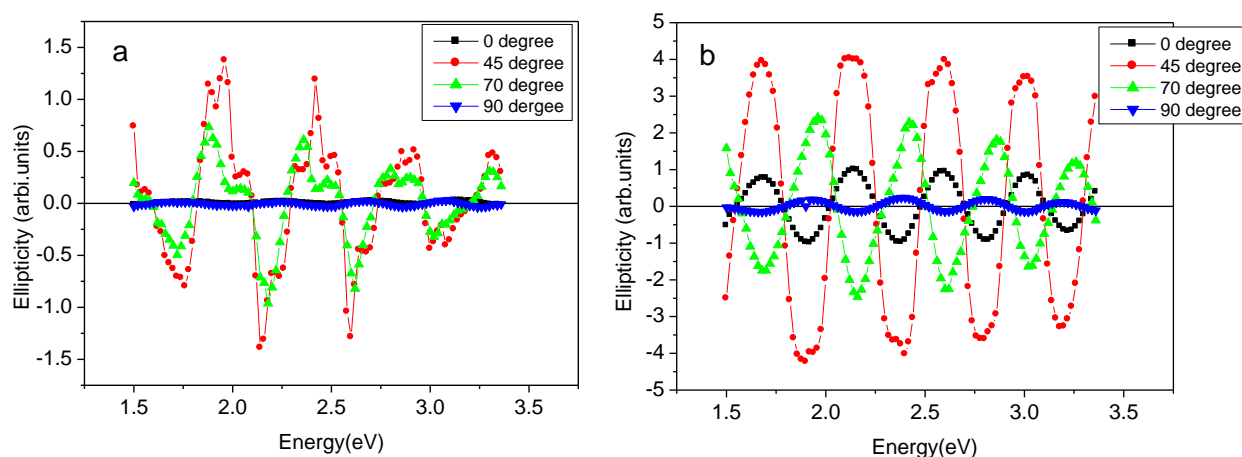


Figure (5.15): Ellipticity spectra measured at room temperature for a GdMnO₃ film on LAO substrate measured a) in a magnetic field, b) in zero field. These show the importance of birefringence in LAO on these measurements.

The STO substrate undergoes a structural transition at about 100 K which gives rise to the birefringence, unless the *E* vector of the light is along one of the optic axes [28]. The samples were oriented carefully so this effect was not a perturbing

feature. The temperature dependence of the MCD obtained from a blank substrate was measured and these spectra were subtracted from the spectra of the film on the substrate in order to obtain just the contribution from the film. Fig.5.16 shows the MCD spectrum as a function of temperature for the GdMnO₃ films grown on STO in fields up to 0.5 T. This measurement was undertaken with the help of Alshammari in the University of Sheffield. The plot shows two main spectral features a positive feature at 2 eV and a negative feature at about 3 eV. In GdMnO₃ the shape of the MCD spectrum near 2 eV follows the expected absorption because the allowed transitions are dominated by the spin occupations of the Mn d orbitals. Transitions to unoccupied d levels with opposite spin are higher in energy by the Hubbard energy, $JH \sim 1$ eV, and so would appear at different parts of the spectrum.

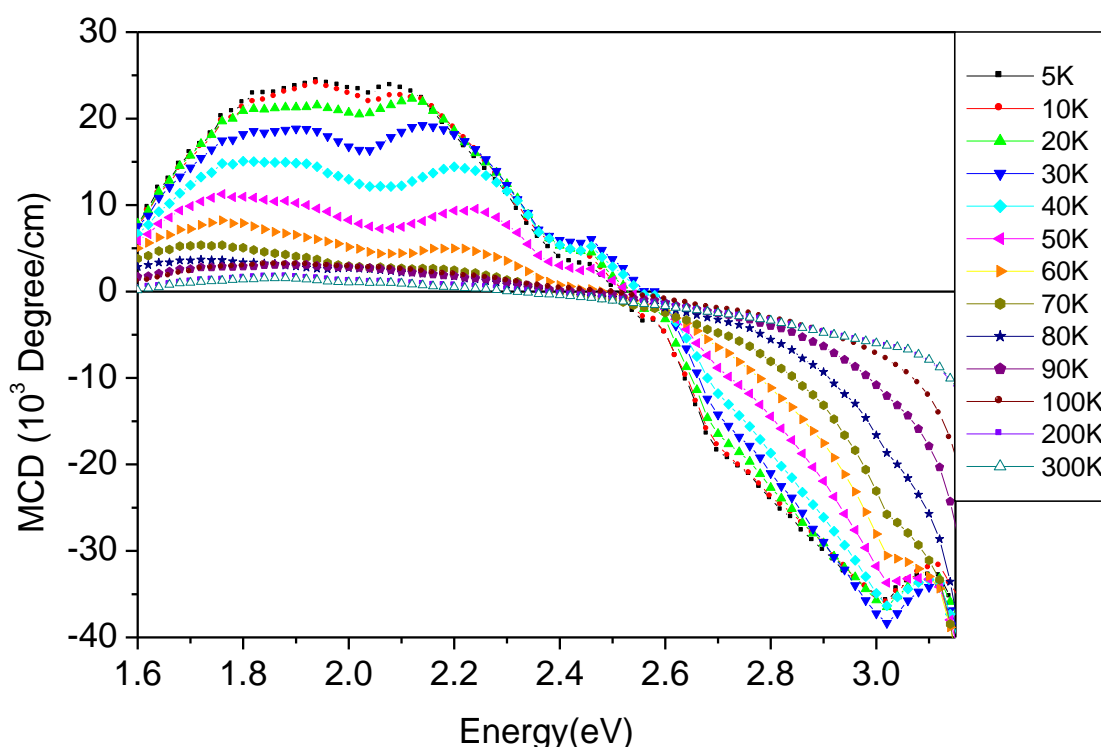


Figure (5.16): Temperature dependence of the MCD of GdMnO₃ measured at 0.5 T. The contribution from a blank STO substrate has been subtracted from this data.

In order to study these features in an optimal way, the spectrum in zero field was measured after having reduced the field to zero from values of 5 Oe, this is the spectrum taken at remanence and is shown in fig.5.17. This measurement was made with the help of Alshammari.

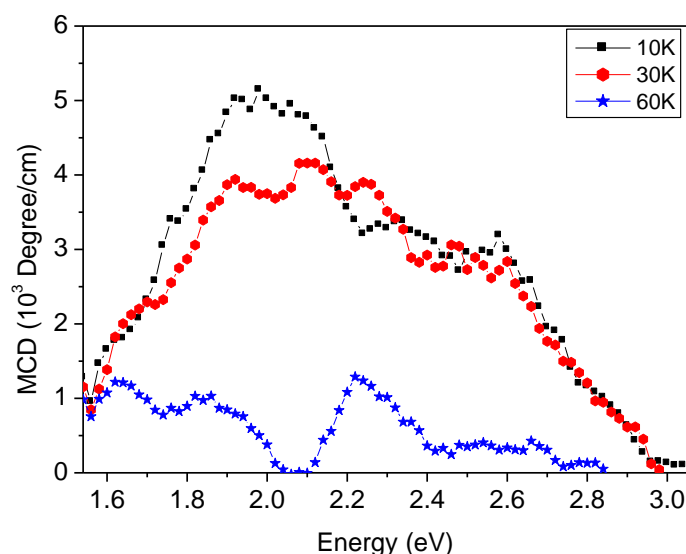


Figure (5.17): The MCD spectrum taken at remanence for GdMnO₃ on SrTiO₃ there is a finite spectrum at 10 K and 30 K, the spectrum at 60 K is almost zero. The spectra for a blank substrate taken at remanence (which was anyway very small) has been subtracted from this data.

The two sets of data measured in a field and at remanence are very surprising, because the spectral shapes of the MCD spectra taken in field and at remanence are so dissimilar, which is, as far as is known, a unique occurrence. One expects that the remnant spectrum should have the same shape as the spectrum taken in a field, but with a magnitude scaled by the ratio of the remnant magnetisation to the applied magnetisation. The peak at ~2 eV at 10 K in the remnant spectrum has been reduced

by a factor of ~ 5 relative to its value in field; this is comparable to the ratio of M_r/M_s observable in the SQUID data shown in fig.5.8.

These spectra can be understood when it is realised that the two optical features at 3 eV and the 2 eV peak give two distinct components of the MCD spectra with different temperature and field dependencies.

The negative feature occurring at 3 eV and it changes only slightly between 5 K and 40 K, in spite of the fact that the susceptibility is rising strongly over this temperature range; also, a finite MCD signal is visible out to high temperatures. This feature vanishes when the magnetic field is zero. Moreover, close to the structural transition of STO at ~ 100 K it was also found to exhibit a large, strongly temperature dependent, circular dichroism just below its band gap that varied linearly with the applied magnetic field as will be discussed later in chapter 6. This signal was considerably larger than the MCD of the film, because the thickness of the substrate, 0.5mm, was so much larger than that of the film ~ 100 nm; since it had a strong temperature dependence, it was very hard to subtract the substrate data from the data taken with the film. Since the substrate dichroism was purely paramagnetic, it did not contribute to the remnant spectrum shown in fig.5.17. The MCD peak at 3 eV shown in fig.5.15 is, therefore, due to the remaining contribution from the STO Substrate.

The energy of the transition at about 2 eV is characteristic of the charge transfer transition between neighbouring Mn ions and depends on the overlap of the spin states such that for adjacent spins oriented at an angle (θ) to each other this varies as $\cos(\theta/2)$ [25, 29]. This could not be detected in the optical absorption data shown in Fig. 5.13. The strength of this peak in the MCD spectrum as shown in Fig.5.16 decreases much more rapidly with temperature, than the strength of the peak at 3 eV. For example, there is a significant drop in the intensity of the 2 eV peak at

30 K relative to 5 K and it has been suppressed almost to zero at 60 K, whereas the intensity of the 3 eV peak at 30 K is changed very little compared with the data taken at 5 K and the intensity at 60 K has only dropped by a factor of ~ 2 . This is consistent with the strength of the 2 eV peak depending on the relative spin directions of two neighbouring Mn ions, as it increases below the transition to the canted A-phase, where the spins in the a - b planes are parallel. On the other hand, it is this peak that survives in the remanence spectrum. One would expect a finite remnant spectrum only when there is magnetic hysteresis, which should occur below the transition to the canted phase at 18 K, and so it is very surprising to obtain such a high remanence spectrum at 30 K. It is possible that the strain in the film is inducing a canted phase already at T_N . The peak in LaMnO₃ that was suppressed at ~ 2 eV is, in fact, 3 peaks at 1.9 eV, 2.3 eV and 2.6 eV and there are features in the remanence spectra that might correspond to these peaks; this, however, is not certain. It is clear that the 2 eV peak can be studied much better using MCD at remanence than in any other mode, because other features are absent.

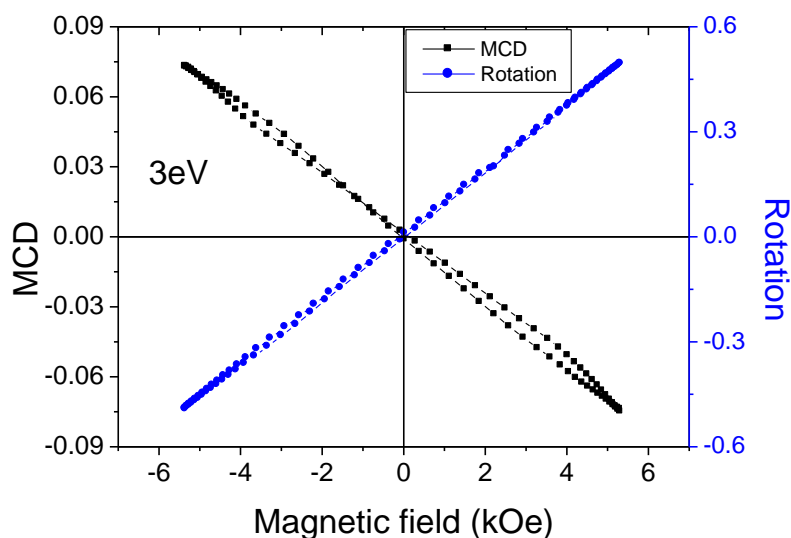


Figure (5.18): MCD and Faraday hysteresis loops obtained from magneto-optics measurements (in arbitrary units) at 3 eV and 10 K.

In order to understand the MCD spectra, hysteresis loops were measured using MCD and Faraday rotation at different energies. It should be noted that the substrate contributes to the loop signals. Fig.5.18 shows the loop obtained at 10 K and at 3 eV as measured by Alshammari. The MCD loop was strongly energy-dependent, as expected from the MCD spectra; the loop obtained with Faraday rotation is very weakly dependent on energy, therefore, it is shown only at 3 eV; it is also more influenced by the contribution from the substrate. The loop at 3 eV has a very small remanence, as expected from the data in Fig.5.16 and the coercive field of ~10 Oe seen in this hysteresis loop was anomalously low, compared with the value of 120 Oe seen in the SQUID data at 10 K. However, this may be due to the small coercivity of the substrate. The MCD and Faraday hysteresis loops at 3 eV confirm a large paramagnetic response below the STO band gap. So that the optical and magneto-optical properties of STO substrate is studied in detail as shown in chapter 6.

5.4 Summary and Conclusions

This chapter reported on the investigation of the magnetic, optical and magneto-optical properties of epitaxial films of GdMnO₃ grown on STO and LAO substrate. Epitaxial films of GdMnO₃ were grown on SrTiO₃ and LaAlO₃ substrates using sputtering technique. The LaAlO₃ was twinned and so produced a highly strained film whereas the strain was less for the film grown on SrTiO₃. There is a structural transition in SrTiO₃ at ~100 K [28, 30] and this may be straining the film grown on this substrate at low temperatures. The Néel temperature is reduced and there is some evidence that a canted phase appears with the onset of anti-ferromagnetism.

The two well-known features in the optical spectrum [24-25], the charge transfer transition between Mn *d* states at ~2 eV and the band edge transition from the oxygen *p* band to the *d* states at ~3 eV are observed in the magnetic circular dichroism (MCD); however they behaved very differently both as a function of magnetic field and temperature. The optical absorption at 3 eV is much stronger than that at 2 eV however the MCD is considerably stronger at 2 eV. The MCD at ~2 eV correlates well with the Mn spin ordering and it is very notable that the same structure appears on this spectrum as is seen in LaMnO₃ [25]. The result shows that the MCD peak at 3 eV is dominated by the optical and birefringence properties of the SrTiO₃ substrate and the absorption of SrTiO₃ substrate above its band gap at about 3.27 eV was actually a limiting feature in this study. Over all, it would have been very difficult to understand the MCD in field without also having the spectrum taken at remanence which underlines the importance of this type of measurement.

5.5 References

1. T. Kimura, G. Lawes, T. Goto, Y. Tokura and A. P. Ramirez, *Phys. Rev. B* **71** (22) (2005).
2. H. Béa and et al., *Journal of Physics: Condensed Matter* **20** (43), 434221 (2008).
3. L. W. Martin and et al., *Journal of Physics: Condensed Matter* **20** (43), 434220 (2008).
4. G. Rogez, N. Viart and M. Drillon, *Angew. Chem.-Int. Edit.* **49** (11), 1921-1923 (2010).
5. M. Gajek, M. Bibes, S. Fusil, K. Bouzehouane, J. Fontcuberta, A. Barthelemy and A. Fert, *Nat Mater* **6** (4), 296-302 (2007).
6. R. Ramesh and N. A. Spaldin, *Nat Mater* **6** (1), 21-29 (2007).
7. D. I. Khomskii, *J. Magn. Magn. Mater.* **306** (1), 1-8 (2006).
8. J. Baier, D. Meier, K. Berggold, J. Hemberger, A. Balbashov, J. A. Mydosh and T. Lorenz, *Phys. Rev. B* **73** (10), 100402 (2006).
9. C. Renu, N. R. Mala, S. L. Chaplot, N. K. Gaur and R. K. Singh, *New Journal of Physics* **11** (7), 073041 (2009).
10. D. Lee, J. H. Lee, P. Murugavel, S. Y. Jang, T. W. Noh, Y. Jo, M. H. Jung, Y. D. Ko and J. S. Chung, *Appl. Phys. Lett.* **90** (18) (2007).
11. J. H. Lee, P. Murugavel, D. Lee, T. W. Noh, Y. Jo, M. H. Jung, K. H. Jang and J. G. Park, *Appl. Phys. Lett.* **90** (1), 012903-012903 (2007).
12. J. H. Lee, P. Murugavel, H. Ryu, D. Lee, J. Y. Jo, J. W. Kim, H. J. Kim, K. H. Kim, Y. Jo, M. H. Jung, Y. H. Oh, Y. W. Kim, J. G. Yoon, J. S. Chung and T. W. Noh, *Advanced Materials* **18** (23), 3125-3129 (2006).

13. B. Lorenz, A. P. Litvinchuk, M. M. Gospodinov and C. W. Chu, *Physical Review Letters* **92** (8), 087204 (2004).
14. T. Lottermoser, T. Lonkai, U. Amann, D. Hohlwein, J. Ihringer and M. Fiebig, *Nature* **430** (6999), 541-544 (2004).
15. M. Fiebig, T. Lottermoser, D. Frohlich, A. V. Goltsev and R. V. Pisarev, *Nature* **419** (6909), 818-820 (2002).
16. T. Goto, T. Kimura, G. Lawes, A. P. Ramirez and Y. Tokura, *Physical Review Letters* **92** (25), 257201 (2004).
17. T. Kimura, T. Goto, H. Shintani, K. Ishizaka, T. Arima and Y. Tokura, *Nature* **426** (6962), 55-58 (2003).
18. T. Kimura, S. Ishihara, H. Shintani, T. Arima, K. T. Takahashi, K. Ishizaka and Y. Tokura, *Phys. Rev. B* **68** (6), 060403 (2003).
19. B. H. Kim and B. I. Min, *Phys. Rev. B* **80** (6), 064416 (2009).
20. J. Hemberger, S. Lobina, H. A. Krug von Nidda, N. Tristan, V. Y. Ivanov, A. A. Mukhin, A. M. Balbashov and A. Loidl, *Phys. Rev. B* **70** (2), 024414 (2004).
21. K. Noda, S. Nakamura, J. Nagayama and H. Kuwahara, *Journal of Applied Physics* **97** (10), 10C103-103 (2005).
22. J. Baier, D. Meier, K. Berggold, J. Hemberger, A. Balbashov, J. A. Mydosh and T. Lorenz, *J. Magn. Magn. Mater.* **310** (2, Part 2), 1165-1167 (2007).
23. X. L. Wang, *J. Appl. Phys.* **107** (9), 09B510 (2010).
24. M. W. Kim and et al., *New Journal of Physics* **6** (1), 156 (2004).
25. M. W. Kim, S. J. Moon, J. H. Jung, J. Yu, S. Parashar, P. Murugavel, J. H. Lee and T. W. Noh, *Physical Review Letters* **96** (24), 247205 (2006).

26. M. Bastjan, S. G. Singer, G. Neuber, S. Eller, N. Aliouane, D. N. Argyriou, S. L. Cooper and M. Rübhausen, *Phys. Rev. B* **77** (19), 193105 (2008).
27. K. van Benthem, *J. Appl. Phys.* **90** (12), 6156 (2001).
28. M. A. Geday and A. M. Glazer, *Journal of Physics: Condensed Matter* **16** (20), 3303 (2004).
29. A. M. Haghiri-Gosnet and J. P. Renard, *Journal of Physics D: Applied Physics* **36** (8), R127 (2003).
30. D. Pesquera, V. Skumryev, F. Sánchez, G. Herranz and J. Fontcuberta, *Phys. Rev. B* **84** (18), 184412 (2011).

Chapter 6

Strontium Titanate STO Substrates

6.1 Introduction

STO was the substrate chosen for growing LSMO and GdMnO₃ films as it was expected to be a low-strain substrate. However, the films grown on substrates of this material showed anomalous magneto-optical behaviour as was discussed in chapters 4 and 5. The present chapter will provide an investigation of the optical and magneto-optical properties of a STO substrate in order to understand the earlier result. The influence of birefringence on the magneto-optical data obtained using the Sato method is discussed.

6.2 Literature on Optical and Magneto-Optical Properties of STO Substrates

A large number of materials have great potential for possible industrial applications. These applications require that the material be grown in thin-film form rather than in the bulk. In recent years, many research groups have studied the difference between the properties of thin films and bulk materials. The thin films have been grown to optimise the structural and physical properties. It is found that some properties, such as structural deformation and magnetic/optical anisotropy, are strongly dependent on the nature of the substrate [1-5]. Such results could often be attributed to the stress induced by the lattice mismatch between film and substrate [3, 5]. In particular, a cubic substrate, such as STO, commonly induces either a compressive or a tensile bi-axial strain on the growing film [6]. STO is probably the

most commonly used substrate for growing epitaxial thin manganites films, as it is one of the more important oxide materials for potential device applications [6-7]. However, STO substrates display birefringence which, in turn, has an effect on the optical and magneto-optical properties. The ray of light that passes through a birefringent material is split into two unequal waves which propagate with different speeds. Thus, birefringent crystals have a refractive index that depends on the polarisation and propagation direction of the incident light; clearly then, it is not the same at all angles.

STO has the ABO_3 cubic perovskite structure with a lattice parameter of 0.3905 nm. In addition, STO substrates can be used at a high deposition temperature due to their high melting point of around 2080 °C [8]. In the perovskite structure, there are always two types of terminating planes. For instance, STO (001) has A (SrO) or B (TiO_2) terminating planes in the $\langle 001 \rangle$ directions see fig.6.1 where, the topmost surface of the STO is terminated by either one of these planes.

**Removed by the
author for copyright reasons**

Figure (6.1): The ABO_3 cubic perovskite crystal structure of STO and possible terminating planes of a {001} surface [8].

At room temperature, STO has a cubic perovskite structure but undergoes a phase transition to a tetragonal structure at about 105 K [6]. The TiO_6 octahedra rotate around the cubic axis, whereas the oxygen ions remain in its position in the face of the unit cell. This leads to an expansion in the c- axis direction and a contraction in the a-axis direction, which results in a tetragonal structure. This transition leads to birefringence in the STO substrate, unless the E vector of the light is directed along one of the optic axes [6, 9].

**Removed by the
author for copyright reasons**

Figure (6.2): Birefringence in STO as a function of temperature. The straight line is a fit to the observed data [9].

It was found that the birefringence (Δn) is directly proportional to the temperature [9] below the phase transition temperature, as illustrated in fig.6.2. The birefringence increased as the temperature decreased below a critical value 105K, which is the phase transition of the STO substrate.

The properties of STO can easily be changed by doping or by introducing oxygen vacancies. Hence, STO can be made n-type conducting by doping with a small fraction of La, Nb or Ta [10]. However, oxygen vacancies can be introduced into STO substrates during film deposition, which may have an effect on the properties of the film.

STO is a dielectric material with a band gap at about 3.2 eV at 300 K [10-11]. Studies of the optical properties of STO found that the absorption near the band edge was attributed to phonon-assisted indirect transition. Blazey [12] measured the wavelength-modulated absorption spectrum of STO around the structural phase transition for various temperatures; this is shown in fig. 6.3. There is a single minimum at all temperatures above and below the phase transition 105 K; this was thought to be due to an indirect transition, as it is not seen in the modulated reflection spectrum.

Zollner *et al* studied the optical properties of bulk STO with a thickness of 0.5 mm. They measured the absorption coefficient (α) and the band gap was found to be about 3.25 to 3.37 eV [13], as illustrated in fig. 6.4. This is similar to what had previously been measured, as is shown in chapter 5 fig. 5.14.

**Removed by the
author for copyright reasons**

Figure (6.3): The wavelength-modulated absorption spectrum of STO at various temperatures around the structural phase transition [12].

**Removed by the
author for copyright reasons**

Figure (6.4): The optical absorption coefficient (α) as a function of photon energy for bulk STO. The inset is $\sqrt{\alpha}$ in the region of the indirect band gap (3.2 eV). This figure was taken from [13].

6.3 Experiment Results and Discussion

In order to study the optical and magneto-optical properties of STO substrates, a (001) sample of dimensions $5\text{mm} \times 5\text{mm} \times 0.5\text{mm}$ was employed. The STO (001) substrate which was polished on both sides was purchased from PyKem.

The optical properties were measured at room temperature in the spectral range 1.5-4.5 eV using the absorption system. The magneto-optical properties were measured in the same range using Faraday geometry in applied magnetic fields up to 1.8 Tesla perpendicular to surface of the samples. The substrate was rotated with (ψ) varying from 0° to 360° relative to the polarisation of the analyser, as shown in fig.6.5.

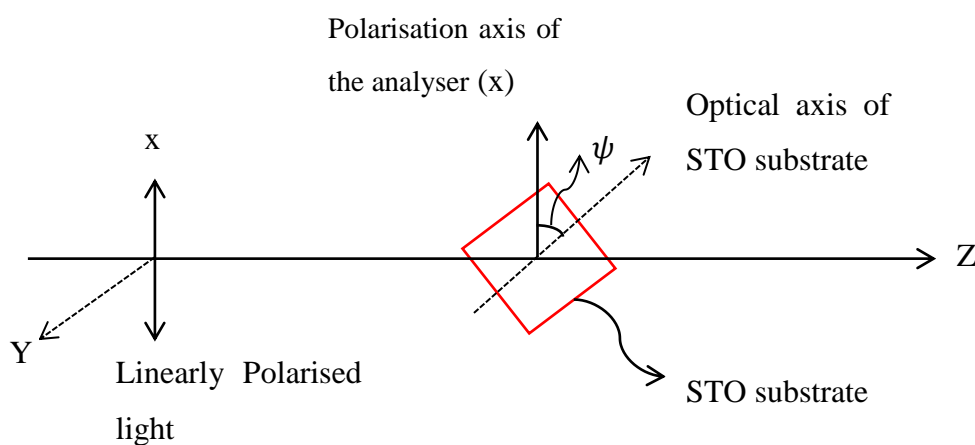


Figure 6.5: Sketch showing the set-up used for studying the magneto-optical properties of an STO substrate in Faraday geometry.

The transmission of STO has previously been measured; it has also been mentioned that STO has an indirect band gap at 3.2 eV . This was shown in fig.5.11, chapter 5. In order to study this more carefully, the derivative spectrum (dT/dE) was calculated, as shown in fig. 6.6. The derivative spectrum removes the background and amplifies the singularity. This shows that the lowest, indirect band gap for our STO substrate occurs at 3.26 eV.

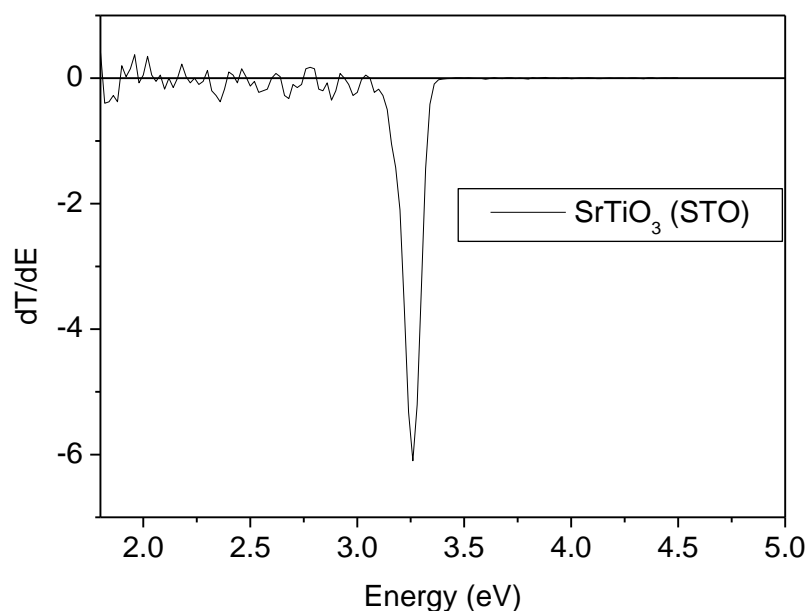


Figure (6.6): The derivative spectrum (dT/dE) versus photon energy for an STO substrate in the region of the band gap, measured at room temperature.

The magneto-optical set-up which is based upon Sato method [14] involves, a measurement of three intensities I_0 , $I_1(f)$ and $I_2(2f)$ being transmitted through the sample, as discussed in chapter 3. In the absence of any birefringence in the sample, the intensity $I_1(f)$ is proportional to the MCD and $I_2(2f)$ is proportional to the Faraday rotation (θ). However, in the presence of the birefringence, this contributes to both

$I_1(f)$ and $I_2(2f)$. With detailed and complex mathematics, the final intensities of $I_1(f)$ and $I_2(2f)$, after passing through the Sato rig, are given by:

$$\frac{I_1(f)}{I_0} = \sin\gamma \left(\frac{1}{4} \sin 4\Gamma (\theta_1 - \theta_2)^2 + 2\eta \sin 2\Gamma \right) - \cos\gamma [\sin 2\Gamma \sin(\theta_1 - \theta_2)] \quad \dots\dots\dots 6.1$$

$$\frac{I_2(2f)}{I_0} = \cos\gamma \left(\frac{1}{4} \sin 4\Gamma (\theta_1 - \theta_2)^2 + 2\eta \sin 2\Gamma \right) + \sin\gamma [\sin 2\Gamma \sin(\theta_1 - \theta_2)] \quad \dots\dots\dots 6.2$$

The derivation plus further details are given in Appendix A. The term (2η) is the true ellipticity, $(\theta_1 - \theta_2)$ is the rotation, Γ is the ellipticity and γ is the sense of rotation; γ is the only parameter that changes sign with magnetic field. The measurement can be taken both in magnetic field (H) and in zero field. In the case of measurements made in a field, the difference between the measurements for $+H$ and $-H$ is taken and only terms in $\sin\gamma$ remain:

$$\frac{I_1(f)}{I_0} = \sin\gamma \left(\frac{1}{4} \sin 4\Gamma (\theta_1 - \theta_2)^2 + 2\eta \sin 2\Gamma \right) \quad 6.3$$

$$\frac{I_2(2f)}{I_0} = \sin\gamma [\sin 2\Gamma \sin(\theta_1 - \theta_2)] \sim \sin\gamma [\sin 2\Gamma (\theta_1 - \theta_2)] \quad 6.4$$

From equations (6.3) and (6.4) there is a term varying like the $\frac{I_2(2f)}{I_0}$ squared in the $\frac{I_1(f)}{I_0}$ unless $\Gamma = \frac{\pi}{4}$. The aim is to eliminate this term in order to find $\frac{I_1(f)}{I_0}$, where (2η) is the true $\frac{I_1(f)}{I_0}$ signal.

The spectra of $I_1(f)/I_0$ and $I_2(2f)/I_0$ for the STO substrate were measured in-field at different orientations (ψ) of the STO substrate relative to the polarisation of

the analyser. Fig.6.7 shows the $I_1(f)/I_0$ spectrum of the STO substrate at different orientations, measured at room temperature in a field of 1.8 T. The data shows two features: one at the band edge and a negative feature at the lower energy. This indicates that, below the band gap, the $I_1(f)/I_0$ spectrum varied with the applied magnetic field and is orientation dependent. The dependence of $I_1(f)/I_0$ on orientation appears to be due to the magnetically induced birefringence in the substrate. Now we need to find the orientation of the substrate which gives the lowest birefringence.

The magnitude of $I_1(f)/I_0$ and $I_2(2f)/I_0$ were plotted as a function of orientation, as shown in fig. 6.8 and fig.6.9. The data indicates that the birefringence in the substrate was enhanced by a magnetic field, which is surprising and unexpected. Moreover, the data is reproducible and non-periodic as expected. The relation between the birefringence (Δ) and the orientation angle (ψ) are given as:

$$\tan\Gamma = \frac{\sqrt{\Delta^2 + 4\varepsilon'_{xy}{}^2 - \Delta \cos 2\psi}}{\sqrt{\Delta^2 \sin^2 2\psi + 4\varepsilon'_{xy}{}^2}} \quad 6.4$$

The derivation and further details are given in Appendix A. The magnetism is included in the term ε'_{xy} . If $\varepsilon'_{xy} = 0$ or when the birefringence dominated we found:

$$\tan\Gamma = \tan\psi \quad 6.5$$

$I_1(f)/I_0$ is proportional to $\sin 2\Gamma$ or $\sin 2\psi$. This vanishes ($\sin 2\psi = 0$) if ψ or Γ are such that: $\Gamma = \psi = 0, \frac{\pi}{2}, \pi, \frac{3\pi}{2}, \dots$

However, the data shown in fig.6.8 did not exhibit a periodic variation with 180° , which is surprising. By looking to the case at when the birefringence (Δ) is zero, and from equation 6.4 it is found that:

$$\tan\Gamma = \frac{2\varepsilon'_{xy}}{2\varepsilon'_{xy}}=1 \quad \text{and} \quad \Gamma = \frac{\pi}{4} = \psi \quad 6.6$$

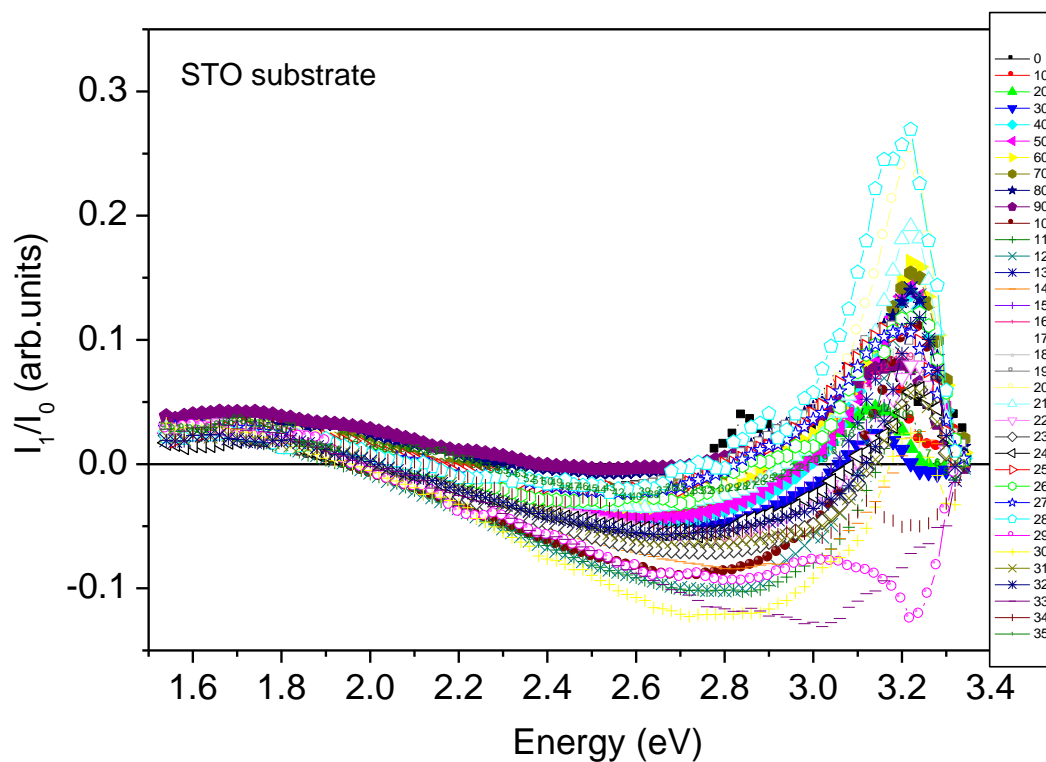


Figure (6.7): Room temperature $I_1(f)/I_0$ spectra for STO substrate at different orientation measured in 1.8 T.

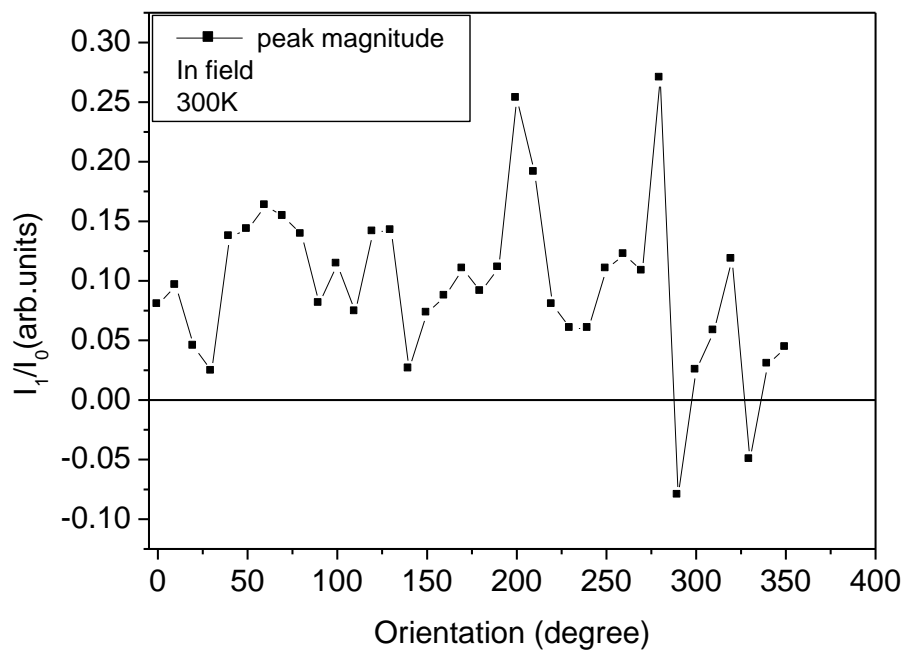


Figure (6.8): $I_1(f)/I_0$ values at room temperature taken around the band edge versus the orientation of an STO substrate. The data was measured in 1.8 T.

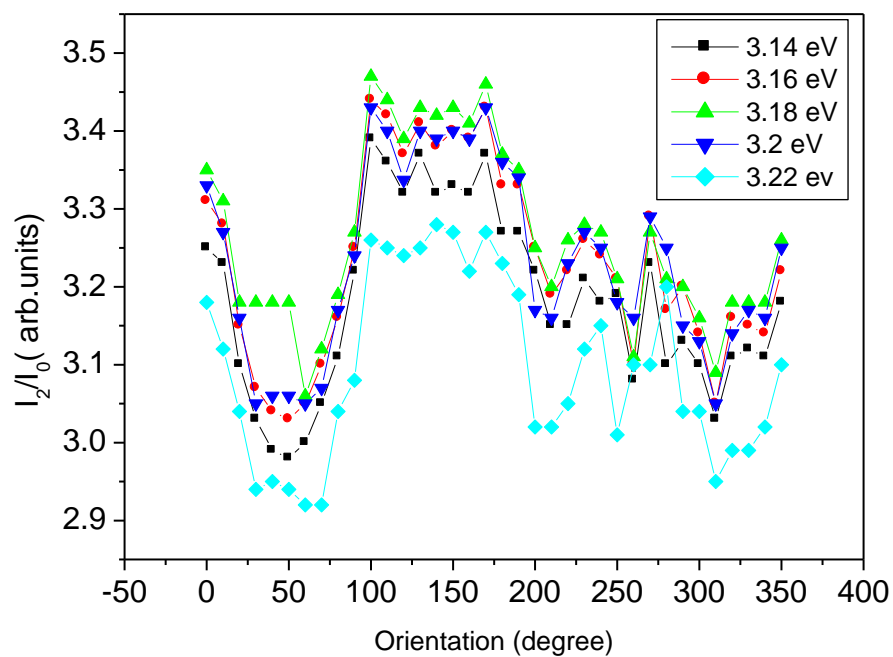


Figure (6.9): $I_2(2f)/I_0$ values at room temperature taken at different photon energy versus the orientation of STO substrate. The data was measured in 1.8 T.

In order to study the temperature dependence of the birefringence, the substrate was rotated by 45° to give a low birefringence, as was expected; then the $I_1(f)/I_0$ spectra were measured as a function of temperature, as shown in fig.6. 10. It is clear that the STO substrate has a signal of $I_1(f)/I_0$ at the structural transition, around 100 K. The magnitude of $I_1(f)/I_0$ is strongly temperature dependent and decrease with decrease of temperature below 100 K, as shown in fig.6.11. This is due to the birefringence of the STO, which is linearly temperature dependent and increases with decrease of temperature. The birefringence vanishes at about 100 K, as was reported previously (fig. 6.2). This indicates that the birefringence contributes to the $I_1(f)/I_0$ signal where $I_1(f)/I_0$ has a maximum value for a minimum value of the birefringence

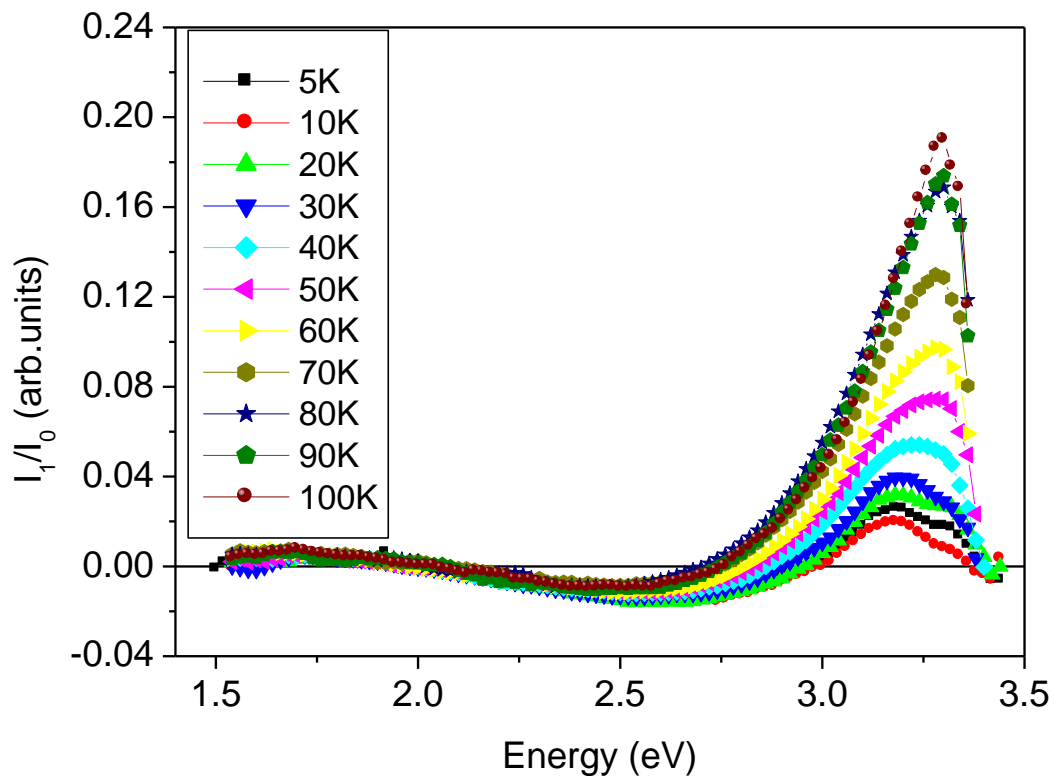


Figure (6.10): Temperature dependence of $I_1(f)/I_0$ for STO substrate measured in 0.5 T. The data were measured at an angle of 45° between the STO substrate optical axis and the polarisation axis of the analyser.

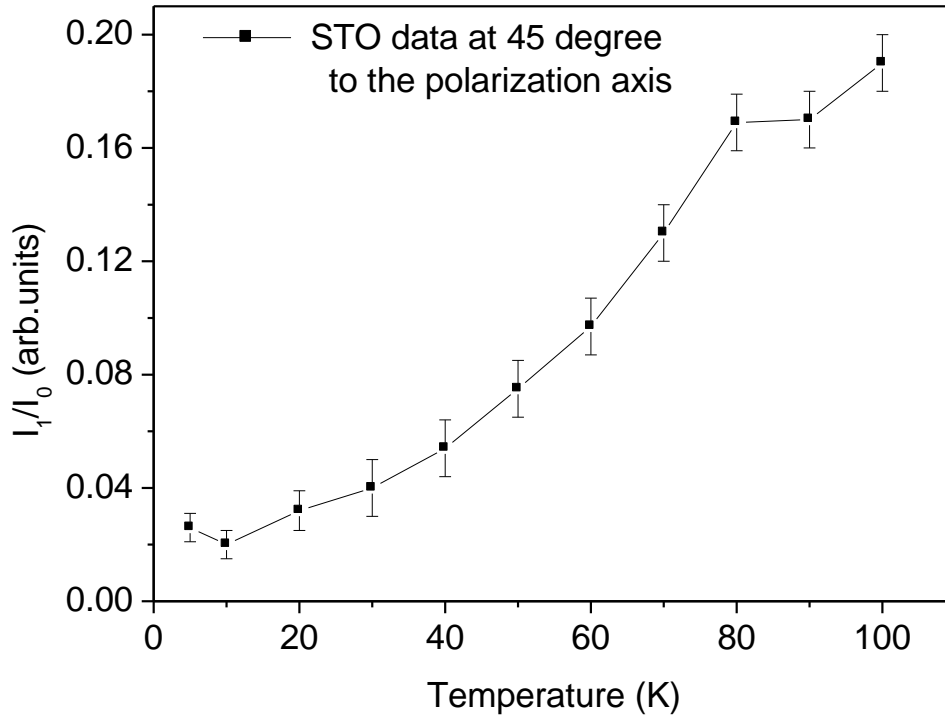


Figure (6.11): Magnitude of $I_1(f)/I_0$ for SrTiO₃ (STO) substrate as a function of temperature taken at 0.5 T. The data was measured at 45° between the STO substrate optical axis and the polarisation axis of the analyser.

It is clear from fig.6.11 that, below the phase transition temperature (100 K) of the STO, the $I_1(f)/I_0$ signal is temperature dependent. However, the birefringence is also temperature dependent and decreased linearly as the temperature was increased. This indicates that the birefringence has a strongly influence on the $I_1(f)/I_0$ data and dominates below the temperature of the phase transition. The birefringence values were expected to vary with temperature as follows:

$$\Delta = \Delta_0 \frac{(T_D - T)}{T_D} \quad 6.7$$

Where, Δ_0 is the initial birefringence and T_D is the distortion temperature (phase transition temperature). The signal of $\frac{I_1(f)}{I_0}$ is found to be proportional to $\sin \gamma$, which is given by:

$$\sin \gamma = \frac{2\varepsilon'_{xy}}{\sqrt{\Delta^2 \sin^2 2\psi + 4\varepsilon'^2_{xy}}} \quad 6.8$$

And at $\psi = \frac{\pi}{4}$ we found that

$$\sin \gamma = \frac{2\varepsilon'_{xy}}{\sqrt{\Delta^2 + 4\varepsilon'^2_{xy}}} \quad 6.9$$

When $\Delta^2 \gg \varepsilon'^2_{xy}$, from equation (6.7) and by using equation (6.9) we obtain:

$$\sin \gamma = \frac{a}{\sqrt{b^2(T_D - T)^2 + a^2}} \quad \text{where, } a = 2\varepsilon'_{xy} \quad \text{and } b = \frac{\Delta_0}{T_D} \quad 6.10$$

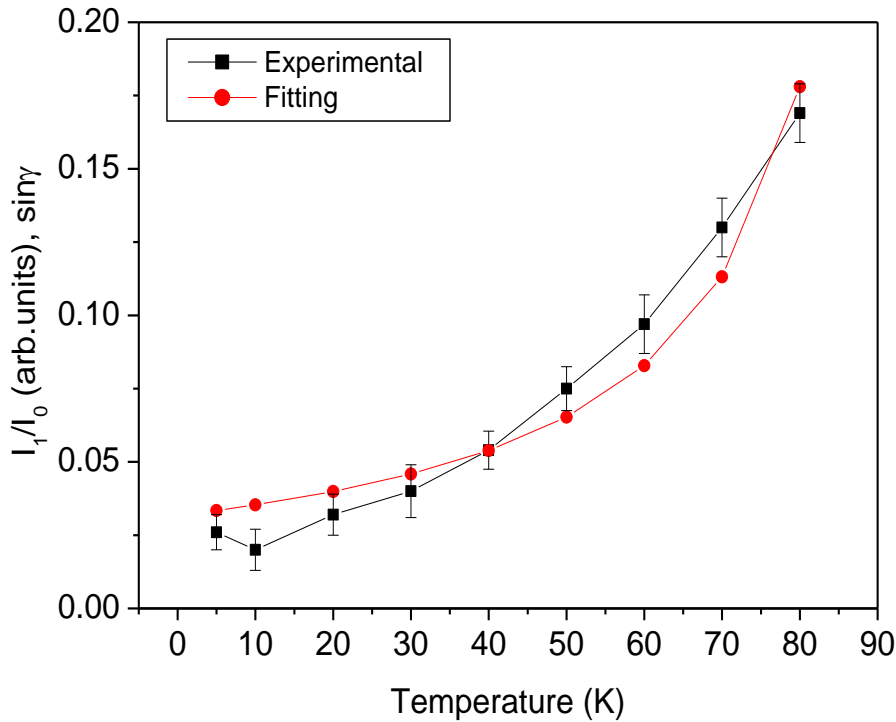


Figure (6.12): The fitting of the experimental data of $(I_1(f)/I_0)$ signal of STO substrate to the equation (6.7). The data was measured at an angle of 45° between the substrate optical axis and the polarisation axis of the analyser.

Fig.6.12 shows the fitting of equation (6.10) to the experimental data of $\frac{I_1(f)}{I_0}$ signal of a STO substrate measured at an angle of 45° between the optical axis of STO substrate and the polarisation axis of the analyser. The experimental data follow to some extent the equation (6.10) and the fitting parameters are: $a= 0.38\pm 0.02$, $b= 0.098\pm 0.005$ and $T_D=97\pm 6$ K. The fitting parameters were used in equation (6.7) to estimate the birefringence values of STO substrate as a function of temperature, as is shown in fig.6.13.

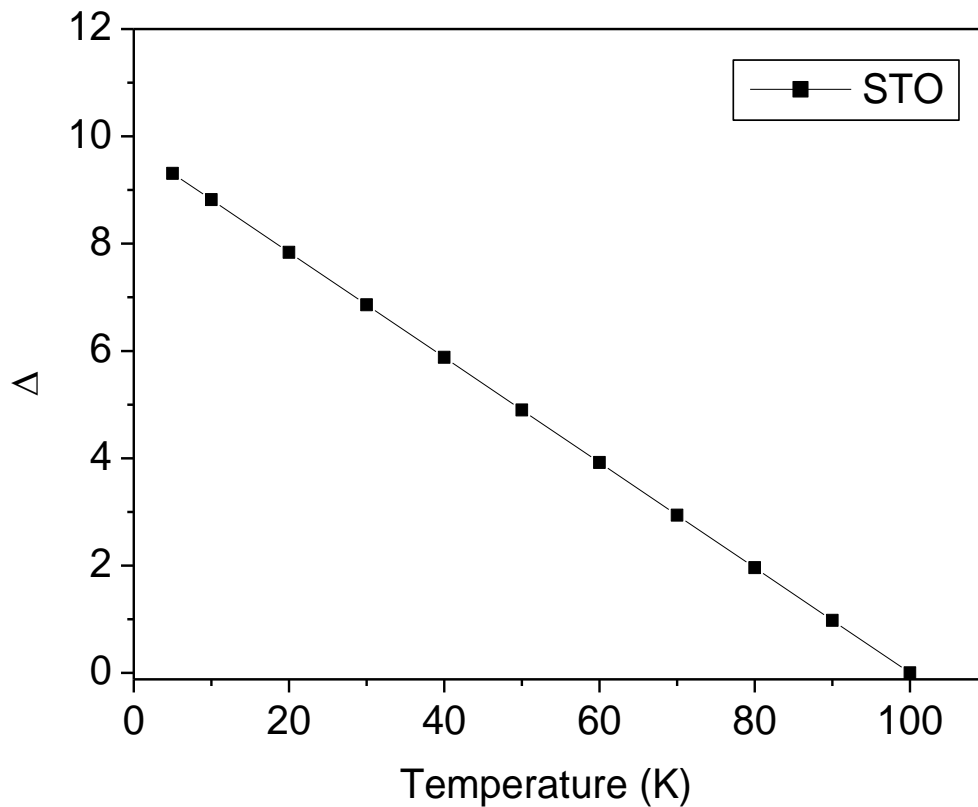


Figure (6.13): The birefringence (Δ) of an STO substrate as a function of temperature.

In the case of measurements taken in zero field; there is no correction for $+H$ and $-H$ and $\sin \gamma = 0$ and $\cos \gamma = 1$. Thus, the $\frac{I_1(f)}{I_0}$ and $\frac{I_2(2f)}{I_0}$ signals should be interchanged and given as:

$$\frac{I_1(f)}{I_0} = \sin 2\Gamma \sin(\theta_1 - \theta_2) \sim \sin 2\Gamma (\theta_1 - \theta_2) \quad 6.11$$

$$\frac{I_2(2f)}{I_0} = \frac{1}{4} \sin 4\Gamma (\theta_1 - \theta_2)^2 + 2\eta \sin 2\Gamma \quad 6.12$$

Fig. 6.14 and 6.15 show the spectra measured in zero field for $I_1(f)/I_0$ and $I_2(2f)/I_0$ respectively. This result shows that the spectrum depended on angle for both $I_1(f)/I_0$ and $I_2(2f)/I_0$. This result is evidence for a birefringent contribution from the STO substrate in zero field. However these data do not agree with the expected results from equations 6.11 and 6.112.

Finally, we can conclude that the birefringence in the STO substrate is both field and temperature dependent, which makes the behaviour of the birefringence very complicated.

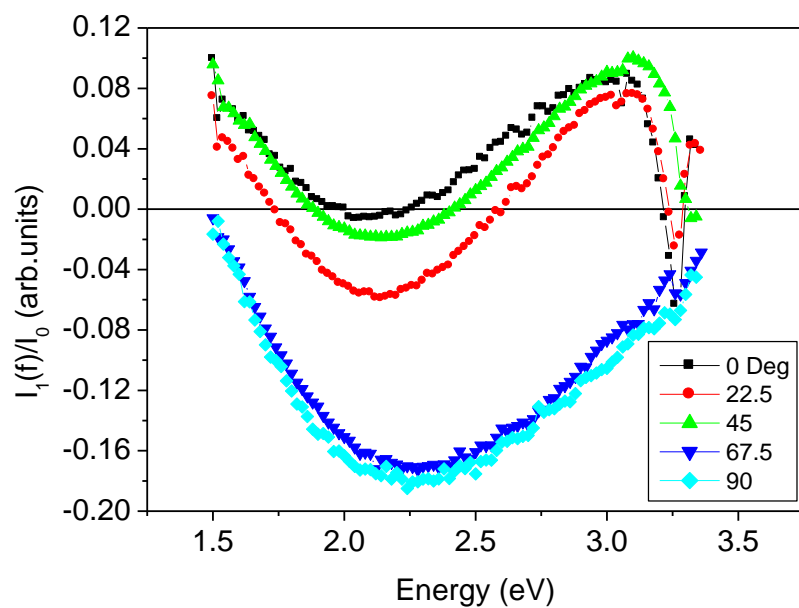


Figure (6.14): Room temperature $I_1(f)/I_0$ spectra for STO substrate at different orientations and measured in zero field.

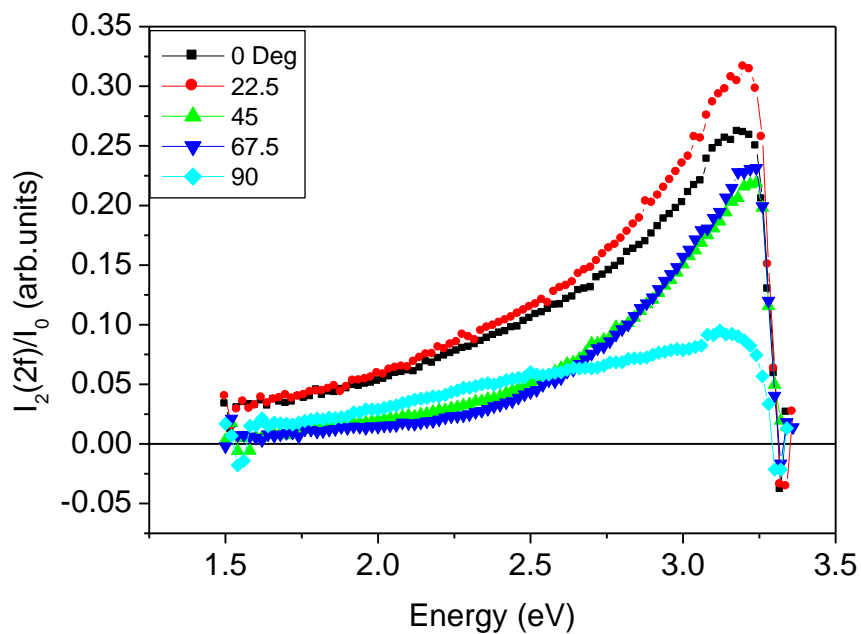


Figure (6.15): Room temperature $I_2(2f)/I_0$ spectra for STO substrate at different orientations and measured in zero field.

6.4 Summary and Conclusions

This chapter reported the investigation of the derivative spectrum and the magneto-optical properties of an STO substrate. We have also discussed the influence of birefringence on the magneto-optics of the substrate obtained using the Sato method.

The derivative spectrum data shows that the lowest indirect band gap for the STO substrate occurs at 3.26 eV. The MCD peak appears at a slightly lower value than that seen in the energy modulated experiment; this could be due to the different thicknesses. The data indicated that the substrate has circular dichroism (MCD) below the band gap, which is strongly temperature dependent and varies linearly with applied magnetic field. The data indicates that the magnetic field enhanced the birefringence in the STO substrate and the birefringence is both orientation and temperature dependent.

Overall, STO substrate were used to grow LSMO and GdMnO₃ thin films and did have an anomalous magneto-optical data, as discussed in chapters 4 and 5. In order to avoid the birefringence, the optical and magneto-optical properties of the substrate were studied. It seems that the relation between the birefringence on the one hand and the magnetic field, orientation and temperature on the other hand is very complex. It is difficult to determine the value of the birefringence and correct the data of the films grown on an STO substrate.

In summary, we do not recommend using STO substrate for the growth of films for optical study for $E \geq 2.4 \text{ eV}$.

6.5 References

1. R. Desfeux, S. Bailleul, A. Da Costa, W. Prellier and A. M. Haghiri-Gosnet, *Applied Physics Letters* **78** (23), 3681-3683 (2001).
2. A. M. Haghiri-Gosnet, J. Wolfman, B. Mercey, C. Simon, P. Lecoeur, M. Korzenski, M. Hervieu, R. Desfeux and G. Baldinozzi, *Journal of Applied Physics* **88** (7), 4257-4264 (2000).
3. C. Kwon, M. C. Robson, K. C. Kim, J. Y. Gu, S. E. Lofland, S. M. Bhagat, Z. Trajanovic, M. Rajeswari, T. Venkatesan, A. R. Kratz, R. D. Gomez and R. Ramesh, *Journal of Magnetism and Magnetic Materials* **172** (3), 229-236 (1997).
4. W. Prellier, M. Rajeswari, T. Venkatesan and R. L. Greene, *Applied Physics Letters* **75** (10), 1446-1448 (1999).
5. J. Z. Sun, D. W. Abraham, R. A. Rao and C. B. Eom, *Applied Physics Letters* **74** (20), 3017-3019 (1999).
6. D. Pesquera, V. Skumryev, F. Sánchez, G. Herranz and J. Fontcuberta, *Physical Review B* **84** (18), 184412 (2011).
7. C. H. Jia, Y. H. Chen, G. H. Liu, X. L. Liu, S. Y. Yang and Z. G. Wang, *Journal of Physics D: Applied Physics* **42** (1), 015415 (2009).
8. G. Koster, G. Rijnders, D. H. A. Blank and H. Rogalla, *Physica C: Superconductivity* **339** (4), 215-230 (2000).
9. M. A. Geday and A. M. Glazer, *Journal of Physics: Condensed Matter* **16** (20), 3303 (2004).
10. A. Kalabukhov, R. Gunnarsson, J. Börjesson, E. Olsson, T. Claeson and D. Winkler, *Physical Review B* **75** (12), 121404 (2007).

11. M. L. Scullin, J. Ravichandran, C. Yu, M. Huijben, J. Seidel, A. Majumdar and R. Ramesh, *Acta Materialia* **58** (2), 457-463 (2010).
12. K. W. Blazey, *Physical Review Letters* **27** (3), 146-148 (1971).
13. S. Zollner, A. A. Demkov, R. Liu, P. L. Fejes, R. B. Gregory, P. Alluri, J. A. Curless, Z. Yu, J. Ramdani, R. Droopad, T. E. Tiwald, J. N. Hilfiker and J. A. Woollam, *J. Vac. Sci. Technol. B* **18** (4), 2242-2254 (2000).
14. K. Sato, *Japanese Journal of Applied Physics* **20** (12), 2403-2409 (1981).

Chapter 7

Transition Metal (TM) Doped In₂O₃

7.1 Introduction

Transition metal (TM)-doped semiconductor oxides are promising material to show ferromagnetism above room temperature. This chapter reports an investigation of the magnetic and magneto optical properties of Fe and Co doped indium Oxide (In₂O₃). It also provides a simple method to determine the contribution from the TM to the ferromagnetic moment of the films. The Co-doped In₂O₃ data presented in this chapter was published in [1].

7.2 Literature Review on TM Doped In₂O₃

Many oxide semiconductors such as ZnO, SnO₂, In₂O₃, and TiO₂ doped with transition metal TM have been reported to be a ferromagnetic FM beyond room temperature [2, 4-11]. Recently, a number of research groups have conducted thorough studies of high ferromagnetism FM in a number of TM doped-In₂O₃ systems. The room temperature ferromagnetism has been reported for all 3d TM such as (V, Cr, Fe, Cu, Ni and Co) [3, 12-25]. In₂O₃ crystallizes in the cubic structure with lattice constant about $a=10.12 \text{ \AA}$ with 80 atoms or 16 formula units per unit cell [14]. This gives In₂O₃ an advantage as a host material because it can be grown on low cost substrates such as MgO and Al₂O₃ [13, 26]. In₂O₃ is a wide band-gap semiconductor (3.75 eV) and is transparent in the visible [4, 24, 27]. It can be prepared as an n-type semiconductor with a high electrical conductivity by introducing oxygen deficiencies

or by Sn doping (ITO) [12, 14]. Sn-doped In₂O₃ with 10% produces transparent n-type conducting semiconductor which can be widely used in device applications. It is widely used in semiconductor devices such as optoelectronics and photovoltaics [28-29]. This has shown a high carrier concentration at about 10^{20} - 10^{21} electrons/cm³ with high mobility at about (10- 100) cm².V⁻¹.s⁻¹ [16, 26, 30].

Recently, room temperature (RT) ferromagnetism has been reported for Co-doped indium oxide (ITO) [31]. This ferromagnetism behaviour has found to be correlated to the transport properties. Moreover, metallic Co clusters have been observed in many cases of thin films but the high-temperature annealing remove these nanoclusters [12, 31].

The origin of ferromagnetism remains unclear although the ferromagnetism properties are strongly affected by many parameters such as growth, annealing processes, defects and substrate nature [12, 16, 31]. However, the origin of the ferromagnetism in TM doped oxides semiconductors was thought to be due the interaction between the s and p band of the host and the localized 3d electrons in TM band [1, 32], whereas, other researchers have reported that the TM ions are paramagnetic [32-33]. Several groups have looked hard for evidence of ferromagnetic behaviour using local probes, X-ray magnetic circular dichroism (XMCD) or Mossbauer effect. A Brillouin function has been fitted to the M(H) curves of Co doped ZnO recorded from XMCD using a magnetic moment of $4.8 \mu_B/\text{Co}$ which is related to Co⁺² [34-35]. The analysis of Mossbauer spectroscopy of Fe doped ITO showed a paramagnetic pattern for Fe⁺² and Fe⁺³ [2]. In all cases they have found that the TM ions themselves have a magnetization that varies as H/T which means purely paramagnetic behaviour of TM. Coey has analysed the susceptibility of a strongly magnetic sample at low temperature and found for Mn in ITO that the susceptibility

varied as C/T where the Curie constant C was exactly what would be predicted for Mn^{+2} [2] as illustrated in fig.7.1. Similar result was found for Co^{+2} doped ITO [32] and $Zn_{1-x}Co_xO$ [34-35]. Moreover, some research groups have reported that the films of In_2O_3 with TM^{2+} are ferromagnetic whereas all those relating to solely TM^{3+} are not ferromagnetic [36-37]. On the other hand mixed valence of TM^{2+}/TM^{3+} is reported to be origin of the magnetism [38] whereas there is good evidence that actually the TM ions are not ferromagnetic.

**Removed by the
author for copyright reasons**

Figure (7.1): Magnetisation curves at different temperature for 5% Mn-doped ITO films. The inset is the Curie-law behaviour [2].

The recent research focuses on investigating the link between the defects and the ferromagnetism (FM). Oxygen vacancies are believed to be a critical role to explain the ferromagnetism in oxide semiconductors. It is strongly believed that the existence of oxygen vacancies in TM doped In_2O_3 plays a critical role in enhancing

the ferromagnetism. Xiao-Hong *et.al* reported the decrease of magnetisation with the increase of oxygen pressure for Fe-doped In₂O₃ films as shown in fig. 7.2 [3].

**Removed by the
author for copyright reasons**

Figure (7.2): Room temperature magnetisation for (In_{0.98} Fe_{0.02})₂O₃ films grown at various oxygen pressures. Adopted from ref. [3]. Inset is the variation in the M_S as a function of oxygen pressure.

Fe-doped In₂O₃ has particularly acquired a significant amount of interest due to the high solubility, up to 20%, of Fe in the In₂O₃ matrix; this makes it an effective system for application in spintronic devices and also for studying the physics that underpins DMSs. However, the growth method and processing conditions are crucial for the magnetic properties of Fe-doped In₂O₃. Room temperature ferromagnetism has been reported in Fe- doped In₂O₃ bulk and thin films [20, 23, 38]. Very recently, room temperature ferromagnetism has been reported in Fe-doped In₂O₃ thin films and others attributed the ferromagnetism to the spin-polarised carriers [11].

Cobalt (Co) is one of the TMs that shows high magnetisation. Room temperature ferromagnetism has been reported in Co doped In₂O₃ and indium-tin oxide (ITO) [30, 39]. Others attributed the ferromagnetism to different contributions from oxidized (Co²⁺) and from metallic cobalt (Co⁰). It was found in indium-tin oxide films the Co atoms substitute homogeneously the indium (In) sites with less than 7% of Co [19].

As far as is known, there is no published research on magneto-optical properties of TM-doped In₂O₃ except our papers [1, 4]. However, there are number of magneto-optical studies on dilute magnetic oxide materials (DMO) such as ZnO. These studies have provided very useful information about the spin polarisation in conduction electrons [40-42].

7.3 Experiment Results and Discussion:

7.3.1 Co Doped In₂O₃

In order to study the magnetic and magneto-optical properties of Co-doped In₂O₃, five thin films of (In_{1-x} Co_x)₂ O₃ with normal Co concentration of 1-5% were grown by A. Hakimi in the laboratory of Cambridge University using dc magnetron sputtering. The Co concentration were measured using an energy dispersive x-ray spectroscopy (EDX) and the actual value were 1.6, 3.1, 4.7 .6.4 and 8.1 %. The films thickness was 200 nm grown in a highly oxygen-deficient environment on (0001) C-plane sapphire substrate at 300 °C. The data presented in this section was published in [1].

Fig.7.3 shows XRD patterns of Co-doped In₂O₃ films performed by A. Hakimi in Cambridge University. XRD patterns shows a relatively sharp peak and no detectable peak corresponds to the secondary phases of Co metal or Co oxides. This indicates that the films are pure phases and have high crystalline quality. With an increase of Co doping levels, the In₂O₃ (222) and (400) peaks was found to be shifted toward higher values of 2θ . This is evidence that the Co²⁺ ions with smaller ionic radius (0.74 Å) substitute for In³⁺ with larger ionic radius (0.94 Å) rather than forming a defect phase. Fig.7.4 shows the near-edge EXAFS data for the (In_{0.919} Co_{0.081})₂ O₃ film compared with CoO and Co metal performed by S.M. Heald in Argonne National laboratory, USA. The EXAFS spectra indicate that Co is predominately Co²⁺. However, the small peak at about 7710 eV could be attributed to a small amount of Co metal.

**Removed by the
author for copyright reasons**

Figure (7.3): XRD data for (In_{1-x} Co_x)₂ O₃ films demonstrate the shift in the peak position upon Co doping. The inset is the steady decrease in the average lattice parameter $\langle a \rangle$ as a function of Co doping [1]

**Removed by the
author for copyright reasons**

Figure (7.4): Normalized Co near-edge EXAFS spectra for the 8.1% Co-doped In₂O₃ thin film compared with CoO and Co metal [1].

Magnetic properties were investigated using the superconducting quantum device (SQUID) magnetometer. Fig.7.5 shows the magnetisation raw data of $(\text{In}_{1-x}\text{Co}_x)_2\text{O}_3$ films measured under in-plane magnetic field up to 1 T and in the temperature range of 5-300 K. This data displays clear evidence for ferromagnetism in each of the Co-doped In_2O_3 films up to and above room temperature.

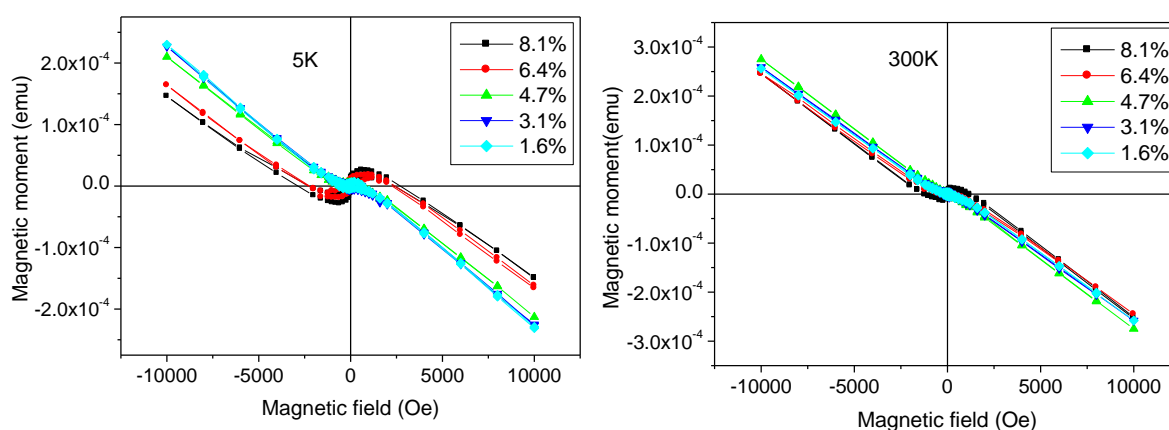


Figure (7.5): The raw magnetisation data for $(\text{In}_{1-x}\text{Co}_x)_2\text{O}_3$ thin films measured at a) 5K b) 300K.

The raw magnetisation data was decomposed into two parts. The first varies linearly with the magnetic field in the range of (0.5 -1 T) and the second is a hysteresis loop as shown in fig.7.5. The paramagnetic susceptibility (χ) is worked out from the slope of the linear part, then the curie constant C_{meas} was calculated. Since the susceptibility (χ) of the substrate is temperature independent and since the paramagnetic susceptibility (χ) at 300 K is expected to be very small, we can estimate the paramagnetic contribution of the films at 5 K from $\chi_{\text{film}}(5\text{ K}) = \chi_{\text{meas}}(5\text{ K}) - \chi_{\text{meas}}(300\text{ K})$. The susceptibility (χ) at 5K for these films has been set as $C/5$ then evaluated Curie constant (C) for the concentration of TM ions. The expected

paramagnetic susceptibility (χ) from the TM ions was calculated using

$$\chi = \frac{N x p_{\text{eff}}^2 \mu_B^2 \mu_0}{3K_B T}$$
 where p_{eff} is the effective number of Bohr magnetons (μ_B), N is the

number of host ions per cm³ and x is the TM concentration. Fig.7.6 represents the susceptibility (χ) per volume at 5 K for (In_{1-x} Co_x)₂O₃ thin films. In octahedral coordination the expected moment for Co²⁺ is $p_{\text{eff}} = 5$ but we took only the spin value of $p = 3.87$ which is for the low symmetry that is give fully quench of the orbital contribution. This is in agreement with EXAFS data that indicates that a high fraction of the Co ions are in sites of low symmetry. The measurement of paramagnetic susceptibility (χ) for these films gives compelling evidence that the Co²⁺ ions for these films do not contribute to the ferromagnetic moment because all of the Co²⁺ ions are paramagnetic. A similar conclusion was reported previously for the Mn and Co ions in indium tin Oxide (ITO) [2, 32].

**Removed by the
author for copyright reasons**

Figure (7.6): The susceptibility (χ) per volume at 5 K for (In_{1-x} Co_x)₂O₃ thin films versus the Co concentration, compared with expected susceptibility of paramagnetic Co²⁺ ions in octahedral coordination [1].

The film with 8.1 % Co shows the largest magnetisation as illustrated in the hysteresis loops shown in fig.7.7 after the contribution from the substrate has been subtracted. The saturation magnetisation increased as the temperature is lowered which is typical for semiconducting behaviour. Hence the conductivity fell rapidly at low temperature [4, 43].

**Removed by the
author for copyright reasons**

Figure (7.7): Ferromagnetic hysteresis loops for an 8.1% Co-doped In₂O₃ thin film measured at 5K and 300K [1].

The values of the saturation magnetisation and coercive fields measured at 300K and 5K for (In_{1-x}Co_x)₂O₃ films and for pure In₂O₃ are shown in the Table (7.1). The magnetisation per Co ion at room temperature is $0.38 \mu_B/Co$ and $0.83 \mu_B/Co$ for the film with Co concentration of 8.1% and 1.6% respectively and the magnetisation at low temperature is $0.61 \mu_B/Co$ and $1.4 \mu_B/Co$. This indicates that the magnetism of these films is not due to the clustering where the fraction of the

clusters and then the magnetisation increases as the Co concentration increased. The magnetisation measured for pure indium film is consistent with zero; however the experimental limit is comparable to the magnetisation observed previously [18]. The coercive field values (H_c) are similar to those reported previously for other DMOs and are considerably smaller than those observed at low temperature if the magnetisation is dominated by metallic cobalt [44-45]. The values of $M_s(5)/M_s(300)$ indicates that the magnetisation is greatly affected by the changes in temperature, which has been observed before in semiconducting oxide films [42].

**Removed by the
author for copyright reasons**

Tale (7.1): Summary of the saturation magnetisation (M_s) and Coercive field (H_c) data for pure and Co-doped In₂O₃ thin films at 5 K and 300 K [1].

In order to provide more information about the origin of magnetism the MCD spectra were measured for these films. Fig.7.8a shows the MCD spectra of (In_{1-x}Co_x)₂O₃ films measured at 300 K and in magnetic field up to 1.8 T measured by Alshammari. The MCD data of the blank substrate has been subtracted. The MCD

spectra show a peak around the band edge at 3.28 eV for all films. However, the MCD spectra for the pure In₂O₃ is significantly lower compared with the spectra of the Co doped films. The MCD feature starts at 2.5 eV for all Co-doped In₂O₃ films, which is lower than the weak gap transitions reported at 2.9 eV [46]. This could be attributed to the transition to donor state level which could originate from oxygen vacancy states that have been calculated to lie 0.9 eV below the band edge [47]. Fig.7.8 b shows the comparison between the magnetisation at 300K and the MCD measured at 3.28 eV for the (In_{1-x}Co_x)₂O₃ films. This result shows that the MCD data follows the magnetisation, although there is no complete agreement on this matter.

**Removed by the
author for copyright reasons**

Figure (7.8): a) Room temperature MCD spectra for (In_{1-x}Co_x)₂O₃ thin films measured at 1.8 T. b) Room temperature MCD taken at 3.28 eV and saturation magnetisation (Ms) as a function of Co doping level. (The scale is chosen so that points superimpose for 8.1%) [1].

7.3.2 Fe Doped In₂O₃

In order to explore the magnetic and magneto-optical properties of TM doped In₂O₃ in more detail, two groups of Fe doped In₂O₃ thin films were prepared in two different research groups. The first group of Fe doped In₂O₃ films were prepared in the National Centre of Nanotechnology at KACST in Saudi Arabia. The second group were prepared by Xiao-Hong Xu's group in Shanxi Normal University Linfen, China. The data presented in this section has been prepared for publication.

The first group of (In_{1-x} Fe_x)₂ O₃ thin films with Fe concentration of 1-5% were grown using PLD system with laser energy of 250 mJ/pulse. The target was prepared for the PLD from high-purity In₂O₃ (99.999%) and Fe₂O₃ (99.999%) powders. The stoichiometric mixture was annealed for about 8 hours in air at 400,600 and 800 °C. After the final anneal, the powder was then pressed and sintered in air at 900 °C for 8 hours and the resultant pellet was used as a target in the PLD. The films were deposited on (0001) sapphire substrate at 600 °C and the oxygen partial pressure was 2×10^{-3} mTorr. The Fe concentration in the films were measured in KACST using (EDX) and the actual value were 0.89, 1.72, 2.99 .4.07 and 5.03 %.

The crystal structure of these films were analysed with the use of x-ray diffraction (XRD) measured by Hakimi in Cambridge University. XRD shows that the films are highly crystalline and well oriented along (222) as shown in fig.7.9. However, a very weak reflection for Fe₃O₄ was observed indicating the presence of the nanoparticles.

EXAFS measurement on 5% Fe indicates a strong contribution from Fe₃O₄ as illustrated in fig.7.10. This measurement was carried out by S.M. Heald at the Advanced Photon Source in the Argonne National Laboratory, USA.

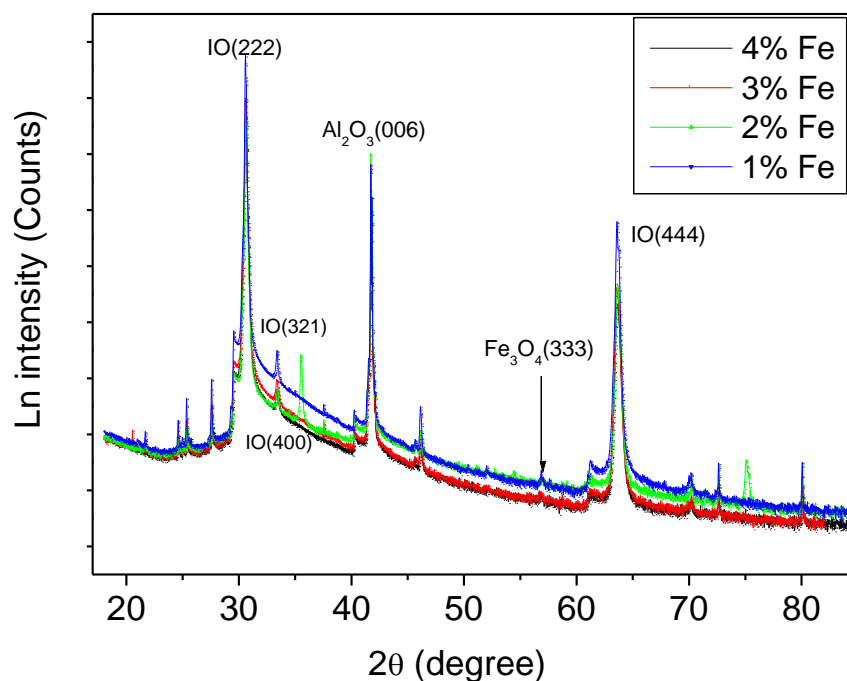


Figure (7.9): XRD data for $(\text{In}_{1-x}\text{Fe}_x)_2\text{O}_3$ thin film, demonstrate the present of Fe_3O_4 nanoparticles in the films.

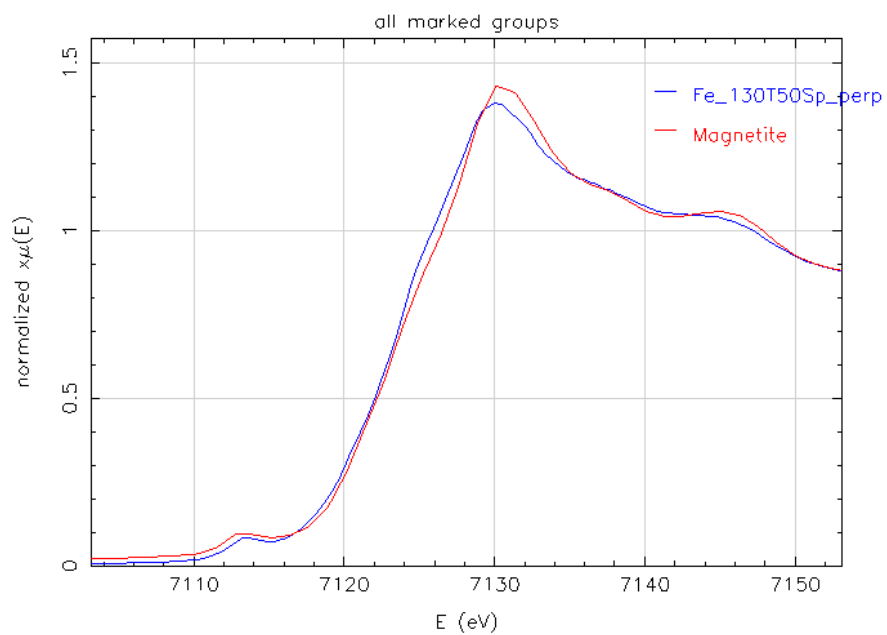


Figure (7.10): Normalized Fe near-edge EXAFS spectra for the 4% Fe-doped In_2O_3 thin film compared with Fe_3O_4 .

The Magnetic properties were investigated using the SQUID magnetometer. Fig.7.11 shows the hysteresis loops of $(\text{In}_{1-x}\text{Fe}_x)_2\text{O}_3$ thin films measured in-plane magnetic field up to 1T and in the temperature range of 5-300 K. This data shows that all films exhibited a ferromagnetic behaviour at room temperature which could be attributed to the existence of Fe_3O_4 nanoparticles. The magnetisation increases with increased of Fe concentration and in agreement with the magnetisation expected from nano-inclusion of Fe_3O_4 as illustrated in fig.7.12. This indicates that the magnetisation is due to Fe_3O_4 nanoparticles where the fraction of Fe_3O_4 nanoparticles increases with an increase in Fe content. However, there is an additional contribution to the magnetisation from other sources in the 4% and 5% Fe films as the saturation magnetisation emerges so differently.

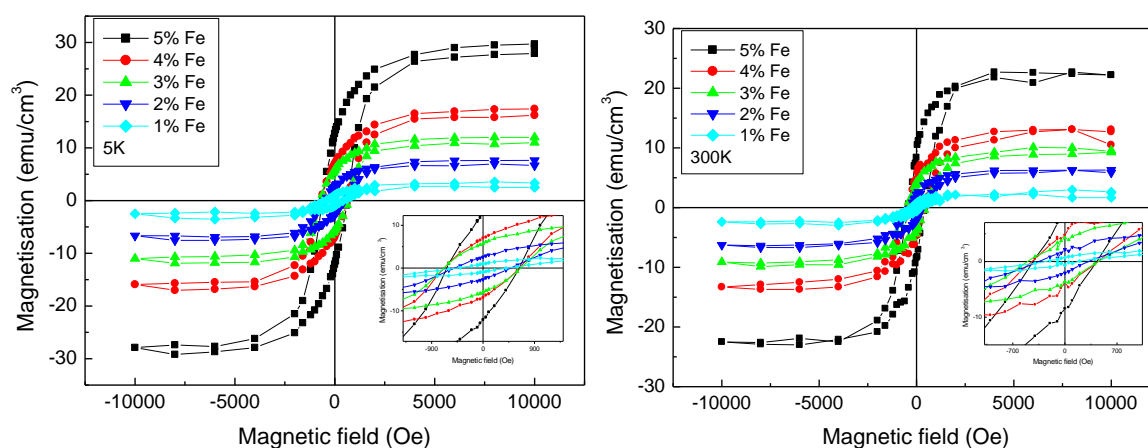


Figure (7.11): Ferromagnetic hysteresis loops of $(\text{In}_{1-x}\text{Fe}_x)_2\text{O}_3$ thin films measured at a) 5 K and b) 300 K. The diamagnetic contribution from the substrate has been subtracted). The Insets show the blow-up of the region around the origin.

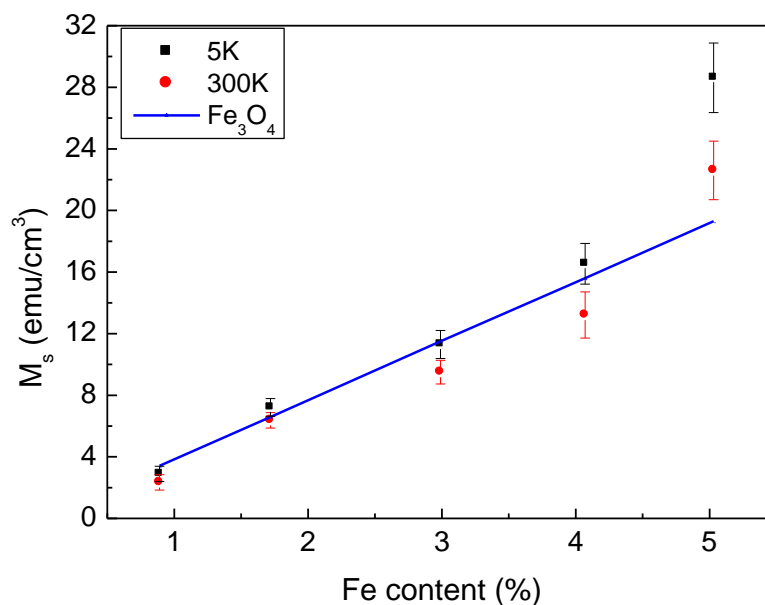


Figure (7.12): The saturation magnetisation at 5 K and 300 K of $(\text{In}_{1-x}\text{Fe}_x)_2\text{O}_3$ films as a function of Fe doping level compared with expected magnetisation if all the films were Fe_3O_4 .

Figure 7.13 shows the coercive field as a function of Fe content measured at 5 K and 300 K. The coercive fields increase as the Fe content increased then start decreases at 3%. This result suggests the formation of Fe_3O_4 cluster in the films and the fraction of Fe_3O_4 nanoparticles increases with an increase in Fe content hence the coercivities are always related to the structural defect. From the Stoner-Wohlfarth model the anisotropy coercive field is determined from $(B_c=2K/M_s)$ where K is the anisotropy energy of the particle and M_s the saturation magnetisation. From the Stoner-Wohlfarth model and by using the bulk magnetisation and coercive field of Fe_3O_4 the coercive field at low temperature is about 632 Oe which is in agreement with the measured value for the 5% Fe film shown in fig. 7.13.

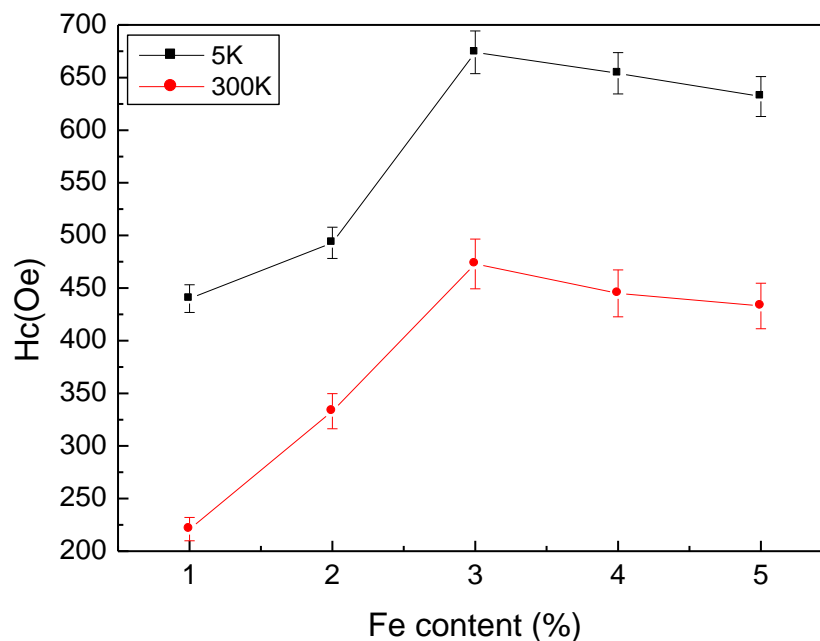


Figure (7.13): The coercive field (H_c) at 5 K and 300 K of the $(\text{In}_{1-x}\text{Fe}_x)_2\text{O}_3$ films as a function of Fe doping level.

The ZFC and FC experiment was employed to measure the magnetisation of the film with 5% Fe. Fig.7.14 shows the magnetisation temperature dependence, ZFC and FC, under in-plane magnetic field of 250 Oe. This indicates the presence of nanoparticle in this film as had been identified by EXAFS. Using Stoner-Wohlfarth model the average size (V) of the nanoparticles can be calculated from the formula ($k_B T_B = KV/25$) [48], hence k_B is Boltzmann's constant, T_B is blocking temperature and K is the anisotropy energy. From fig.7.14 the blocking temperature is at 115 K due to the nanoparticles of Fe_3O_4 in the 5% Fe film. Therefore, the average size of the nanoparticles was evaluated from the blocking temperature to be $(14.5 \text{ nm})^3$. This size is rather large which could be due to the anisotropy was actually higher than the assumed, bulk, value.

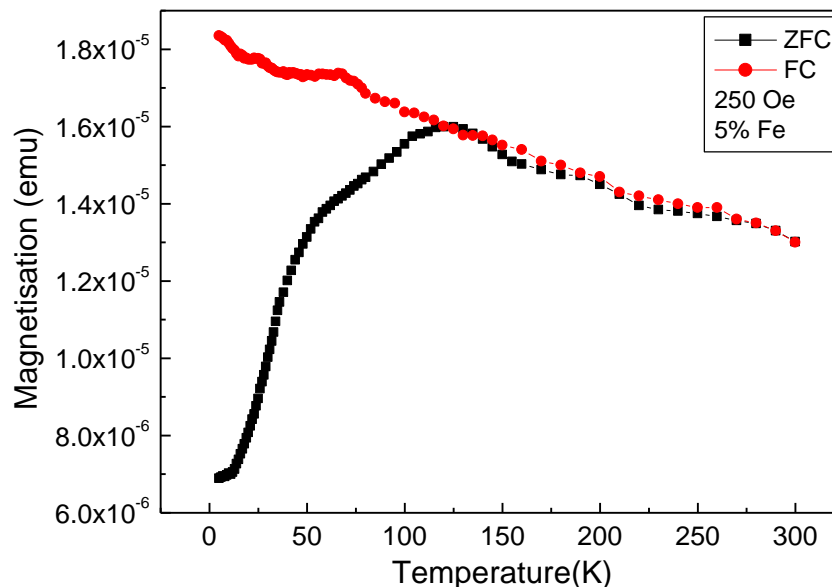


Figure (7.14): Zero field-cooled (ZFC) and field -cooled (FC) magnetisation of $(\text{In}_{0.95}\text{Fe}_{0.05})_2\text{O}_3$ thin film, taken at 250Oe, as a function of temperature. The ZFC curve shows the blocking temperature T_B at 115K due to the Fe_3O_4 nanoparticles in the film.

In order to avoid the formation of Fe_3O_4 nanoparticles in the films and also to study the influence of the annealing on the structure and magnetic properties of Fe doped In_2O_3 , other series of thin films were made with 5% Fe under the same growth conditions. Four films were grown in KACST from the same target at 600 °C and oxygen partial pressure of 2×10^{-3} mTorr. Three of these films were annealed after deposition process for 30 minutes in vacuum at 300 °C , 400 °C and 500 °C. The XRD analysis shows again a sign for presence of the Fe_3O_4 nanoparticles as shown in fig.7.15 for the film annealed at 500 °C. This measurement was performed by Hakimi in Cambridge University.

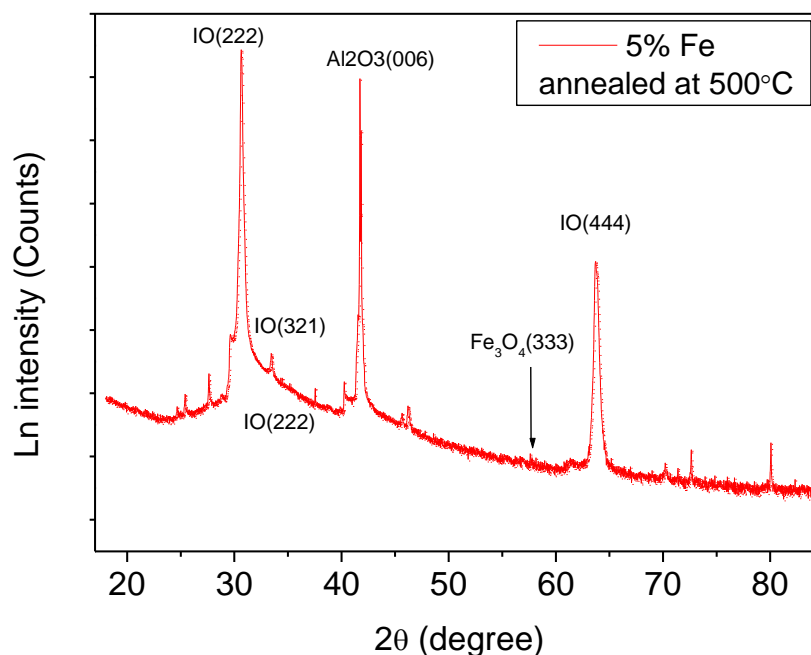


Figure (7.15): XRD data for $(\text{In}_{0.95}\text{Fe}_{0.05})_2\text{O}_3$ thin film annealed at 500 K, demonstrate the present of Fe_3O_4 nanoparticles in the film.

The magnetic properties of these films were studied using a SQUID magnetometer. Fig.7.16 shows the magnetic hysteresis loops measured at 5 K and 300K and in-plane magnetic field up to 1 T. The diamagnetic contribution from the substrate has been subtracted. The as-grown film exhibits a lower magnetisation and coercive field compared with the as-grown film of the first series of Fe thin films shown in fig.7.12 due to fewer Fe_3O_4 nanoparticles in this film. The magnetisation is annealing temperature-independent. However, the magnetisation was enhanced with annealing in vacuum which could be attributed to an increase of the concentration of oxygen vacancies.

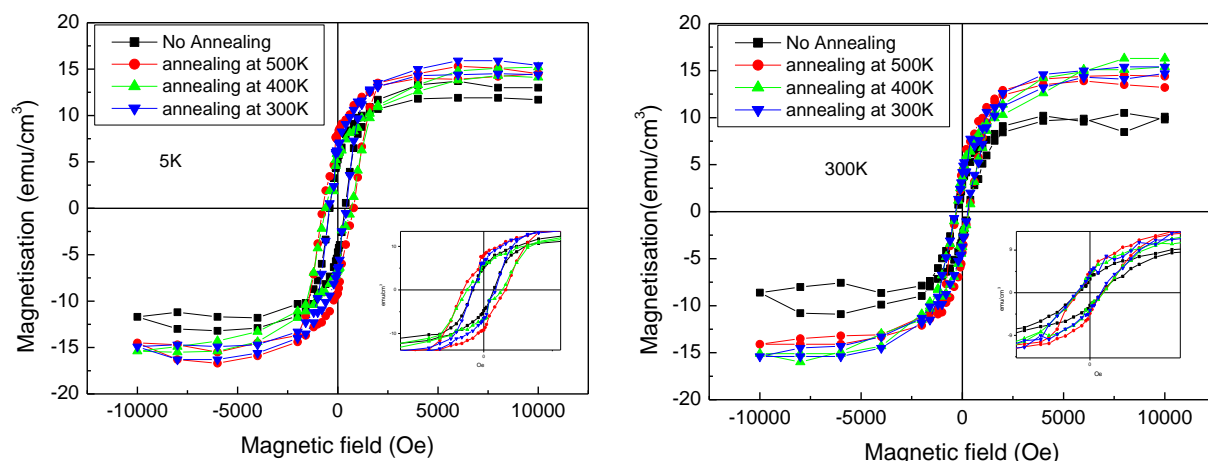


Figure (7.16): The hysteresis loops measured at 5 K and 300 K of the as-grown and annealed $(\text{In}_{0.95}\text{Fe}_{0.05})_2\text{O}_3$ thin films (the diamagnetic contribution from the substrate has been subtracted). The Insets show the blow-up of the region around the origin.

The influence of Sn doping on Fe-doped In_2O_3 films was investigated, where three films of $(\text{In}_{0.95-y}\text{Fe}_{0.05}\text{Sn}_y)_2\text{O}_3$ were grown with $y = 0, 0.05$ and 0.1 . The films were grown in KACST under the same growth conditions. Fig.7.17 shows the magnetic hysteresis loop at 5 K and 300 K measured by the SQUID under a magnetic field of 1 T. The magnetic moment decreases with increases of n concentration which could be due to prevent the formation of the nanoparticles in the films.

The MCD spectra of these films were measured at room temperature in applied magnetic field up to 1.8 T as shown in fig.7.18. The spectra show a peak at about 2.2 eV for the pure Fe-doped In_2O_3 films whereas the peak has totally disappeared for the films with 5% and 10% tin (Sn). As found previously that the Fe-doped In_2O_3 film contains Fe_3O_4 nanoparticles this means that the peak shown in the Fe-doped In_2O_3 films is due to the Fe_3O_4 nanoparticles. Adding tin leads to the disappearance of the peaks at 2.2 eV which is in agreement with the magnetic data shown in fig.7.17.

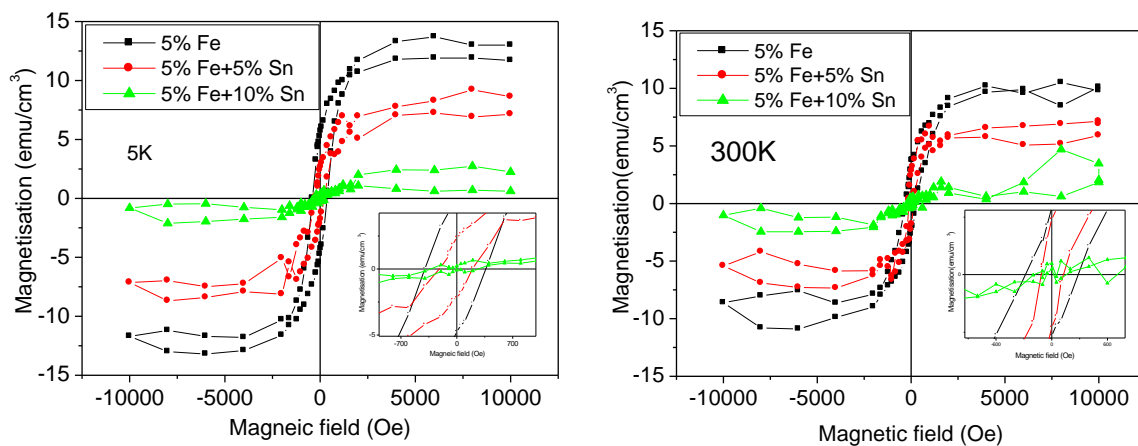


Figure 7.17: The hysteresis loops measured at 5 K and 300 K of pure $(\text{In}_{0.95}\text{Fe}_{0.05})_2\text{O}_3$ thin films and films doped with 5% and 10% Sn (the diamagnetic contribution from the substrate has been subtracted). The Insets show the blow-up of the region around the origin.

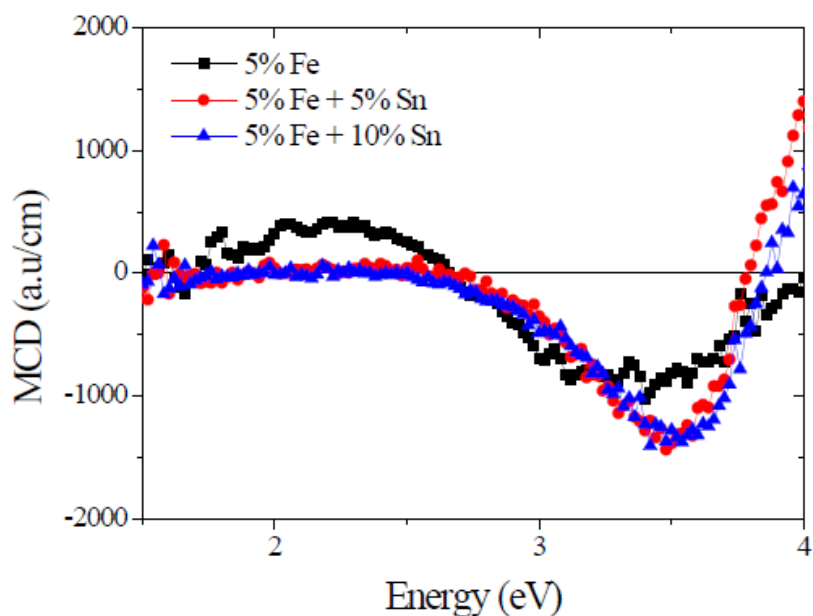


Figure 7.18: Room temperature MCD spectra taken at 1.8 T of pure $(\text{In}_{0.95}\text{Fe}_{0.05})_2\text{O}_3$ thin films and films doped with 5% and 10% Sn (the substrate contribution from has been subtracted).

The MCD spectra also show a feature at 3.4 eV which increased with tin doping due to the increase of the carrier concentration in the films. Both magnetic and MCD data give good evidence that adding Sn to the Fe-doped In₂O₃ films leads to the prevention of the formation of the nanoparticles where adding Sn may help the Fe atom to substitute the In₂O₃ lattice rather than forming cluster or nanoparticles.

The second group of Fe-doped In₂O₃ thin films was grown to optimize the growth processes and to study the magnetic and magneto-optic properties. Two thin films of (In_{0.95} Fe_{0.05})₂ O₃ were grown at 5×10^{-3} mTorr and 100 mTorr by PLD technique in Xiao-Hong Xu's group, China. The target was prepared for the PLD from high-purity In₂O₃ (99.995%) and Fe₂O₃ (99.998%) powders. The stoichiometric mixture was annealed in air at 500, 650 and 800 °C for 12 hours. The calcined powder was then pressed and sintered in air at 1100 °C for 12 hours and the resultant pellet was used as a target in the PLD. The films were deposited on a sapphire substrate at 600 °C by PLD with energy of 300 mJ/pulse. The data presented in this section of these films have been published in [4].

The XRD patterns of (In_{0.95} Fe_{0.05})₂ O₃ film grown at 5×10^{-3} mTorr can be shown in fig.7.19, measured by Xu in Shanxi Normal University Linfen, China. The XRD pattern shows high crystalline with single phase cubic structure and well-oriented (222) as the un-doped In₂O₃ structure. No secondary phases relating to metallic Fe clusters or Fe oxide are observed which indicates that Fe ions are substituted in to the In³⁺ sites of the In₂O₃ lattice without changing the cubic bixbyite structure. This result is totally different to that found for the film grown in KACST shown in fig.7.9.

Removed by the author for copyright reasons

Figure (7.19): XRD data of $(\text{In}_{1-x}\text{Fe}_x)_2\text{O}_3$, shows the patterns of $(\text{In}_{0.95}\text{Fe}_{0.05})_2\text{O}_3$ grown at 5×10^{-3} mTorr [4].

Measurements of the magnetic properties of these films were made with a SQUID magnetometer. Fig.7.20 shows the magnetic hysteresis loops measured at 5 K and 300K for $(\text{In}_{0.95}\text{Fe}_{0.05})_2\text{O}_3$ films grown at 5×10^{-3} mTorr and 100 mTorr. The diamagnetic contribution from the substrate has been subtracted as shown in the insets. The samples illustrate a clear room temperature (RT) ferromagnetic behaviour. The magnetisation of the film deposited at 5×10^{-3} mTorr is independent of temperature, which strongly indicates that the T_c of the film is above room temperature. This is therefore essential for developing practical spintronic devices. In contrast, the magnetisation of the film deposited at 100 mTorr displays temperature dependent behaviour and the magnetisation is relatively small which suggests the presence of a paramagnetic contribution in the film besides the ferromagnetic moment.

Removed by the author for copyright reasons

Figure (7.20): The hysteresis loops measured at 5K and 300K of (In_{0.95} Fe_{0.05})₂O₃ thin films deposited under various oxygen pressure of a) 5×10^{-3} mTorr and b) 100 mTorr (the diamagnetic contribution from the substrate has been subtracted). The Insets show the blow-up of the region around the origin [4].

The expected paramagnetic susceptibility per volume (χ/V) from the Fe²⁺ ions at 5 K was calculated using $\chi/V = \frac{N x p_{eff}^2 \mu_B^2 \mu_o}{3K_B T V}$ where p_{eff} is the effective number of Bohr magnetons (μ_B), N is the number of host ions per cm³ and x is the Fe²⁺ concentration. The p_{eff} of Fe²⁺ is taken only for the spin value of $p= 4.90$ which is for the low symmetry that is give fully quench of the orbital contribution. The measured values of Curie constant C_{meas} and the calculated values C of the Fe²⁺ of these films are given in the Table (7.2). The Curie constant values measured for both films were close to the expected values for Fe²⁺. This result indicates that the Fe ions in the film are Fe²⁺ and all the Fe²⁺ ions in the films are paramagnetic. This result is similar to what have been found for Co²⁺ ions shown in fig.7.6.

Film thickness (nm)	Oxygen Pressure (mTorr)	$(\chi/V)_{\text{meas}} \times 10^{-3}$	$C_{\text{meas}} \times 10^{-3}$	$(\chi/V) \times 10^{-3}$	$C_{\text{calc}} \times 10^{-3}$
319	5×10^{-5}	1.28	6.40	1.46	7.31
224	100	1.43	7.14	1.46	7.31

Table (7.2): Summary of the paramagnetic susceptibility (χ) and Curie constant measured values of $(\text{In}_{0.95}\text{Fe}_{0.05})_2\text{O}_3$ thin films and the expected values of Fe^{2+} ions respectively.

The transport properties of these films were measured by Xu using four-point configuration. Fig.7.21 shows the temperature dependence of resistance (R) of $(\text{In}_{0.95}\text{Fe}_{0.05})_2\text{O}_3$ films grown at 5×10^{-3} mTorr and 100 mTorr. This plot indicates metallic behaviour of the film grown at 5×10^{-3} mTorr whereas the film grown at 100 mTorr shows classic semiconductor behaviour. This illustrates that the oxygen partial pressure effects on the resistivity and then on carrier density due to the variation in the number of Fe^{2+} ions or the density of the Oxygen vacancies. Therefore, the difference in the ferromagnetic behaviour between the film grown at 5×10^{-3} mTorr and the one grown at 100 mTorr exists because that the former film lies in the metallic regime and the later one lies in the insulating regime.

Removed by the author for copyright reasons

Figure (7.21): Resistance temperature dependence for the two $(\text{In}_{0.95}\text{Fe}_{0.05})_2\text{O}_3$ thin films grown at 5×10^{-3} mTorr and 100mTorr. The inset is $\text{Log RVs } T^{1/4}$ for the film grown at 100mTorr [4].

In order to verify the origin of the magnetism the MCD spectroscopy were measured for these films. Fig.7.22 shows the MCD spectra of $(\text{In}_{0.95}\text{Fe}_{0.05})_2\text{O}_3$ films measured at room temperature in applied magnetic field up to 1.8 Tesla perpendicular to surface of the films. The contribution from the substrate has been subtracted from the MCD spectra.

Fig.7.22 shows a positive signal for the film grown at 5×10^{-3} mTorr around the band edge whereas the film grown at 100 mTorr exhibits no MCD signal. Moreover, the film grown at 5×10^{-3} mTorr shows a contribution from the forbidden transitions on the energy ranges $2.75 < E < 3.70$ which is absent in the film grown at high oxygen atmosphere (100 mTorr). This is because the former film is metallic and contains a fraction of Fe^{2+} ions and these ions act as acceptors which generate a spin polarized conduction band. Hence any exchange splitting in the

conduction band state will leads to a large imbalance in the density of states at Fermi level which causes the strong MCD signal in the film grown at 5×10^{-3} mTorr. In contrast the film grown at high oxygen atmosphere (100 mTorr) is semiconducting and had few carriers or contained a very few Fe²⁺. In this film the states near the Fermi level are localized and the density of states is potential dependent and energy independent. Therefore, any spin splitting of these localized states will not lead to unequal densities at the Femi level and as a result the MCD signal is very low which could be below the experimental limit.

**Removed by the
author for copyright reasons**

Figure (7.22): Room temperature MCD spectra taken at 1.8T of (In_{0.95} Fe_{0.05})₂O₃ thin films grown at grown at 5×10^{-3} mTorr and 100 mTorr [4].

7.4 Summary and Conclusions

This chapter reported the investigation of the magnetic and magneto-optical properties of Co and Fe-doped In₂O₃. Ferromagnetic beyond room temperature was found in Co and Fe-doped In₂O₃ films grown in two different research group using different techniques. The investigation of XRD and EXAFS indicated that TM ions in the films are predominately TM²⁺ and substitute for In³⁺ rather than forming a defect phase. In this work the major emphasis is focused on exploring the contribution of the TM to the magnetisation in order to determine the origin of ferromagnetism in this system. A new simple method was established and the use this method illustrated that the TM²⁺ ions are paramagnetic and do not contribution to the ferromagnetic moment of the films.

The magneto-optics measurement showed a positive contribution from the forbidden transition in the energy range $2.75 < E < 3.7$ eV for (In_{1-x}Co_x)₂O₃ and (In_{1-x}Fe_x)₂O₃ thin films grown at low oxygen pressure and this transition is absent for the films grown at high oxygen pressure. This is good evidence for a donor state formed in the band gap energy of In₂O₃ and located closed to conduction band. Oxygen vacancies are found to be the origin of these donor states which were calculated to lay at 0.9 eV below the conduction band.

The magnetic and magneto-optics measurement together gives convincing evidence that the magnetism observed in these films is due to the polarised electrons in localised donor state and to the oxygen vacancies. Oxygen partial pressure plays a crucial role for the carrier concentration and the density of oxygen vacancies. Hence a decrease of oxygen partial pressure leads to an increase of the density of oxygen vacancies and *vice versa*.

The (In_{1-x} Fe_x)₂O₃ films grown in KACST by PLD contain a fraction of Fe₃O₄ nanoparticles whereas Fe ions substitute for In³⁺ in Fe-doped In₂O₃ films grown by PLD in Xu group. This indicates that the TM doped In₂O₃ is very sensitive to the growth method. The formation of Fe₃O₄ nanoparticles could be attributed to either the grinding of the powder used to make the target or to the temperatures that were involved in annealing the powder. However, adding Sn to the Fe-doped In₂O₃ films may help to reduce the formation of Fe₃O₄ nanoparticles.

7.5 References

1. A. M. H. R. Hakimi, M. G. Blamire, S. M. Heald, M. S. Alshammari, M. S. Alqahtani, D. S. Score, H. J. Blythe, A. M. Fox and G. A. Gehring, *Physical Review B* **84** (8), 085201 (2011).
2. M. Venkatesan, R. D. Gunning, P. Stamenov and J. M. D. Coey, *Journal of Applied Physics* **103** (7), 07D135-133 (2008).
3. X.-H. Xu, F.-X. Jiang, J. Zhang, X.-C. Fan, H.-S. Wu and G. A. Gehring, *Applied Physics Letters* **94** (21), 212510-212513 (2009).
4. F.-X. Jiang, X.-H. Xu, J. Zhang, X.-C. Fan, H.-S. Wu, M. Alshammari, Q. Feng, H. J. Blythe, D. S. Score, K. Addison, M. Al-Qahtani and G. A. Gehring, *Journal of Applied Physics* **109** (5), 053907-053907 (2011).
5. T. Fukumura, H. Toyosaki and Y. Yamada, *Semiconductor Science and Technology* **20** (4), S103 (2005).
6. S. B. Ogale, R. J. Choudhary, J. P. Buban, S. E. Lofland, S. R. Shinde, S. N. Kale, V. N. Kulkarni, J. Higgins, C. Lanci, J. R. Simpson, N. D. Browning, S. Das Sarma, H. D. Drew, R. L. Greene and T. Venkatesan, *Physical Review Letters* **91** (7), 077205 (2003).
7. T. Fukumura, Z. Jin, A. Ohtomo, H. Koinuma and M. Kawasaki, *Applied Physics Letters* **75** (21), 3366-3368 (1999).
8. Y. Matsumoto, M. Murakami, T. Shono, T. Hasegawa, T. Fukumura, M. Kawasaki, P. Ahmet, T. Chikyow, S.-y. Koshihara and H. Koinuma, *Science* **291** (5505), 854-856 (2001).
9. C. B. Fitzgerald, M. Venkatesan, A. P. Douvalis, S. Huber, J. M. D. Coey and T. Bakas, *Journal of Applied Physics* **95** (11), 7390-7392 (2004).

10. J. Philip, N. Theodoropoulou, G. Berera, J. S. Moodera and B. Satpati, *Applied Physics Letters* **85** (5), 777-779 (2004).
11. H. Kim, M. Osofsky, M. M. Miller, S. B. Qadri, R. C. Y. Auyeung and A. Pique, *Applied Physics Letters* **100** (3), 032404-032403 (2012).
12. D. Bérardan, E. Guilmeau and D. Pelloquin, *Journal of Magnetism and Magnetic Materials* **320** (6), 983-989 (2008).
13. L. M. Huang, C. M. Araujo and R. Ahuja, *Epl* **87** (2) (2009).
14. H. W. Ho, B. C. Zhao, B. Xia, S. L. Huang, J. G. Tao, A. C. H. Huan and L. Wang, *Journal of Physics-Condensed Matter* **20** (47) (2008).
15. Sub, iacute, G. as, J. Stankiewicz, F. Villuendas, M. Lozano, P. a, Garc and J. a, *Physical Review B* **79** (9), 094118 (2009).
16. J. Philip, A. Punnoose, B. I. Kim, K. M. Reddy, S. Layne, J. O. Holmes, B. Satpati, P. R. LeClair, T. S. Santos and J. S. Moodera, *Nat Mater* **5** (4), 298-304 (2006).
17. G. Z. Xing, J. B. Yi, D. D. Wang, L. Liao, T. Yu, Z. X. Shen, C. H. A. Huan, T. C. Sum, J. Ding and T. Wu, *Physical Review B* **79** (17), 174406 (2009).
18. R. P. Panguluri, P. Kharel, C. Sudakar, R. Naik, R. Suryanarayanan, V. M. Naik, A. G. Petukhov, B. Nadgorny and G. Lawes, *Physical Review B* **79** (16), 165208 (2009).
19. G. Subías, J. Stankiewicz, F. Villuendas, M. P. Lozano and J. García, *Physical Review B* **79** (9), 094118 (2009).
20. Y. K. Yoo, Q. Xue, H.-C. Lee, S. Cheng, X. D. Xiang, G. F. Dionne, S. Xu, J. He, Y. S. Chu, S. D. Preite, S. E. Lofland and I. Takeuchi, *Applied Physics Letters* **86** (4), 042506-042503 (2005).

21. O. D. Jayakumar, I. K. Gopalakrishnan, S. K. Kulshreshtha, A. Gupta, K. V. Rao, D. V. Louzguine-Luzgin, A. Inoue, P. A. Glans, J. H. Guo, K. Samanta, M. K. Singh and R. S. Katiyar, *Applied Physics Letters* **91** (5), 052504-052503 (2007).
22. D. Chu, Y.-P. Zeng, D. Jiang and Z. Ren, *Applied Physics Letters* **91** (26), 262503-262503 (2007).
23. P. F. Xing, Y. X. Chen, S.-S. Yan, G. L. Liu, L. M. Mei, K. Wang, X. D. Han and Z. Zhang, *Applied Physics Letters* **92** (2), 022513-022513 (2008).
24. F.-X. Jiang, X.-H. Xu, J. Zhang, H.-S. Wu and G. A. Gehring, *Applied Surface Science* **255** (6), 3655-3658 (2009).
25. H. W. Ho, B. C. Zhao, B. Xia, S. L. Huang, Y. Wu, J. G. Tao, A. C. H. Huan and L. Wang, *Journal of Physics: Condensed Matter* **20** (47), 475204 (2008).
26. N. H. Hong, J. Sakai, N. T. Huong, A. Ruyter and V. Brize, *Journal of Physics-Condensed Matter* **18** (29), 6897-6905 (2006).
27. I. Hamberg, C. G. Granqvist, K. F. Berggren, B. E. Sernelius and L. Engström, *Physical Review B* **30** (6), 3240-3249 (1984).
28. C. Nunes de Carvalho, G. Lavareda, A. Amaral, O. Conde and A. R. Ramos, *Journal of Non-Crystalline Solids* **352** (23–25), 2315-2318 (2006).
29. J.-H. Lee, S.-Y. Lee and B.-O. Park, *Materials Science and Engineering: B* **127** (2–3), 267-271 (2006).
30. J. Stankiewicz, F. Villuendas, J. Bartolomé and J. Sesé, *Journal of Magnetism and Magnetic Materials* **310** (2, Part 3), 2084-2086 (2007).
31. J. Stankiewicz, F. Villuendas, Bartolomé and Juan, *Physical Review B* **75** (23), 235308 (2007).

32. A. M. H. R. Hakimi, F. Schoofs, R. Bali, N. A. Stelmashenko, M. G. Blamire, S. Langridge, S. A. Cavill, G. van der Laan and S. S. Dhesi, *Physical Review B* **82** (14), 144429 (2010).
33. T. Thomas, G. Milan, S. Gisela, J. Gerhard, B. Sebastian and G. Eberhard, *New Journal of Physics* **10** (5), 055009 (2008).
34. A. Ney, K. Ollefs, S. Ye, T. Kammermeier, V. Ney, T. C. Kaspar, S. A. Chambers, F. Wilhelm and A. Rogalev, *Physical Review Letters* **100** (15), 157201 (2008).
35. A. Barla, G. Schmerber, E. Beaurepaire, A. Dinia, H. Bieber, S. Colis, F. Scheurer, J. P. Kappler, P. Imperia, F. Nolting, F. Wilhelm, A. Rogalev, D. Müller and J. J. Grob, *Physical Review B* **76** (12), 125201 (2007).
36. Z. G. Yu, J. He, S. Xu, Q. Xue, O. M. J. van't Erve, B. T. Jonker, M. A. Marcus, Y. K. Yoo, S. Cheng and X.-d. Xiang, *Physical Review B* **74** (16), 165321 (2006).
37. L. X. Guan, J. G. Tao, Z. R. Xiao, B. C. Zhao, X. F. Fan, C. H. A. Huan, J. L. Kuo and L. Wang, *Physical Review B* **79** (18), 184412 (2009).
38. J. He, S. Xu, Y. K. Yoo, Q. Xue, H.-C. Lee, S. Cheng, X. D. Xiang, G. F. Dionne and I. Takeuchi, *Applied Physics Letters* **86** (5), 052503-052503 (2005).
39. J. Stankiewicz, F. Villuendas and J. Bartolomé, *Physical Review B* **75** (23), 235308 (2007).
40. J. R. Neal, A. J. Behan, R. M. Ibrahim, H. J. Blythe, M. Ziese, A. M. Fox and G. A. Gehring, *Physical Review Letters* **96** (19), 197208 (2006).
41. K. Ando, H. Saito, Z. Jin, T. Fukumura, M. Kawasaki, Y. Matsumoto and H. Koinuma, *Applied Physics Letters* **78** (18), 2700-2702 (2001).

42. A. J. Behan, J. R. Neal, R. M. Ibrahim, A. Mokhtari, M. Ziese, H. J. Blythe, A. M. Fox and G. A. Gehring, *Journal of Magnetism and Magnetic Materials* **310** (2, Part 3), 2158-2160 (2007).
43. F.-X. Jiang, X.-H. Xu, J. Zhang, X.-C. Fan, H.-S. Wu and G. A. Gehring, *Applied Physics Letters* **96** (5), 052503-052503 (2010).
44. S. M. Heald, T. Kaspar, T. Droubay, V. Shutthanandan, S. Chambers, A. Mokhtari, A. J. Behan, H. J. Blythe, J. R. Neal, A. M. Fox and G. A. Gehring, *Physical Review B* **79** (7), 075202 (2009).
45. D. A. Schwartz, N. S. Norberg, Q. P. Nguyen, J. M. Parker and D. R. Gamelin, *Journal of the American Chemical Society* **125** (43), 13205-13218 (2003).
46. A. Walsh, J. L. F. Da Silva, S.-H. Wei, C. Körber, A. Klein, L. F. J. Piper, A. DeMasi, K. E. Smith, G. Panaccione, P. Torelli, D. J. Payne, A. Bourlange and R. G. Egdell, *Physical Review Letters* **100** (16), 167402 (2008).
47. L.-M. Tang, L.-L. Wang, D. Wang, J.-Z. Liu and K.-Q. Chen, *Journal of Applied Physics* **107** (8), 083704-083705 (2010).
48. F. C. Fonseca, G. F. Goya, R. F. Jardim, R. Muccillo, N. L. V. Carreño, E. Longo and E. R. Leite, *Physical Review B* **66** (10), 104406 (2002).

Chapter 8

Conclusions and Future Work

8.1 Conclusions

This study has investigated the magnetic and magneto-optical properties of LSMO, multiferroic GdMnO₃ and TM-doped In₂O₃ thin films grown under different conditions. Moreover, optical and magneto-optical measurements were made on a STO substrate because it had been used to grow high quality thin films of LSMO and GdMnO₃ but it was found to have some disadvantages for an optical study. The magnetic properties of each sample were measured in a SQUID and the magneto-optical properties were performed in Faraday geometry.

8.1.1 LSMO Thin Films

The magnetic and magneto-optical properties of LSMO thin films grown on both STO and sapphire substrate were studied. Increasing both the concentration of Sr content and oxygen growth pressure shows an improvement of magnetic behaviour for LSMO films grown on both STO and sapphire substrate. The ratio of Mn⁴⁺/Mn³⁺ can be controlled by controlling the oxygen growth pressure. Therefore, increase of oxygen pressure means increasing the number of holes in the films and thus increasing the Mn⁴⁺/Mn³⁺ ratio, and subsequently enhancing the magnetic properties of LSMO films. In this study, It was found that the LSMO film of about 80nm exhibits one of the highest values of T_C=340 K compared to the previous studies [1-2]. However, the reduction in the magnetisation in this film is attributed to the strain

and interface between the film and the substrate [1]. The value of so-called dead layer is about 23 nm which is about 20 times higher than the previously reported dead layer of 1.2 nm for LSMO on SrTiO₃ (001) [3].

The strong MCD peak at the band gap at about 3.3 eV of the film grown on sapphire was found to be shifted to lower energy with decreasing oxygen pressure which could be attributed to the decrease of Mn⁴⁺ fraction and band width with reduction in oxygen. The magnitude of the signal in the temperature dependence of MCD measurement is found to be proportional to the polarisation of band electrons which is needed in spintronics. This result shows that a sapphire substrate is a promising substrate for LSMO films for magneto-optical study. On the other hand, the MCD spectrum of LSMO films on STO substrate are dominated by the magneto optical properties and birefringence behaviour arising from the STO substrate. Hence, the absorption of STO above its band gap at about 3.3 eV, its magneto-optical properties and the birefringence are a limitation of the optical study of LSMO films.

The influence of birefringence on the magneto-optics of STO was investigated. This study is considered the first attempt that investigated the influence of birefringence on the magneto-optical properties of STO using the Sato method. It was found that a STO substrate has a strongly temperature dependence of the MCD below the band gap which also varied linearly with applied magnetic field. This result indicates that it is not easy to study samples that are both birefringent and magnetic and also that STO substrates are not suitable for optical studies. However magneto-optical studies are a very powerful technique to study LSMO films.

8.1.2 GdMnO₃ Thin Films

The magnetic, optical and magneto-optical properties of epitaxial films of GdMnO₃ grown on SrTiO₃ and LaAlO₃ substrate were studied. This study is considered the first attempt that investigated the magnetic and magneto-optical properties of epitaxial GdMnO₃ thin films. Considerable differences have been found between the magnetic behaviour of bulk GdMnO₃ and that grown on the two substrates, STO and the twinned substrate of LAO. These apply different strains to the manganite film. The Néel temperature is reduced and there is some evidence that a canted phase appears with the onset of anti-ferromagnetism for both films.

The optical absorption data on these films was dominated by the strong absorption that starts around 3 eV, but the 2 eV peak was not sufficiently strong to be detected. However, both peaks featured strongly in the MCD data measured with thin films of GdMnO₃ grown on STO. The optical absorption at 3 eV is much stronger than at 2 eV, but the MCD is considerably stronger at 2 eV. A dramatic result was the stark difference between the shapes of the spectra taken in a field of 5kOe and at remanence, as well as in the hysteresis loops. The 2 eV peak is attributed to the charge transfer transition between Mn ions occurring near 2 eV, whereas the 3 eV peak is due to the contribution from the STO substrate. Hence, the STO substrate exhibited a MCD temperature dependent signal at about 3 eV and this signal dominates the MCD spectra, so that the MCD peak at 3 eV is due to the STO substrate. The transition near 2 eV was more strongly dependent on temperature, but much less sensitive to the external field, and was observed in the remnant spectrum. It was a clear feature in the MCD, whereas it is strongly suppressed in the optical absorption. This is because it depends so strongly on the spin dependence of the occupation of the Mn *d* orbitals. It also depends on the relative orientation of the spins of the

neighbouring Mn ions and on the Mn-O-Mn bond angle. It is clear that study of the MCD spectrum of this material is a rich source of information that is not available from a study of the magnetisation and the absorption alone.

8.1.3 Co and Fe- Doped In_2O_3 Thin Films

The magnetic and magneto-optical properties of Co and Fe-doped In_2O_3 thin films were studied. The study showed that the RT ferromagnetic of $(\text{In}_{1-x}\text{Co}_x)_2\text{O}_3$ and $(\text{In}_{1-x}\text{Fe}_x)_2\text{O}_3$ thin films is ascribed to the substitution of Co and Fe ions for In ions and not due to either the presence of metallic clusters or oxides secondary phases in the films.

A new method was established to explore the contribution of the transition metal ions (TM) to the magnetisation in order to determine the origin of ferromagnetism in this system. This method was used to estimate the paramagnetic contribution of the films at 5K and compare it with the expected paramagnetic susceptibility from the TM ions which was calculated at the fully quenching of the orbital angular momentum. This method revealed that the Co and Fe ions in $(\text{In}_{1-x}\text{Co}_x)_2\text{O}_3$ and $(\text{In}_{1-x}\text{Fe}_x)_2\text{O}_3$ thin films are paramagnetic and do not contribute to the magnetisation. This result is in agreement with a X-ray magnetic circular dichroism (XMCD) study reported previously for $\text{Zn}_{1-x}\text{Co}_x\text{O}$ films [4-5] Co-doped indium tin oxide (ITO) [6] and Mn doped ITO [7].

The study of magneto-optical properties of Co and Fe-doped In_2O_3 is considered to be the first attempt on these materials. This study revealed that there are donor states formed in the band gap energy of In_2O_3 and located closed to the conduction band. The origin of these donor states is oxygen vacancies which were calculated to lie at 0.9 eV below the conduction band [8-9]. The density of oxygen

vacancies depends on the oxygen partial pressure and a decrease of oxygen partial pressure leads to an increase in the number of the oxygen vacancies and vice versa. The magnetic and magneto-optical properties together indicate that the observed ferromagnetism in TM-doped In_2O_3 is due to the polarised electrons in localized donor state associated with oxygen vacancies.

EXAFS measurement showed the existence of Fe_3O_4 nanoparticles in some of Fe-doped In_2O_3 thin films. In this study, the calculation of the expected magnetisation from Fe_3O_4 nanoparticles in the thin films supports the EXAFS result of existence the Fe_3O_4 nanoparticles in these films. The existence of Fe_3O_4 nanoparticles in these films are very probably due to the processing conditions of fabrication. This indicates that the TM-doped In_2O_3 thin films are extremely sensitive to the fabrication method and to the processing conditions. However, adding Sn to the Fe-doped In_2O_3 films could lead to a reduction of the formation of Fe_3O_4 nanoparticles and may help the Fe atoms to substitute the In_2O_3 lattice rather than forming cluster or nanoparticles.

8.2 Future Work

There are a number of unresolved issues that it would be interesting to pursue in further work for LSMO and TM-doped In_2O_3 films.

The quality of LSMO thin-film is crucial for device performance. A high quality LSMO thin film should exhibit a large magnetization, small residual resistivity and smooth surface morphology and avoid surface segregation. The high quality LSMO film can illustrate saturation magnetisation near to the expected $3.7 \mu_B/\text{Mn}$ value where values of $4 \mu_B/\text{Mn}$ have observed previously in LSMO single crystals [10], polycrystals [11] and thin films [12]. It would be really interesting to grow high-quality thin film of LSMO. This requires investigating the film with x-ray

diffraction, atomic force microscopy, SQUID, van der Pauw configuration and scanning transmission electron microscopy.

The TM-doped In_2O_3 thin films are very sensitive to the fabrication method and processing conditions. The most important issue is to grow reproducible thin films of TM-doped In_2O_3 . This will need to investigate the growth conditions such as the method of preparing and grinding the powder, effect of different precursor, and plume quality. Further investigation is required on (V, Cr, Mn, Ni, Cu and Zn)-doped In_2O_3 and tin-doped indium oxide (ITO). On the other hand, it would be very interesting to grow high quality Fe-doped In_2O_3 for the application in devices. All these together will provide for a deeper understanding of the origin of ferromagnetism in DMS films.

Finally, since the discovery of graphene in 2004 [13], the electrical properties of graphene have attracted much attention for voluminous fundamental studies. Most of the recent research has focused on growth of large sheets of monolayer or bilayer graphene [14]. Following interesting work on the magneto-optics studies of graphene films in the infrared (IR) and noting that the Faraday rotation had been calculated for graphite but never measured; we attempted to grow graphite on sapphire substrate using PLD and spin coating but some difficulties were faced, which delayed the project.

8.3 Reference

1. A. K. Pradhan, D. Hunter, T. Williams, B. Lasley-Hunter, R. Bah, H. Mustafa, R. Rakhimov, J. Zhang, D. J. Sellmyer, E. E. Carpenter, D. R. Sahu and J. L. Huang, *Journal of Applied Physics* **103** (2), 023914-023918 (2008).
2. Y. P. Sukhorukov, A. P. Nosov, N. N. Loshkareva, E. V. Mostovshchikova, A. V. Telegin, E. Favre-Nicolin and L. Ranno, *Journal of Applied Physics* **97** (10), 103710-103715 (2005).
3. M. Huijben, L. W. Martin, Y. H. Chu, M. B. Holcomb, P. Yu, G. Rijnders, D. H. A. Blank and R. Ramesh, *Physical Review B* **78** (9) (2008).
4. A. Ney, K. Ollefs, S. Ye, T. Kammermeier, V. Ney, T. C. Kaspar, S. A. Chambers, F. Wilhelm and A. Rogalev, *Physical Review Letters* **100** (15) (2008).
5. A. Barla, G. Schmerber, E. Beaurepaire, A. Dinia, H. Bieber, S. Colis, F. Scheurer, J. P. Kappler, P. Imperia, F. Nolting, F. Wilhelm, A. Rogalev, D. Mueller and J. J. Grob, *Physical Review B* **76** (12) (2007).
6. A. M. H. R. Hakimi, F. Schoofs, R. Bali, N. A. Stelmashenko, M. G. Blamire, S. Langridge, S. A. Cavill, G. van der Laan and S. S. Dhesi, *Physical Review B* **82** (14), 144429 (2010).
7. M. Venkatesan, R. D. Gunning, P. Stamenov and J. M. D. Coey, *Journal of Applied Physics* **103** (7) (2008).
8. L.-M. Tang, L.-L. Wang, D. Wang, J.-Z. Liu and K.-Q. Chen, *Journal of Applied Physics* **107** (8), 083704-083705 (2010).
9. A. M. H. R. Hakimi, M. G. Blamire, S. M. Heald, M. S. Alshammari, M. S. Alqahtani, D. S. Score, H. J. Blythe, A. M. Fox and G. A. Gehring, *Physical Review B* **84** (8), 085201 (2011).

10. A. Urushibara, Y. Moritomo, T. Arima, A. Asamitsu, G. Kido and Y. Tokura, *Physical Review B* **51** (20), 14103-14109 (1995).
11. T. Koide, H. Miyauchi, J. Okamoto, T. Shidara, T. Sekine, T. Saitoh, A. Fujimori, H. Fukutani, M. Takano and Y. Takeda, *Physical Review Letters* **87** (24), 246404 (2001).
12. H. Boschker, M. Huijben, A. Vailionis, J. Verbeeck, S. v. Aert, M. Luysberg, S. Bals, G. v. Tendeloo, E. P. Houwman, G. Koster, D. H. A. Blank and G. Rijnders, *Journal of Physics D: Applied Physics* **44** (20), 205001 (2011).
13. J. Hofrichter, B. N. Szafrank, M. Otto, T. J. Echtermeyer, M. Baus, A. Majerus, V. Geringer, M. Ramsteiner and H. Kurz, *Nano Letters* **10** (1), 36-42 (2010).
14. Z. Sun, Z. Yan, J. Yao, E. Beitler, Y. Zhu and J. M. Tour, *Nature* **468** (7323), 549-552 (2010).

Appendix A

Chapter 6 – Appendix

The Sato method [1] was employed in order to discuss the magneto-optic spectrum of the medium that exhibits magnetic and birefringent behaviour. At optical frequencies, propagation of electromagnetic waves through a material can be described in terms of the electric permeability tensors, ε [2]. For a crystal with cubic symmetry magnetised perpendicularly to its surface, i.e., the z-direction, this dielectric tensor tensors can be written in the form:

$$\tilde{\varepsilon} = \begin{pmatrix} \tilde{\varepsilon}_{xx} & -i\tilde{\varepsilon}_{xy} & 0 \\ +i\tilde{\varepsilon}_{xy} & \tilde{\varepsilon}_{xx} & 0 \\ 0 & 0 & \tilde{\varepsilon}_{xx} \end{pmatrix} \quad \text{A. 6.1}$$

Where each element has real and imaginary part as:

$$\tilde{\varepsilon}_{ij} = \varepsilon_{ij}' + i\varepsilon_{ij}'' \quad \text{A. 6.2}$$

The diagonal elements ε_{xx} are related to normal refractive index and extinction coefficient. The off-diagonal element describes the magneto-optical effects such as the Kerr effects and the Faraday effect. The dielectric tensor, ε , for an isotropic magnetic medium with the magnetisation directed along the z axis, can be written as:

$$\varepsilon = \begin{pmatrix} \varepsilon_1 & -i\varepsilon_{xy} & 0 \\ i\varepsilon_{xy} & \varepsilon_1 & 0 \\ 0 & 0 & \varepsilon_3 \end{pmatrix} \quad \text{A. 6.3}$$

If the sample has a birefringence (Δ), the light transmitted through the sample can be calculated by writing the dielectric tensor as following:

$$\varepsilon = \begin{pmatrix} \varepsilon_1 - \Delta \sin^2 \psi & \Delta \sin \psi \cos \psi - i\varepsilon_{xy} & 0 \\ \Delta \sin \psi \cos \psi + i\varepsilon_{xy} & \varepsilon_1 - \Delta \cos^2 \psi & 0 \\ 0 & 0 & \varepsilon_3 \end{pmatrix} \quad \text{A. 6.4}$$

Here, Δ is the birefringence, $\Delta = \varepsilon_2 - \varepsilon_1$ and the magnetism is included via the off-diagonal term, ε_{xy} . The eigenstates of propagation are given in term of Γ and γ :

$$u_1 = \begin{pmatrix} \cos \Gamma \\ \sin \Gamma e^{i\gamma} \end{pmatrix} \quad \text{and} \quad u_2 = \begin{pmatrix} -\sin \Gamma e^{-i\gamma} \\ \cos \Gamma \end{pmatrix} \quad \text{A.6.5}$$

$$\sin \gamma = \frac{\varepsilon'_{xy}}{C_0} \quad \text{A.6.6}$$

$$\tan \Gamma = \frac{\sqrt{\Delta^2 + 4\varepsilon'^2_{xy} - \Delta \cos 2\psi}}{2C_0} \quad \text{A.6.7}$$

$$C_0 = \frac{1}{2} \sqrt{\Delta^2 \sin^2 \psi \cos^2 \psi + 4 \varepsilon'^2_{xy}} \quad \text{A.6.8}$$

$$\cos \gamma = \frac{\Delta \sin 2\psi}{\sqrt{\Delta^2 \sin^2 2\psi + 4 \varepsilon'^2_{xy}}} \sim 1 - \frac{2\varepsilon'^2_{xy}}{\Delta^2 \sin^2 2\psi} \quad \text{A.6.9}$$

The two values of the dielectric constant are given by:

$$\lambda_{\pm} = \frac{1}{2} (2\varepsilon_1 - \Delta \pm \sqrt{\Delta^2 + 4\varepsilon_{xy}^2}) \quad \text{A.6.10}$$

The refractive indices are given by:

$$n_{\pm} = \sqrt{\lambda_{\pm}} = \sqrt{\varepsilon} \left[1 - \frac{1}{4\varepsilon_1} (\Delta \pm \sqrt{\Delta^2 + 4\varepsilon_{xy}^2}) \right] \quad \text{A.6.11}$$

The rotation ($\theta_1 - \theta_2$) and ellipticity are evaluated respectively from:

$$\text{Re}(n_+ - n_-) = -\frac{\sqrt{\Delta^2 + 4 \text{Re}\varepsilon_{xy}^2}}{2\sqrt{\varepsilon_1}} \quad \text{A.6.12}$$

$$\text{Im}(n_+ - n_-) = \frac{-\text{Im}\sqrt{\Delta^2 + 4\varepsilon_{xy}^2}}{4\sqrt{\varepsilon_1}} = \frac{-4\varepsilon'_{xy}\varepsilon''_{xy}}{2\sqrt{\varepsilon_1}\sqrt{\Delta^2 + 4\varepsilon'_{xy}}} \quad \text{A. 6.13}$$

If the birefringence, Δ , is small. According to equation (6.11), we revert to the standard result; otherwise the ellipticity is a maximum for a minimum value of Δ . The aim, therefore, is to obtain the ellipticity from the birefringence (Δ) with as little contamination as possible.

From the Sato method, and after detailed mathematics, the final intensity, after passing through the Sato rig, is given by:

$$\frac{I_1(f)}{I_0} = C_1 J_1(\delta_0)(A \sin\gamma - B \cos\gamma) \quad \text{A. 6.14}$$

$$\frac{I_2(2f)}{I_0} = C_2 J_2(\delta_0)(A \cos\gamma + B \sin\gamma) \quad \text{A. 6.15}$$

Where $A = \frac{1}{2} \sin 4\Gamma (1 - \cos(\theta_1 - \theta_2)) + 2\eta \sin 2\Gamma$, $B = \sin 2\Gamma \sin(\theta_1 - \theta_2)$, $J_1(\delta_0)$ and $J_2(\delta_0)$ are Bessel functions. The coefficients C_1 and C_2 can be determined by the calibration procedure.

The terms involving $\sin\gamma$ are odd under magnetic field reversal; and terms in $\cos\gamma$ are even under magnetic field reversal and hence do not contribute in a magneto-optic measurement. The measurements can be made both in a magnetic field and in zero magnetic field. In the case of measurements made in a field (H), the difference between the measurements for $+H$ and $-H$ is taken and only terms in $\sin\gamma$ remain:

$$\frac{I_1(f)}{I_0} = C_1 J_1(\delta_0) \left[\sin\gamma \left(\frac{1}{4} \sin 4\Gamma (\theta_1 - \theta_2)^2 + 2\eta \sin 2\Gamma \right) \right] \quad \text{A. 6.16}$$

$$\frac{I_2(2f)}{I_0} = C_2 J_2(\delta_0) [\sin\gamma [\sin 2\Gamma \sin(\theta_1 - \theta_2)] \sim \sin\gamma [\sin 2\Gamma (\theta_1 - \theta_2)]] \quad \text{A. 6.17}$$

If the measurement was taken in zero field then ϵ_{xy} and γ should be zero.

Hence it is found that:

$$\sin \gamma = 0; \quad \cos \gamma = 1; \quad \tan \Gamma = \frac{\Delta(1 - \cos 2\psi)}{\Delta \sin 2\psi} = \tan \psi$$

$$\text{and } C_0 = \frac{1}{2} \Delta \sin 2\psi$$

In this case, the $\frac{I_1(f)}{I_0}$ and $\frac{I_2(2f)}{I_0}$ spectra are given by:

$$\frac{I_1(f)}{I_0} = \sin 2\Gamma \sin(\theta_1 - \theta_2) \sim \sin 2\Gamma (\theta_1 - \theta_2) \quad \text{A.6.18}$$

$$\frac{I_2(2f)}{I_0} = \frac{1}{4} \sin 4\Gamma (\theta_1 - \theta_2)^2 + 2\eta \sin 2\Gamma \quad \text{A.6.19}$$

References

1. K. Sato, Japanese Journal of Applied Physics **20** (12), 2403-2409 (1981).
2. S. Wittekoek, T. J. A. Popma, J. M. Robertson and P. F. Bongers, Physical Review B **12** (7), 2777-2788 (1975).